

Determination of Soil Moisture and Vegetation Parameters from Spaceborne C-Band SAR on Agricultural Areas

Inaugural-Dissertation

zur

Erlangung des Doktorgrades

der Mathematisch-Naturwissenschaftlichen Fakultät

der Universität zu Köln

vorgelegt von

Sabrina Esch

Köln, 2018

Gutachter: Prof. Dr. Karl Schneider

Prof. Dr. Georg Bareth

Tag der mündlichen Prüfung: 09.01.2018

Abstract

Soil moisture is an important factor influencing hydrological and meteorological exchange processes at the land surface. As ground measurements of soil moisture cannot provide spatially distributed information, remote sensing of soil moisture using Synthetic Aperture Radar (SAR) offers an alternative. To derive soil moisture from vegetated areas with SAR, the influence of vegetation parameters on SAR backscatter must be considered, though.

The first part of the study analyses the potential to use a qualitative soil moisture index from ERS-SAR with high spatial resolution that can be used without ground truth soil moisture and vegetation data. The index ranges from low to high soil moisture instead of giving absolute soil moisture values. The method is applied to agricultural areas in the catchment of the river Rur in Germany. The soil moisture index represents wetting and drying tendencies well when compared to precipitation records and behaves like in-situ soil moisture regarding its variability. The analysis of spatial patterns from the soil moisture index by using semivariograms reveals that differences in management that result for example in differences in evapotranspiration from one to the next agricultural field, are the only influence on spatial patterns of soil moisture in the Rur catchment. This study confirms the applicability of a high-resolution soil moisture index for monitoring soil moisture changes and to analyze spatial soil moisture patterns. The soil moisture index could be used as input to hydrological models and could substitute antecedent precipitation, which needs precipitation stations, as a proxy to soil moisture.

The second part of the study examines the capability of dual-polarimetric C-Band SAR data with high incidence angles from the Sentinel-1 satellites to derive soil moisture and vegetation parameters quantitatively. A processing scheme for Sentinel-1 Level-1 data is presented to produce images of different SAR observables that are compared to extensive ground measurements of soil moisture and vegetation parameters. It shows that soil moisture retrieval is feasible from bare soil and maize with an RMSE of 7 Vol%. From other land use types, different vegetation parameters could be retrieved with an error of around 25 % of their range, in median. Neither soil moisture nor vegetation parameters could be derived from grassland and triticale due to the influence of the thatch layer and the missing of a clear row structure. Both grassland and triticale are in contrast to the other crops not sown in rows on our research fields. The analysis has shown that the incidence angle is of main importance for the capability of C-band SAR to derive soil moisture and that the availability of at least one co- and cross-polarized channel is important for the quantitative retrieval of land surface parameters. The dual-pol H2 α parameters were not meaningful for soil moisture and vegetation parameter retrieval in this study.

Kurzzusammenfassung

Bodenfeuchte hat einen großen Einfluss auf hydrologische und meteorologische Austauschprozesse an der Landoberfläche. Die Fernerkundung von Bodenfeuchte mittels Radar mit synthetischer Apertur (SAR) bietet eine Alternative zu in-situ Messungen von Bodenfeuchte, da diese keine räumlich verteilten Informationen geben können. Um Bodenfeuchte unter Vegetation mit Hilfe von SAR ableiten zu können, müssen jedoch Vegetationsparameter berücksichtigt werden.

Der erste Teil dieser Arbeit analysiert das Potential eines qualitativen Bodenfeuchteindex, der aus ERS-SAR Daten abgeleitet wurde, mit hoher räumlicher Auflösung Bodenfeuchte abzuleiten, ohne dass in-situ Messungen von Bodenfeuchte und Vegetation nötig sind. Der Index produziert keine absoluten Werte sondern relative Werte zwischen hoher und niedriger Bodenfeuchte. Die Index Methode wird auf landwirtschaftliche Flächen im Einzugsgebiet des Flusses Rur in Deutschland angewandt. Der Bodenfeuchteindex zeigt, dass er Abtrocknungs- und Befeuchtungstendenzen im Vergleich mit Niederschlagsmessungen gut abbilden kann und sich bezüglich der Bodenfeuchtevariabilität wie in-situ gemessene Bodenfeuchte verhält. Die Analyse der räumlichen Bodenfeuchtemuster mittels Semivariogrammen offenbart, dass Unterschiede in Bewirtschaftung und hiermit in Evapotranspiration zwischen landwirtschaftlichen Feldern der einzige Einfluss auf die räumlichen Muster der Bodenfeuchte im Rur Einzugsgebiet sind. Der Bodenfeuchteindex kann als Eingangsgröße für hydrologische Modelle genutzt werden und somit den Vorniederschlag ersetzen, der häufig als Ersatz für Bodenfeuchte dient, jedoch ein Netz an Niederschlagsmessungen benötigt.

Der zweite Teil der Arbeit untersucht die Fähigkeit von dual-polarimetrischem Sentinel-1 C-Band SAR mit großem Einfallswinkel, Bodenfeuchte und Vegetationsparameter quantitativ abzuleiten. Eine Prozessierkette für Sentinel-1 SLC Daten wird präsentiert, die Bilder verschiedener SAR Parameter erzeugt, die wiederum mit umfangreichen Feldmessungen von Bodenfeuchte und Vegetationsparametern von landwirtschaftlichen Nutzflächen verglichen werden. Die Analyse zeigt, dass die Bodenfeuchteableitung auf Brache und Futtermaiskfeldern mit einem RMSE von 7 Vol. % möglich ist. Auf anderen Landnutzungen konnten verschiedene Vegetationsparameter mit einem Fehler von ca. 25 % des Wertebereichs im Median abgeleitet werden. Auf Grünland und Triticalefeldern können weder Bodenfeuchte noch Vegetationsparameter abgeleitet werden da die Streuschicht einen großen Einfluss auf die Rückstreuung hat und die Oberflächenstruktur von Grünland und Triticale auf Grund fehlender Reihenstruktur weniger

geordnet ist. Im Gegensatz zu den anderen untersuchten Vegetationsarten, sind beide auf unseren Untersuchungsfeldern nicht in Reihen gesät. Die Studie zeigt, dass der Einfallswinkel von besonderer Bedeutung ist für die Fähigkeit von C-Band SAR Bodenfeuchte abzuleiten. Außerdem ist das Vorhandensein von mindestens einem ko- und kreuzpolarisiertem Kanal wichtig für die Ableitung von Landoberflächenparametern. Die $H2\alpha$ Parameter waren in dieser Studie für die Ableitung von Bodenfeuchte und Vegetationsparameters nicht aussagekräftig.

Acknowledgments

This thesis was prepared during the second and third phase of the Transregional Collaborative Research Centre 32 (SFB/TR32) “Patterns in Soil-Vegetation-Atmosphere Systems: Monitoring, Modelling and Data Assimilation”, funded by the German Research Foundation (DFG). I gratefully acknowledge the financial support. I would also like to thank the European Space Agency (ESA) for the provision of the ERS-SAR data through their PI-program (AOALO.3570) and for providing the Sentinel-1A data through the Copernicus Program.

The thesis was supervised by Prof. Dr. Karl Schneider, who gave me the chance to participate in TR32 since I started working on my diploma thesis. I am grateful for that. My thanks go to Prof. Dr. Georg Bareth, who accepted to be the second reviewer of my thesis, Prof. Dr. Susanne Crewell for accepting to be head of the examination board and to Prof. Dr. Uwe Rascher and Dr. Wolfgang Korres for being advisors in my doctoral committee.

My thanks go also to Dr. Tim G. Reichenau for many discussions, good ideas and his help in mastering R problems.

I thank our student assistants, Tobias Bothe, Lars Knapik, Alicia Takbash, Michael Holthausen, Jan Peters, Stefan Linnarz, Claire Zimmermann and Stephanie Scheffler for helping to collect the in-situ data that were used this thesis. Thanks also to Julian Helge Braatz for preparing the land use maps that were used in the ERS study.

Thanks to Dr. Verena Dlugoß, Dr. Wolfgang Korres, Dr. Tim G. Reichenau and Nadine Bellinghausen for proof-reading parts of my thesis.

My special thanks go to my partner Emilio Martínez de Santiago for his overall support and understanding during stressful times and of course for proof-reading this thesis as well.

I am most grateful to my parents Kurt and Marita Esch who supported me always with everything and encourage me continuously.

Contents

| | |
|---|-------------|
| Abstract..... | I |
| Kurzzusammenfassung | II |
| Acknowledgments..... | IV |
| Contents | V |
| List of Figures..... | VIII |
| List of Tables | X |
| List of Abbreviations | XI |
| 1 Introduction..... | 1 |
| 2 Theoretical Basis for Soil Moisture Retrieval with Synthetic Aperture Radar | 6 |
| 2.1 Synthetic Aperture Radar Remote Sensing | 6 |
| 2.1.1 SAR Geometry | 7 |
| 2.1.2 SAR Image Formation | 11 |
| 2.1.3 Speckle Reduction | 13 |
| 2.2 SAR Polarimetry | 15 |
| 2.3 Soil Moisture and its Measurement..... | 20 |
| 2.3.1 Relevance of Soil Moisture | 21 |
| 2.3.2 Measurement of Soil Moisture | 22 |
| 2.3.3 Factors Influencing Soil Moisture Variability..... | 25 |
| 2.4 Surface Roughness and its Effect on SAR Backscatter..... | 26 |
| 2.4.1 Field Measurement of Surface Roughness..... | 28 |
| 2.5 Vegetation Influence on SAR Backscatter | 29 |
| 3 State of the Art of Soil Moisture Estimation with SAR | 32 |
| 4 Materials & Methods: Analysing two Methods to Derive Land Surface Parameters from C-Band SAR | 35 |
| 4.1 Study Area | 35 |
| 4.1.1 Geology and Soils..... | 37 |
| 4.1.2 Climate | 38 |
| 4.1.3 Test Sites | 38 |
| 4.2 SAR Data | 39 |

| | | |
|----------|---|-----------|
| 4.2.1 | ERS-SAR Data | 39 |
| 4.2.2 | Sentinel-1A Data | 41 |
| 4.3 | Land Use Information..... | 43 |
| 4.4 | Soil Moisture and Precipitation Data for the Soil Moisture Index Approach | 44 |
| 4.5 | Field Measurements of Soil Moisture, Vegetation, and Surface Roughness..... | 45 |
| 4.5.1 | Soil Moisture Measurements..... | 46 |
| 4.5.2 | Vegetation Measurements | 47 |
| 4.5.3 | Roughness Measurements | 48 |
| 4.6 | Soil Moisture Index Approach..... | 50 |
| 4.6.1 | Developing the Soil Moisture Index Scheme..... | 51 |
| 4.6.2 | Evaluating the Soil Moisture Index Maps..... | 51 |
| 4.7 | Geospatial Analysis of SMI Maps | 53 |
| 4.8 | Sentinel-1 Processing and Algorithm Development | 54 |
| 4.8.1 | S1A Radiometric Calibration Refinement | 56 |
| 4.8.1 | Algorithm Development for the Retrieval of Soil Moisture, Plant Parameters, and Surface Roughness | 58 |
| 5 | Results & Discussion: Soil Moisture and Vegetation Parameters from SAR | 61 |
| 5.1 | The Qualitative ERS Soil Moisture Index | 61 |
| 5.1.1 | ERS-1 & 2 Tandem Scenes for Drying and Wetting Processes | 63 |
| 5.1.2 | Comparing the Soil Moisture Index to Antecedent Precipitation..... | 65 |
| 5.1.3 | Summary Qualitative ERS Soil Moisture Index | 70 |
| 5.2 | Analysis of Spatial Patterns of Soil Moisture in the Rur Catchment | 71 |
| 5.2.1 | Summary Spatial Patterns of Soil Moisture in the Rur catchment | 77 |
| 5.3 | Sensitivity of Sentinel-1A to Soil Moisture and Vegetation Characteristics | 77 |
| 5.3.1 | Bare Soil Signal Analysis..... | 78 |
| 5.3.2 | Sugar Beet Signal Analysis | 81 |
| 5.3.3 | Cereal Signal Analysis | 83 |
| 5.3.4 | Maize Signal Analysis | 88 |
| 5.3.5 | Grassland and Triticale Signal Analysis | 90 |
| 5.3.6 | Signal Analysis Summary | 94 |
| 5.4 | Retrieval of Soil Moisture and Vegetation Parameters from S1A Data..... | 95 |
| 5.4.1 | The Bare Soil Model..... | 95 |
| 5.4.2 | The Sugar Beet Model | 100 |
| 5.4.3 | The Cereal Model | 104 |

5.4.4 The Maize Model..... 107

5.4.5 The Grassland and Triticale Model 112

5.4.6 Summary Models for Land Surface Parameter Retrieval 112

6 Conclusions and Perspective 114

7 References..... 119

Appendix..... 127

List of Figures

| | |
|--|----|
| Figure 2.1. Different types of radiation with corresponding wavelength..... | 6 |
| Figure 2.2. Scheme of a side looking spaceborne SAR..... | 7 |
| Figure 2.3. Radar Geometry..... | 8 |
| Figure 2.4. Ground-range vs. slant-range geometry..... | 9 |
| Figure 4.1. Catchment of the River Rur with main land use types | 36 |
| Figure 4.2. Map of the Digital Elevation Model of the Rur catchment..... | 36 |
| Figure 4.3. Schematic overview of measurement sites | 39 |
| Figure 4.4. Overview of the locations of the precipitation measurements | 44 |
| Figure 4.5. Custom laser scanner for roughness measurements | 49 |
| Figure 4.6. Processing chain for Sentinel-1 SLC data..... | 55 |
| Figure 4.7. Stable targets for radiometric accuracy study | 56 |
| Figure 4.8. Comparison of γ_{0VV} and γ_{0VH} for 2015 and 2016. | 58 |
| Figure 4.9. Excerpt from S1A γ_{0VV} image | 59 |
| Figure 5.1. Monthly boxplots of backscattering coefficient. | 62 |
| Figure 5.2. SMI maps based on single pixels | 63 |
| Figure 5.3. Maps of SMI differences from ERS tandem pairs | 64 |
| Figure 5.4. Theoretical relationship between soil moisture and antecedent precipitation..... | 66 |
| Figure 5.5. Comparison of antecedent precipitation with daily mean soil moisture..... | 67 |
| Figure 5.6. Comparison of antecedent precipitation with mean SMI..... | 67 |
| Figure 5.7. Comparison of antecedent precipitation averaged by SMI class..... | 68 |
| Figure 5.8. Comparison of Antecedent Precipitation Index with SMI values. | 69 |
| Figure 5.9. Comparison of Antecedent Precipitation Index with daily mean soil moisture... | 70 |
| Figure 5.10. Comparison of SMI Standard Deviation and SMI Mean..... | 72 |
| Figure 5.11. Exemplary empirical semivariogram..... | 73 |
| Figure 5.12. Relationship of short range to standard deviation f..... | 75 |
| Figure 5.13. Relationship of short range to mean SMI | 75 |
| Figure 5.14. Temporal Evolution of short ranges | 76 |
| Figure 5.15. Correlation heat map for bare soil | 79 |
| Figure 5.16. Histograms of backscatter per bare soil field | 80 |
| Figure 5.17. Correlation heat map for sugar beet..... | 82 |
| Figure 5.18. Histograms of backscatter per sugar beet field | 83 |
| Figure 5.19. Correlation heat map for winter barley. | 84 |
| Figure 5.20. Histograms of backscatter per winter barley field..... | 85 |

| | |
|---|-----|
| Figure 5.21. Correlation heat map for winter wheat. | 86 |
| Figure 5.22. Histograms of backscatter per winter wheat field | 87 |
| Figure 5.23. Correlation heat map for maize. | 88 |
| Figure 5.24. Histograms of backscatter per maize field | 89 |
| Figure 5.25. Correlation heat map for grassland. | 91 |
| Figure 5.26. Histograms of backscatter per grassland field | 92 |
| Figure 5.27. Correlation heat map for triticale. | 93 |
| Figure 5.28. Histograms of backscatter per triticale field | 94 |
| Figure 5.29. Relationship between surface soil moisture and γ_{0VV} for bare soil..... | 96 |
| Figure 5.30. Comparison of measured and estimated soil moisture for bare soil..... | 97 |
| Figure 5.31. Relationship between k_s and the Crosspol Ratio | 100 |
| Figure 5.32. Relationship between canopy height and γ_{0vv} for sugar beet | 101 |
| Figure 5.33. Comparison of measured and estimated canopy height for sugar beet..... | 102 |
| Figure 5.34. Comparison of estimated and measured VWC for sugar beet. | 103 |
| Figure 5.35. Comparison of estimated and measured biomass for sugar beet..... | 104 |
| Figure 5.36. Relationship of green LAI and γ_{0vv} for cereals..... | 105 |
| Figure 5.37. Relationship of green LAI and the Crosspol Ratio for cereals..... | 106 |
| Figure 5.38. Comparison of measured and estimated green LAI for cereals | 106 |
| Figure 5.39. Comparison of measured and estimated green LAI for cereals. | 107 |
| Figure 5.40. Relationship between soil moisture and γ_{0vv} under maize. | 108 |
| Figure 5.41. Comparison of measured and estimated soil moisture under maize..... | 109 |
| Figure 5.42. Relationship between green LAI and the Crosspol Ratio on maize. | 109 |
| Figure 5.43. Comparison of measured and estimated green LAI for maize. | 110 |
| Figure 5.44. Relationship between canopy height and γ_{0vh} for maize. | 111 |
| Figure 5.45. Comparison of estimated and measured canopy height for maize. | 111 |

List of Tables

| | |
|--|-----|
| Table 2.1. Overview of different radar bands | 6 |
| Table 4.1. Overview of the 84 ERS-acquisitions | 40 |
| Table 4.2. Overview of Sentinel-1A acquisitions. | 42 |
| Table 4.3. Overview of the field measurements | 45 |
| Table 4.4. Overview of field measurements of soil moisture | 47 |
| Table 4.5. Maximum of measured vegetation parameters..... | 48 |
| Table 4.6. Radiometric calibration refinement for Sentinel-1A | 56 |
| Table 4.7. Mean and Standard Deviation (SD) of γ_0 | 57 |
| Table 5.1. Mean precipitation measured at the ten different stations a | 65 |
| Table 5.2. Mean <i>RMSE</i> for soil moisture retrieval on bare soil..... | 97 |
| Table 5.3. Overview of different models to retrieve roughness..... | 99 |
| Table 5.4. Mean <i>RMSE</i> for the retrieval of canopy height for sugar beet. | 101 |
| Table 5.5. Mean <i>RMSE</i> for the retrieval of VWC from sugar beet..... | 102 |
| Table 5.6. Mean <i>RMSE</i> for the retrieval of sugar beet biomass..... | 103 |
| Table 5.7. Mean <i>RMSE</i> for the retrieval of green LAI using models 5.6 and 5.7..... | 107 |
| Table 5.8. Mean <i>RMSE</i> for soil moisture retrieval from maize. | 108 |
| Table 5.9. Mean <i>RMSE</i> for LAI retrieval from maize..... | 110 |
| Table 5.10. Mean <i>RMSE</i> for canopy height retrieval from maize..... | 111 |
| Table A.1. User's Accuracy of the yearly land use maps..... | 128 |
| Table A.2. Overall Accuracy of the yearly land use maps..... | 128 |
| Table A.3. Kappa-Values of the yearly land use maps..... | 129 |

List of Abbreviations

| | |
|-----------|--|
| ACF | Autocorrelation Function |
| ACL | Autocorrelation Length |
| ALOS | Advanced Land Observing Satellite |
| DEM | Digital Elevation Model |
| DLR | Deutsches Zentrum für Luft- und Raumfahrt |
| EC | European Commission |
| ENVISAT | Environmental Satellite |
| ERS | European Remote Sensing Satellite |
| ESA | European Space Agency |
| FDR | Frequency Domain Reflectometry |
| GMES | Global Monitoring for Environment and Security |
| GPS | Global Positioning System |
| HH | Horizontally Transmitting Horizontally Receiving |
| HV | Horizontally Transmitting Vertically Receiving |
| IQR | Inter Quartile Range |
| IW | Interferometric Wide Swath |
| LAI | Leaf Area Index |
| LIA | Local Incidence Angle |
| LMMSE | Linear Minimum Mean Square Error |
| LOOCV | Leave-One-Out Cross-Validation |
| LUT | Look Up Table |
| MAP | Maximum A Posteriori |
| MMSE | Minimum Mean Square Error |
| NASA | National Aeronautics and Space Administration |
| NDVI | Normalized Difference Vegetation Index |
| PDF | Probability Density Function |
| Radar | Radio Detecting and Ranging |
| RCS | Radar Cross Section |
| RFI | Radio Frequency Interference |
| RMS | Root Mean Square (Height) |
| RMSE | Root Mean Square Error |
| S1A | Sentinel 1A |
| SAOCOM-CS | SAOCOM Companion Satellite |

| | |
|--------|--|
| SAR | Synthetic Aperture Radar |
| SLC | Single Look Complex |
| SMI | Soil Moisture Index |
| SNAP | Sentinels Application Platform |
| SNR | Signal-to-Noise Ratio |
| TDR | Time Domain Reflectometry |
| TOPSAR | Terrain Observation with Progressive ScanSAR |
| TSX | TerraSAR-X |
| VH | Vertical Transmit Horizontal Receive |
| VV | Vertical Transmit Vertical Receive |
| VWC | Vegetation Water Content |

1 Introduction

Soil moisture is one of the main drivers of the complex soil-vegetation-atmosphere exchange processes. It determines the partitioning of incoming solar radiation into sensible and latent heat flux as well as the partitioning of precipitation into surface runoff and infiltration. Hereby, it influences the energy and water budget at the land surface. Moreover, plant growth and thus food production strongly depends upon the availability of soil moisture. Understanding soil moisture dynamics is important to understand carbon and nitrogen fluxes at the earth surface. Thus, soil moisture and its spatial and temporal patterns is of key importance for basic science as well as for application, as various studies show (Bell et al., 1980, Blume et al., 2009b, Famiglietti et al., 1999, Mohanty et al., 2000, Schmugge and Jackson, 1996). However, due to the spatial variability of properties at the earth surface in terms of soil (e.g. soil texture) and terrain (e.g. slope) and due to the many processes affecting the water fluxes of the soil-vegetation-atmosphere continuum (e.g. precipitation, water uptake, and evapotranspiration), soil moisture is variable both in terms of space and time.

There are different ways to determine soil moisture, which can be summarized as in-situ measurements, models, or remote sensing. While in-situ measurements give the most accurate results, they are time- and cost-intensive and only provide point information. They are typically used to calibrate and validate spatially distributed techniques such as models and remote sensing. Likewise, spatially distributed soil-vegetation-atmosphere models require in-situ measurements for model parametrization and validation. Those models provide spatially distributed, continuous data, with high temporal resolution. Alternatively, airborne, or satellite-based remote sensing can provide spatially-distributed soil moisture information, ideally without the need of in-situ data. Both active and passive, air- and spaceborne microwave remote sensing systems can be used to estimate near surface soil moisture. Compared to modelled soil moisture that can be provided continuously, the temporal resolution of remote sensing soil moisture products is currently low. While passive microwave remote sensing is limited to a coarse spatial resolution (Lakshmi, 2013, Fang et al., 2013, Mohanty et al., 2017), active microwave remote sensing such as Synthetic Aperture Radar (SAR) can provide high-resolution near-surface soil moisture information.

Near-surface soil moisture cannot be measured directly with SAR remote sensing. The principle of soil moisture estimation from radar remote sensing is well described (Engman, 1991, Jackson et al., 1996, Roth et al., 1992, Schmugge and Jackson, 1996, Schmugge et al., 1980, Topp et al., 1980) and is based on the dependence of the backscatter intensity upon the dielectric constant of the observed medium. The relative dielectric constant ϵ_r varies largely between air (~ 1),

soil particles (~5) and water (~80) (Jackson et al., 1996, Engman, 1991). Therefore, in mixtures of dry soil, air and water, variations in the relative dielectric constant, that imply variations in the backscatter intensity, mainly depend on changes in volumetric soil water content. The penetration depth of the SAR signal, which is the depth at which the power of the incident wave is attenuated by $1/e$, increases with increasing wavelength and decreases with increasing moisture content (Campbell, 2002, Ulaby et al., 1982, Bruckler et al., 1988). It is in an order of magnitude comparable to the wavelength (Boisvert et al., 1995). Thus, remotely sensed soil moisture relates to the uppermost few centimetres of the soil. In addition to soil moisture, the surface roughness and vegetation cover affects the backscatter intensity to a high degree. Therefore, to assess the soil moisture state on vegetated areas by remote sensing, the influence of surface roughness and vegetation on the backscatter must be estimated as well. Consequently, developing methods to retrieve vegetation and roughness parameters by remote sensing, are indispensable for soil moisture retrieval on vegetated areas.

Researchers have developed theoretical, semi-empirical and empirical models to retrieve soil moisture values from radar remote sensing (Thoma et al., 2006b, Verhoest et al., 2008). Theoretical approaches (Fung et al., 1992) model the backscattering behaviour of incoming microwaves, based on incidence angle, frequency, surface roughness and relative dielectric constant. These approaches require many input parameters, which are not available under practical conditions. They are usually restricted to bare soil conditions. Approaches exploiting the polarimetric information to decompose the backscattered signal and hereby correcting for vegetation and roughness effects (Hajnsek et al., 2009, Jagdhuber et al., 2014b) need full polarimetric SAR data that is supplied only by few sensors (e.g. Radarsat-2, ALOS-2). Thus, semi-empirical approaches are widely used instead, especially for vegetated areas. They require only few input parameters, mainly vegetation (e.g. type, growth stadium, and biomass), surface roughness and soil texture (Baghdadi et al., 2004, Oh, 2004, Rombach and Mauser, 1997). Correlating soil moisture and backscatter requires a large range of field measurements. Moreover, these approaches are often restricted to areas with characteristics comparable to the calibration region. Applying an existing semi-empirical retrieval scheme (Rombach and Mauser, 1997) that was developed for southern Germany, to our research catchment in western Germany in previous work, revealed a systematic overestimation when compared to measured near-surface soil moisture. In many regions of the earth and for most historic datasets (such as the vast ERS archives) suitable ground truth data to calibrate semi-empirical retrieval schemes is unavailable. Furthermore, (semi)-empirical retrieval schemes are sensor-specific. Thus, the application of existing

empirical approaches either to a different SAR-system or to a different research area may result in large errors.

To learn more about underlying structures that influence soil moisture patterns, it is important to analyse the spatial soil moisture distribution. The spatial variability of soil moisture for example, changes with mean soil moisture state (Vereecken et al., 2007) and also its spatial structure exhibits a temporal course and a dependency on the soil moisture state (Korres et al., 2015, Western et al., 1998). To understand the development and fade of soil moisture patterns, repetitive observations with suitable temporal resolution are needed. Current data of this format are not available at this time. However, the extensive set of historic ERS data provides a valuable data base to analyse spatial patterns and to investigate whether recurrent structures can be found.

ERS SAR data, are now available since 1991 and provide a long historic time series of backscatter observations worldwide. The lack of ground truth measurements usually limits their use for soil moisture studies. So far, there is no retrieval approach that provides multi-temporal soil moisture information on a spatial scale that would enable the monitoring of soil moisture patterns within agricultural fields when no ground truth measurements are available. Therefore, the **first scope** of this thesis is to present a qualitative approach to determine surface soil moisture and its patterns that does not require in situ measurements of soil moisture and vegetation parameters and which is based only on remote sensing. Instead of giving absolute soil moisture values, the approach produces an index ranging from low to high soil moisture. For many applications, such as the analysis of soil moisture patterns or drought monitoring, it should be sufficient to know the moisture state in qualitative terms rather than in absolute values. The approach in this study is based on a time series of SAR-data from the European Remote Sensing Satellites (ERS-1 & -2). While most semi-empirical approaches to determine soil moisture exploit the information contained in each image separately, multi-temporal approaches have already been applied successfully e.g. on Radarsat-2 data (Tomer et al., 2015) and on low resolution ERS scatterometer data (Wagner et al., 1999b). The approach presented here utilizes the vast ERS data archives to answer the following questions:

- i) Can the qualitative near-surface soil moisture status in the Rur catchment be assessed without in-situ measurements?
- ii) How can a soil moisture retrieval scheme be validated in the absence of corresponding in-situ measurements of soil moisture?

- iii) Can near-surface soil moisture patterns in the Rur catchment be found from qualitative data and can their occurrence be explained?

A different way to develop a soil moisture retrieval scheme that can be applied without the need of additional empirical calibration is to use the information supplied by the different channels of multi-polarimetric SAR. Quad-Pol data offer the greatest potential to fully decompose the backscattering fractions from vegetation and soil (Jagdhuber et al., 2014b), but are unfortunately not widely available due to limited spatial coverage. Dual-Pol data, as provided by the Sentinel-1A/B satellites, poses a compromise between polarimetric information and spatiotemporal resolution. Despite not allowing for full decomposition of the backscatter signal, by using dual-polarimetric observables, the observation space can be increased drastically compared to single channel SAR (Jagdhuber et al., 2014a). A former study in the Rur catchment has shown that dual-pol data from the L-Band satellite ALOS-1 is suitable for soil moisture retrieval under vegetation (Koyama and Schneider, 2010). As C-Band has a lower penetration depth compared to L-Band data, its usefulness to provide accurate quantitative soil moisture information under vegetation has been questioned (Wiseman et al., 2014).

Up to now, there is no scheme to describe quantitatively the influence of soil moisture and vegetation parameters on SAR backscatter and enable their retrieval with high spatial resolution from dual-polarimetric C-Band SAR like provided by the Sentinel-1 satellites.

Therefore, a huge dataset of ground-truth measurements during simultaneous Sentinel-1A (S1A) acquisitions gives the opportunity to assess the potential of C-Band SAR from S1A for soil moisture studies and its potential to derive vegetation parameters, which are not only important for the backscatter correction but also as input for Soil-Vegetation-Atmosphere models.

Consequently, the **second scope** of this thesis is to develop a quantitative semi-empirical retrieval scheme for soil moisture and vegetation parameters based on dual-polarimetric Sentinel-1A data and ground truth data from intensive field studies. Hereby the following questions shall be answered:

- iv) Is C-Band SAR data from S1A with high incidence angles suitable for the quantitative estimation of near surface soil moisture under vegetation?
- v) Can semi-empirical algorithms be developed that make the huge open source data archive of Sentinel-1A/B usable for soil moisture and vegetation studies?

Overall, this thesis aims to improve the extraction of soil moisture and vegetation information from C-band SAR on agricultural fields

- a) to monitor spatial and temporal patterns of soil moisture
- b) to enable qualitative soil moisture retrieval without ground measurements and
- c) to enable the retrieval of high resolution quantitative soil moisture and vegetation parameters from the newly launched dual-polarimetric Sentinel-1 satellites.

The research area of this thesis is the Rur catchment in western Germany. It is characterized by a fertile loess plain in the northern part and a low mountain range in the southern part. It is the research area of the Collaborative Research Center TR 32 “Patterns in soil, vegetation, atmosphere systems”, which is a collaborative project of the University of Bonn, University of Cologne, RWTH Aachen and Research Centre Jülich (Simmer et al., 2015). The project runs in three phases from 2007-2018. The goal of TR32 is to find patterns in land and atmosphere parameters, to describe the processes of their development and how they are influenced and finally to enable their prediction. The subproject C3, in whose framework this thesis was prepared, focuses in this context on surface soil moisture pattern analysis, using radar remote sensing and modelling. By analysing cause and effect relationships leading to surface soil moisture patterns, the understanding of relevant processes and the scaling properties of soil moisture and water fluxes shall be improved and the parameterization of the Community Land Model (CLM) shall be enhanced. In the third phase, the subproject was organized in the three work packages: satellite remote sensing, model analysis and field measurements. This thesis summarizes results of the work packages satellite remote sensing and field measurements mainly of the third phase of TR32.

The thesis is structured as follows:

Chapter 2 provides an overview about the theoretical principles of SAR remote sensing and its application for soil moisture retrieval and defines soil moisture and describes its relevance. **Chapters 3** introduces the state of the art of SAR remote sensing with respect to soil moisture retrieval. **Chapter 4** describes the study area and the datasets that have been used and discusses two different methods for soil moisture retrieval that are used in this thesis. **Chapter 5** presents the results of the retrieval of soil moisture and vegetation parameters. It is subdivided into the chapters 5.1-5.2 that describe the qualitative soil moisture retrieval from ERS-SAR and its application to analyse spatial soil moisture patterns. Chapter 5.3 presents an analysis of the sensitivity of SAR backscatter to different land surface parameters and chapter 5.4 presents semi-empirical models for the retrieval of vegetation parameters and soil moisture from different land use types. The thesis is concluded with **chapter 6** that draws and discusses the conclusions and presents possibilities for future work.

2 Theoretical Basis for Soil Moisture Retrieval with Synthetic Aperture Radar

To understand soil moisture retrieval with Synthetic Aperture Radar (SAR) in detail, first an adequate theoretical background has to be established. Therefore, the theoretical basis in this chapter encompasses an introduction to SAR remote sensing, SAR Polarimetry and to soil moisture and its measurement. Furthermore it illustrates the effects of surface roughness and vegetation parameters on SAR backscatter.

2.1 Synthetic Aperture Radar Remote Sensing

Remote Sensing is defined as the analysis of the physical properties of a target from a remote location (Campbell, 2002). For that, radiation in different spectra can be used, depending on the target of interest and its relationship to the given radiation properties.

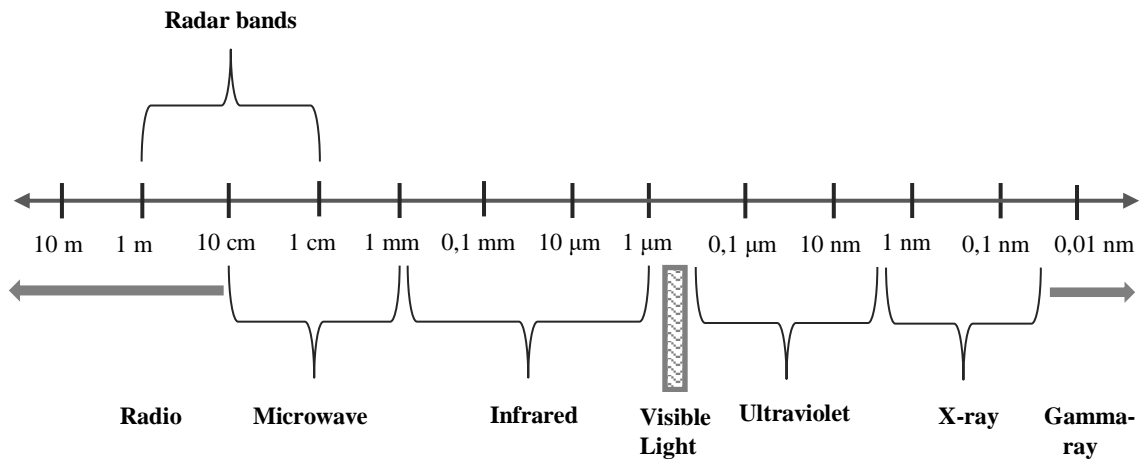


Figure 2.1. Different types of radiation with corresponding wavelength.

In contrast to optical remote sensing, which uses light in the visible spectrum, microwave remote sensing employs radiation in the spectrum of the radar bands at about 1 m to 1 cm wavelength (Figure 2.1 & Table 2.1). As longer wavelengths allow for a deeper penetration into the target material, microwave remote sensing can be utilized to examine subsurface or volume structures. Bands with wavelengths longer than X-band, are also not sensitive to cloud cover, thus enabling weather-independent observation.

Table 2.1. Overview of different radar bands and their corresponding frequency ranges and wavelength.

| Band | Ka | Ku | X | C | S | L | P |
|-----------------|----------|---------|--------|----------|--------|-------|----------|
| Frequency [GHz] | 40-25 | 17.6-12 | 12-7.5 | 7.5-3.75 | 3.75-2 | 2-1 | 0.5-0.25 |
| Wavelength [cm] | 0.75-1.2 | 1.7-2.5 | 2.5-4 | 4-8 | 8-15 | 15-30 | 60-120 |

Generally, two types of sensors for remote sensing applications can be distinguished: active sensors, transmitting pulses actively and receiving their backscatter from the earth surface and passive sensors, measuring the radiation from their target. Most optical sensors are passive and therefore depend on the sunlight as radiation transmitter. As active microwave remote sensing systems come with their own radiation source, they can operate day and night.

Active microwave remote sensing is also called radar (**R**adio **D**etecting **A**nd **R**anging) remote sensing and dates back to the 1920s when mainly long radio waves were used (Jensen, 2007).

2.1.1 SAR Geometry

Radar remote sensing systems can have a bistatic or monostatic constellation. A bistatic constellation has a transmitting and a receiving antenna (e.g. upcoming SAOCOM-CS mission). Most current spaceborne radar remote sensing missions employ a monostatic design, where a single antenna switches between transmitting and receiving the backscattered echoes. In this thesis, only monostatic constellations are considered.

A Synthetic Aperture radar (SAR) is a side-looking coherent imaging radar (a radar that creates a 2D image) mounted on a moving platform. To describe the SAR geometry, we need to differentiate azimuth (or along track) direction, that is the direction of platform movement, and range (or across track) direction, that is perpendicular to the direction of movement (Figure 2.2).

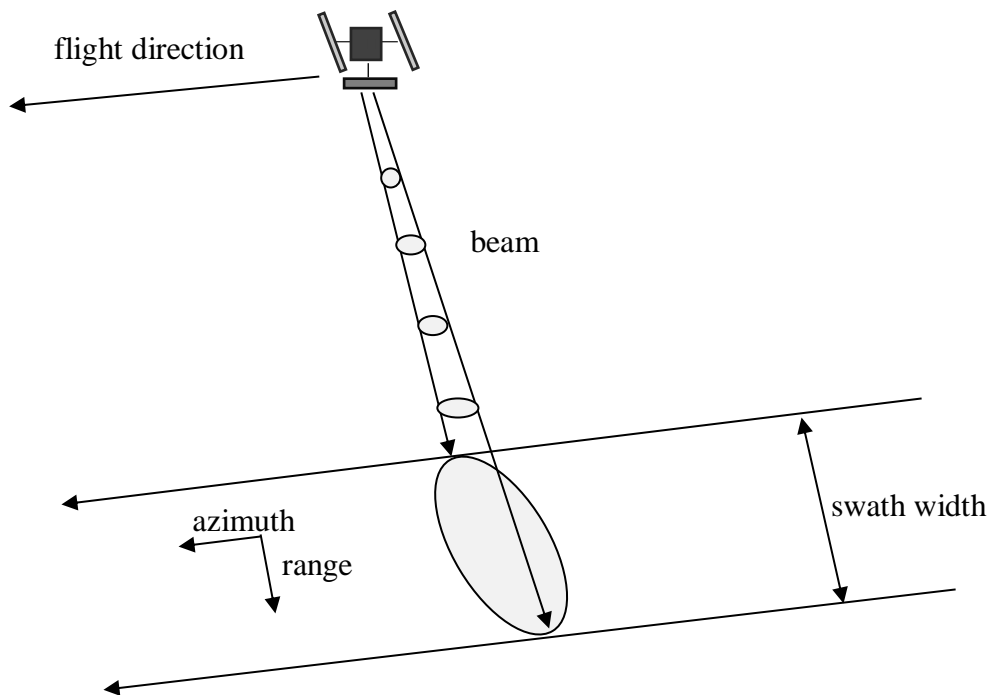


Figure 2.2. Scheme of a side looking spaceborne SAR. The beam covers a swath of a given width in ground resolution. The duration of the data take determines the length of the swath.

Basically, SAR uses the time that a sent-out pulse takes to return to the antenna, to locate an object spatially. SAR sensors are side-looking, so that two targets in range direction with the same elevation can be discriminated. Short distances to nadir are referred to as near-range, long distances as far range (Figure 2.3). The native SAR geometry is in slant range, a plane perpendicular to flight direction. The incidence angle is later used to project the image to ground range and determines the ground range resolution.

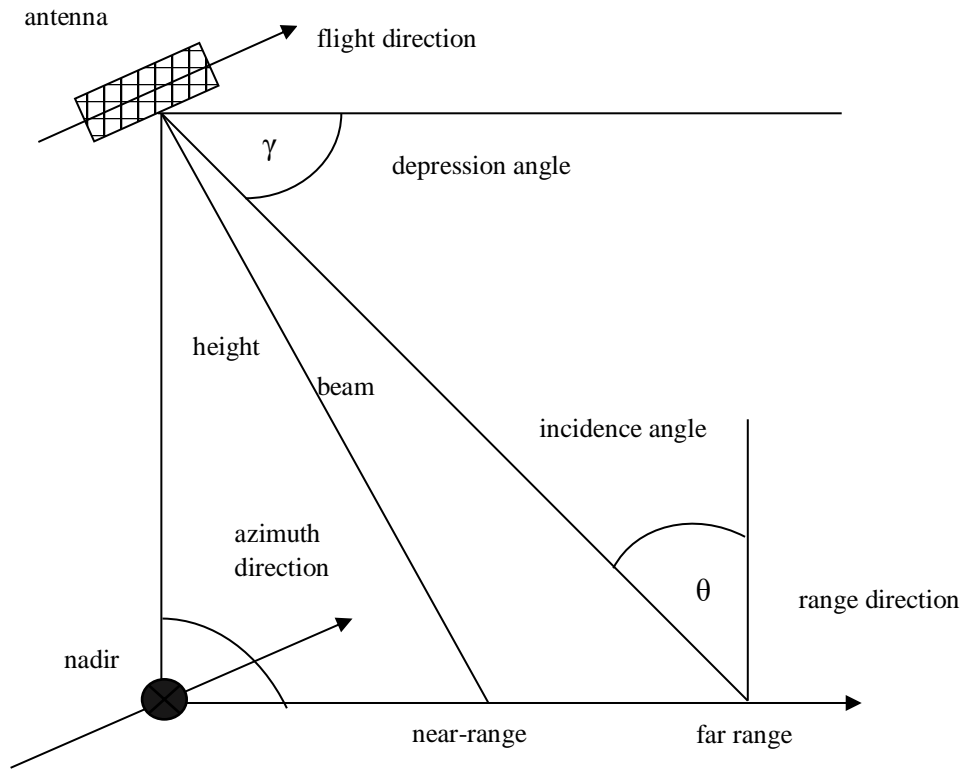


Figure 2.3. Radar Geometry.

The spatial resolution in slant range can be defined as the minimal distance that two objects can have to each other to be recognized as two objects rather than one (Mott, 2007). For SAR, we must differentiate range and azimuth resolution.

In slant range, for two targets to be resolved, the echo of the first target must be differentiable from the echo of the second target (Figure 2.4), thus the spatial resolution in range direction is defined as:

$$\delta_{RS} = \frac{c\tau_p}{2} = \frac{c}{2B} \quad (2.1)$$

With $c = 3,8 \times 10^8$ [m/s], τ_p = pulse duration [μ s] and B = bandwidth [rad] (Maitre, 2008, Sabins, 2007, Mott, 2007).

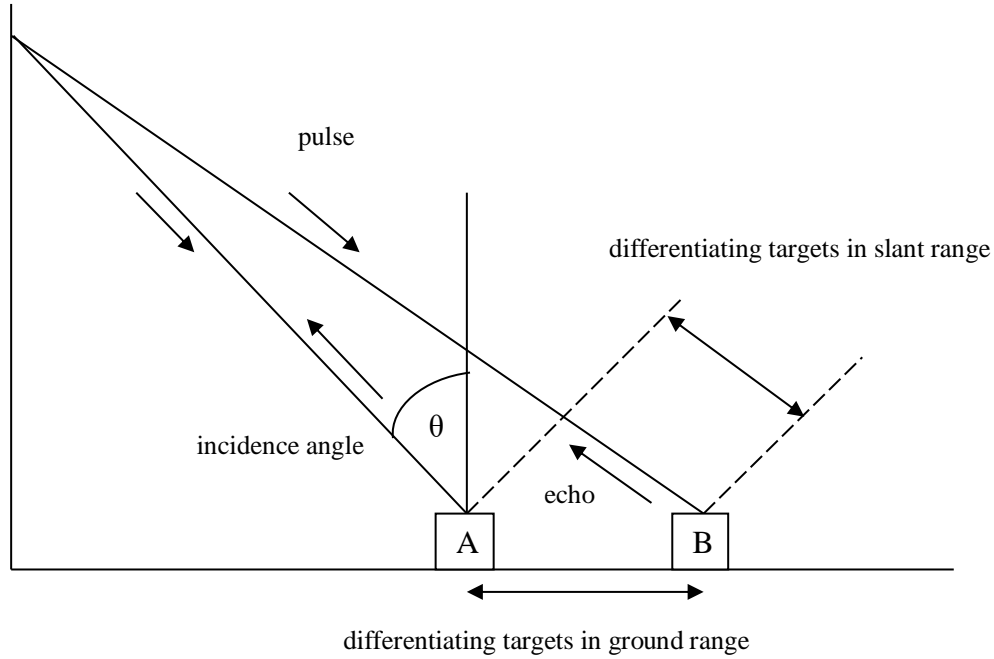


Figure 2.4. Ground-range vs. slant-range geometry. Modified according to (Richards, 2009).

Therefrom we can derive that range resolution can be increased using a short pulse. However, if this is done, the average power may drop low (Mott, 2007) and the Signal-to-Noise Ratio (SNR) would decrease (Sabins, 2007). The second part of (2.1) on the other hand shows the possibility to increase spatial resolution by increasing the bandwidth. This can be done by pulse-compression radars that usually use a frequency-modulated pulse, or chirp (Mott, 2007). The amplitude of the transmitted waveform is constant during the pulse duration, while the instantaneous frequency is varied according to (Moreira et al., 2013):

$$f_i = k_r \cdot t \quad (2.2)$$

, where k_r is the chirp rate, yielding the bandwidth

$$B = k_r \cdot \tau_p. \quad (2.3)$$

The pulse is followed by the echo window time during which the radar listens to the scattered echoes and stores the received signal. The transmission and listen procedure is repeated every PRI seconds, where the pulse repetition interval (PRI) is reciprocal of the pulse repetition frequency (Moreira et al., 2013):

$$PRI = \frac{1}{PRF}. \quad (2.4)$$

An acquisition in slant range shows the distance, or the time delay from the sensor to the target. To project the acquisition to ground range (Figure 2.4) we can use for the range resolution (Sabins, 2007):

$$\delta_{Rg} = \frac{c\tau_p}{2\sin\theta} \quad (2.5)$$

with θ = incidence angle, $c = 3,8 \times 10^8$ [m/s] and τ_p = pulse duration [μ s].

The spatial resolution improves with increasing incidence angle, thus from near-range to far-range (Richards, 2009). Due to the range geometry, different image distortions may occur in areas with topography:

- **Foreshortening:** When looking at a slope, the backscattered pulse of an elevated area in a distinct range position reaches the sensor earlier than if the same area was not elevated, as it is closer to the sensor in slant range. This may lead to a decreased slope length on the image.
- **Layover:** This is an extreme case of foreshortening, when the pulse on top of the slope reaches the sensor earlier than the pulse from the bottom of the slope. The image appears inverted.
- **Shadowing:** There is a radar shadow at the back-slope of a mountain, as the area is obscured from the radar beam.

These topography effects are corrected or reduced during geometrical image processing, utilizing a high resolution digital elevation model (DEM).

For a conventional radar, the azimuth resolution depends on the antenna size and the range distance from the antenna to the target. As for spaceborne radars, the range distance is high, a huge antenna would be needed to provide an acceptable resolution. To overcome this limitation, the synthetic aperture radar principle is used, that employs a coherent radar (preserving proper phase relationships) and the principle of Doppler beam sharpening. This principle relies on the relative movement between antenna and target that changes the frequency of the echoes based on the Doppler frequency. The azimuth resolution is then provided by the construction of the synthetic aperture which is the path length during which the radar receives echo signals from a point target. The azimuth resolution δ_{AS} is then defined as:

$$\delta_{AS} = \frac{l_a}{2} \quad (2.6)$$

with l_a = antenna size. This means a shorter antenna yields a finer azimuth resolution (Moreira et al., 2013). Nevertheless, a SAR antenna may not be infinitely small, as with a smaller antenna the beam width in azimuth direction decreases. In turn, the Doppler bandwidth of the received signal decreases and thus the PRF must increase to allow for accurate Doppler frequency estimation. But if the PRF increases, the swath width decreases, because the backscattered signal from far range must reach the sensor before the next pulse is transmitted (Mott, 2007). Thus,

antenna design is always a trade-off between spatial resolution and spatial coverage.

The echo signal data that are received, form a two-dimensional data matrix of complex samples, where each complex sample is given by its real and imaginary part, thus representing an amplitude and phase value. The first dimension corresponds to the range direction; a range line consists of the complex echo signal sampled. The radar acquires a range line whenever it travels a distance $v \cdot PRI$, thus forming the second dimension of the data matrix, known as azimuth (Moreira et al., 2013).

2.1.2 SAR Image Formation

Unlike optical sensors, visualizing raw SAR data does not give any useful information on the scene. It is only after signal processing that an image is obtained (Moreira et al., 2013). From these complex images, other products can be formed, for example images of the real part $A \cos\theta$ (the in-phase component i), the imaginary part $A \sin\theta$ (the quadrature component q), the amplitude A , the phase θ , the intensity $I = A^2$ or the dB-image, calculated as:

$$I[dB] = \log_{10}(I) \cdot 10 \quad (2.7)$$

for each pixel in the calibrated intensity image (Oliver and Quegan, 2004). Normally, a SAR image is displayed in terms of intensity values such that each image pixel gives an indication of the reflectivity of a corresponding location on the ground. Therefore, calibration and geocoding must be performed. The calibration ensures that the intensity value represents the sigma nought value of the reflectivity. Sigma nought is defined as the radar cross section (RCS) normalized to the ground area (Moreira et al., 2013). Typically radar cross-sections are specified as HH (horizontally transmitting, horizontally receiving), HV (horizontally transmitting, vertically receiving) etc. The RCS traces back to the radar equation (Lee and Pottier, 2009):

$$P_R = \frac{P_T G_T(\theta, \phi)}{4\pi r_T^2} \sigma \frac{A_{ER}(\theta, \phi)}{4\pi r_R^2} \quad (2.8)$$

, with P_R = power detected at receiving system, P_T = transmitted power, G_T = transmitting antenna gain, A_{ER} = effective aperture of the receiving antenna, r_T = distance between transmitting system and the target, r_R = distance between the target and the receiving system and the azimuth and elevation angles θ, ϕ .

That radar equation establishes the relation between the power which the target intercepts from the incident electromagnetic wave and the power reradiated by the same target in the form of the scattered wave. The RCS of an object is then defined as the cross section of an equivalent idealized isotropic scatterer that generates the same scattered power density as the object in the observed direction. The RCS is given by:

$$\sigma = 4\pi r^2 \frac{|\vec{E}_s|^2}{|\vec{E}_I|^2} \quad (2.9)$$

and sigma nought is then defined as:

$$\sigma_0 = \frac{\sigma}{A_0}, \quad (2.10)$$

with A_0 = illuminated ground area. Beta nought is defined as:

$$\beta_0 = \frac{\sigma}{A_s}, \quad (2.11)$$

with A_s = area sample interval in slant range, where the area in slant range depends on the local incidence angle. It provides the natural radar observable (Raney et al., 1994). Gamma nought is defined as:

$$\gamma_0 = \frac{\sigma}{A_\gamma}, \quad (2.12)$$

Where A_γ is the projection in the plane perpendicular to the slant range direction (Small et al., 2009) and describes the unit area of the incident wave front (Cosgriff et al., 1960). Therefore it describes best how a radar “sees” a target. For a correct σ_0 and γ_0 representation, the local incidence angle must be known, e.g. by utilizing a high-resolution DEM.

Because of the coherent nature of SAR, elemental scatterers with a random distribution within a resolution cell cause speckle. It is produced by the coherent sum of the amplitudes and phases of the backscatter by the elemental scatterers that cause a strong fluctuation of the backscattering, resulting in brighter and darker pixels (Moreira et al., 2013, Massonnet and Souyris, 2008). The individual scattering amplitudes and phases are unobservable, because the individual scatterers are on much smaller scales than the resolution of the SAR. This causes a salt-and-pepper like appearance. While speckle is noise like, it is not noise but a real electromagnetic measurement (Oliver and Quegan, 2004). The mechanism is not random but cannot be predicted (Oliver and Quegan, 2004) as it would need exactly the same radar geometry and distribution of elemental scatterers to be reproduced. This problem is even inherent in very high resolution SAR, when the spatial resolution is close to the wavelength, depending on the size of the targets (Lee et al., 2015). Considering a point target, each pixel supplies a real measurement of backscattered power or amplitude. When the pixel is made up of many elementary scatterers, as is the case for distributed targets, the observed power is an estimate of an underlying RCS whose true value is being masked by interference effects (Oliver and Quegan, 2004). Brighter pixels will be affected by stronger disturbances than darker ones (Argenti et al., 2013).

2.1.3 Speckle Reduction

Despite not being exactly reproducible, the speckle effect can be reduced. Speckle reduction or despeckling methods should be carefully designed to avoid spoiling useful information, such as local mean of backscatter, point targets, linear features, and textures (Argenti et al., 2013). A way to improve the estimation of the RCS is to average L independent intensity values related to the same position. This processing, called “Multilooking” maintains the mean intensity of the RCS but reduces its variance (Argenti et al., 2013). The resulting image is known as L -look (Oliver and Quegan, 2004). In general, radiometric accuracy is improved at the cost of spatial resolution. There are two different approaches to obtain the independent intensity values: 1.) Averaging in the frequency domain by splitting the synthetic aperture Doppler bandwidth into independent sub-bands or 2.) By averaging in the spatial domain over a neighbourhood surrounding the pixel of interest. Both cases are statistically identical but suppress different types of information to improve radiometric accuracy: 1.) Neglects angular variation in the RCS while 2.) Loses spatial variation (Oliver and Quegan, 2004). While SARscape performs multilooking in the frequency domain (used on the ERS-data), SNAP performs spatial multilooking (used on the Sentinel-1 data).

An important positive side-effect of multilooking is that by choosing an appropriate L in range and azimuth direction, quadratic pixels with constant pixel spacing are generated. This prevents over- or undersampling during the geocoding process. If the averaging is performed on the complex images rather than on amplitudes or intensities, no speckle reduction is archived, because the process is identical to the vector sum of the total number of elementary scatterers from the L images. The statistics remain identical to that of single look SAR data (Lee and Pottier, 2009, Oliver and Quegan, 2004). Consequently, the only advantage of multilooking complex data, is the generation of quadratic pixels.

To smooth speckle further without blurring out spatial heterogeneities, dedicated speckle filters can be applied after the image has been formed. In the last decades, a multitude of such filters has been developed by combining different domains of estimation (spatial, homomorphic, wavelet, and homomorphic-wavelet), the estimation criteria (e.g., MMSE, LMMSE, MAP or non-Bayesian) and the PDF models (Argenti et al., 2013). In principle, speckle reduction of distributed targets requires averaging pixels within a homogeneous area (Lee et al., 2009) but preserving edges. The Lee Filter is the first model-based despeckling filter and is based on local statistics. A LMMSE solution was derived by linearizing the multiplicative noise model around the mean of the noisy signal (Argenti et al., 2013). Each pixel can be processed separately and

it is assumed that the a priori mean and variance can be derived from the local mean and variance of a window (Lee, 1981). Other common filters for example are the Frost filter (Frost et al., 1982), the Kuan filter (Kuan et al., 1985) or the Lee sigma filter (Lee, 1983).

The Lee sigma filter is based on the two-sigma probability of a Gaussian distribution. It reduces speckle noise by replacing the centre pixel of a scanning window with the average of those pixels within the two-sigma range of the centre pixel. Pixels outside the two-sigma range are regarded as outliers and are not used to calculate the sample mean (Lee et al., 2009).

The improved Lee Sigma Filter overcomes several deficiencies of the original Lee sigma filter: bias is removed by redefining the sigma range, a MMSE estimator is included and strong targets are preserved (Lee et al., 2009). For polarimetric SAR, the speckle effect appears not only in the intensities but also in the complex correlation terms. Thus, polarimetric variables must be smoothed by averaging the coherency or covariance matrices of neighbouring pixels (Lee et al., 2015). The basic procedure in PolSAR speckle filtering is to locate pixels of similar scattering property to filter effectively (Lee et al., 2015).

The extended Lee Sigma Filter is an extension to the improved Lee Sigma Filter for the polarimetric case. General steps for the improved Lee Sigma and the extended Lee Sigma Filter are: 1. Detection of strong point targets (in the polarimetric case for double bounce and specular returns) in a 3x3 window, 2. From the rest of the pixels the a priori mean is estimated and pixels in the sigma range are selected (for the polarimetric case only pixels selected by all polarizations are filtered). 3. MMSE filter is applied (for polarimetric case to coherency or covariance matrix, with a weighting factor determined by the selected pixels).

Multitemporal speckle filters apply a weighted average based on a stack of images, thus exploiting the speckle statistics of several input images to enhance filtering. In general, the selection of a speckle-filtering algorithm is determined by application requirements and personal preference (Lee et al., 2015). This means, there is no such thing as a perfect speckle filter. For example, as we are interested in data that changes significantly with time, we do not consider multitemporal filtering as a good option as it would smooth temporal effects.

2.2 SAR Polarimetry

In contrast to conventional single-channel SAR like e.g. ERS, that provides only information about backscattering intensity and phase, polarimetric SAR like e.g. ALOS-2 or Radarsat-2, exploits the polarization state of a backscattered wave. The polarization state depends on the geometrical structure and orientation of a target and can describe, in combination with intensity information, the physical properties of a medium.

The behaviour of electromagnetic waves in time and space is described by the Maxwell equations. The simplest solution to the wave propagation equations is given by considering a monochromatic plane wave. A monochromatic wave is a wave with a single frequency and can be described at a given point in time on a plane perpendicular to the direction of travel by its two orthogonal components (Hecht, 2014, Lee and Pottier, 2009):

$$E_x = E_{0x} e^{i(kz - \omega t + \varphi_x)} \quad (2.13.1)$$

$$E_y = E_{0y} e^{i(kz - \omega t + \varphi_y)} \quad (2.13.2)$$

With E_0 = amplitude, k = wavenumber = $\frac{2\pi}{\lambda}$, z = direction of propagation, ω = angular frequency, t = time, φ = absolute phase.

These two components are oscillating in time with the same frequency. For convenience, they can also be fully described by the amplitude and phase information in the form of a phasor or complex amplitude, in this case called Jones Vector:

$$\underline{E} = \begin{bmatrix} E_x = E_{0x} e^{i\varphi_x} \\ E_y = E_{0y} e^{i\varphi_y} \end{bmatrix} \quad (2.14)$$

With the real part $\vec{E}(z, t) = \text{Re}(\underline{E} e^{i(kz - \omega t)})$.

The Jones vector describes the polarization state of the wave. The amplitude A of the electromagnetic wave can now be calculated as:

$$A = \sqrt{E_{0x}^2 + E_{0y}^2} \quad (2.15)$$

And the intensity I as:

$$I = E_{0x}^2 + E_{0y}^2 \quad (2.16)$$

The Jones Vector for a horizontally polarized wave has the form $H = \begin{bmatrix} 1 \\ 0 \end{bmatrix}$ and for the vertically polarized wave $V = \begin{bmatrix} 0 \\ 1 \end{bmatrix}$.

When an incident wave reaches the ground, and interacts with a scatterer, the scatterer transforms the incident wave into a (back-) scattered wave. It changes the polarization state of the

incident wave and the degree of polarization. This interaction can be described by the Sinclair matrix for the bistatic case with:

$$[S] = \begin{bmatrix} S_{hh} & S_{hv} \\ S_{vh} & S_{vv} \end{bmatrix}. \quad (2.17)$$

The elements of $[S]$ are the four complex scattering amplitudes $S_{ij} = |S_{ij}|e^{i\varphi_{ij}}$, with ij = transmitted and received polarization (Moreira et al., 2013). In the monostatic case the reciprocity theorem is applied so that $S_{hv} = S_{vh} = S_{xx}$.

The transformation from the transmitted to the received wave, is then given as:

$$\underline{E}^r = \frac{e^{ikr}}{r} [S]\underline{E}^t \quad (2.18)$$

where the factor $\frac{e^{ikr}}{r}$, the absolute phase, expresses the phase shift and attenuation for a spherical wave of a radius that equals the distance between the scatterer and the radar (Moreira et al., 2013). The absolute phase term is important in SAR interferometry to estimate the location of the scatterer but is neglected in SAR polarimetry, where only the relative phases between the matrix elements are considered (Moreira et al., 2013). Altogether, in a monostatic constellation we have five independent parameters that fully describe our scattering process: three amplitudes and two relative phases.

The Sinclair matrix can characterize pure or point-like targets but fails to describe distributed scatterers that are composed of many randomly distributed targets and are typical for natural targets. For distributed scatterers, the measured scattering matrix consists of the coherent superposition of the scattering matrices from all the individual targets (Moreira et al., 2013, Lee and Pottier, 2009). To extract physical information, we must decompose our resulting scattering matrix into simpler processes, which means to break down the scatter of a resolution cell into a sum of elementary scattering contributions. Therefore, a second-order statistical formulation is necessary to describe space and time varying stochastic processes that can be extracted from the polarimetric coherency or covariance matrices. The first step is to represent the Sinclair matrix through the construction of system vectors:

$$[S] = V([S]) = \frac{1}{2} \cdot \text{Trace}([S] \cdot [\psi]), \quad (2.19)$$

with $V()$ as a vectorization operator and ψ a 2x2 basis matrix set. For the monostatic backscattering case the complex Pauli spin matrix basis set is defined as

$$\{\psi_p\} = \left\{ \sqrt{2} \begin{bmatrix} 1 & 0 \\ 0 & 1 \end{bmatrix}, \sqrt{2} \begin{bmatrix} 1 & 0 \\ 0 & -1 \end{bmatrix}, \sqrt{2} \begin{bmatrix} 0 & 1 \\ 1 & 0 \end{bmatrix} \right\}, \quad (2.20)$$

which results in the Pauli-vector:

$$\mathbf{k} = \frac{1}{\sqrt{2}} \begin{bmatrix} S_{hh} + S_{vv} \\ S_{hh} - S_{vv} \\ 2S_{xx} \end{bmatrix} \quad (2.21)$$

that is closely related to the physical properties of the scatterer. The Pauli decomposition expresses the Sinclair matrix as the complex sum of the Pauli matrices and decomposes the scatter into three elementary scattering mechanisms: $S_{hh} + S_{vv}$ for example, is sensitive to single bounce scattering or surface scattering, where no change in polarization occurs (e.g. flat area, corner reflector), $S_{hh} - S_{vv}$ is sensitive to double bounce scattering, or dihedral scattering, when a phase change in S_{vv} occurs (e.g. vertical structures, urban areas, tree trunks) whereas S_{xx} is sensitive to random polarization as in volume scattering (e.g. forests, full grown vegetation). In general, coherent decompositions as the Pauli decomposition or the Krogager decomposition (Krogager, 1990), express the Sinclair matrix as a combination of basis matrices corresponding to canonical scattering mechanisms (Lee and Pottier, 2009).

The lexicographic basis matrix set is defined as:

$$\{\psi_L\} = \left\{ 2 \begin{bmatrix} 1 & 0 \\ 0 & 0 \end{bmatrix}, 2\sqrt{2} \begin{bmatrix} 0 & 1 \\ 0 & 0 \end{bmatrix}, 2 \begin{bmatrix} 0 & 0 \\ 0 & 1 \end{bmatrix} \right\}, \quad (2.22)$$

and results in the Lexicographic-vector:

$$\Omega = \begin{bmatrix} S_{hh} \\ \sqrt{2}S_{xx} \\ S_{vv} \end{bmatrix}, \quad (2.23)$$

which relates directly to the system measure (Lee and Pottier, 2009, Moreira et al., 2013). By unitary transformation, we can calculate the Lexicographic-vector from the Pauli-vector and vice versa. In a second step, the 3x3 coherency $[T]$ or covariance $[C]$ matrix can be calculated by the outer product of the Pauli- or Lexicographic-vector:

$$T_3 = \langle \mathbf{k} \cdot \mathbf{k}^{*T} \rangle$$

$$= \frac{1}{2} \begin{bmatrix} \langle |S_{hh} + S_{vv}|^2 \rangle & \langle (S_{hh} + S_{vv})(S_{hh} - S_{vv})^* \rangle & 2\langle (S_{hh} + S_{vv})S_{xx} \rangle \\ \langle (S_{hh} - S_{vv})(S_{hh} + S_{vv})^* \rangle & \langle |S_{hh} - S_{vv}|^2 \rangle & 2\langle (S_{hh} - S_{vv})S_{xx} \rangle \\ 2\langle S_{xx}(S_{hh} + S_{vv})^* \rangle & 2\langle S_{xx}(S_{hh} - S_{vv})^* \rangle & 4\langle |S_{xx}|^2 \rangle \end{bmatrix} \quad (2.24)$$

$$C_3 = \langle \Omega \cdot \Omega^{*T} \rangle = \begin{bmatrix} \langle |S_{hh}|^2 \rangle & \sqrt{2}\langle S_{hh}S_{xx}^* \rangle & \langle S_{hh}S_{vv}^* \rangle \\ \sqrt{2}\langle S_{xx}S_{hh}^* \rangle & 2\langle |S_{hh}|^2 \rangle & \sqrt{2}\langle S_{xx}S_{vv}^* \rangle \\ \langle S_{vv}S_{hh}^* \rangle & \sqrt{2}\langle S_{vv}S_{xx}^* \rangle & \langle |S_{vv}|^2 \rangle \end{bmatrix} \quad (2.25)$$

The coherency matrix is the basis for Eigenvector-based decompositions like the Cloude (Cloude, 1985), Holm (Holm, 1988) or the Entropy/Alpha (H/α) decomposition by Cloude and Pottier (Lee and Pottier, 2009). Model based decompositions like the Freeman-Durden (Freeman and Durden, 1998) and the four-component Yamaguchi decomposition (Yamaguchi et al., 2005) generally use the covariance matrix.

As of these decompositions only the Entropy/Alpha decomposition has been extended to the dual polarimetric case so far, we concentrate on this decomposition in the following.

As the coherency matrix is Hermitian positive semi-definite, it can always be diagonalized by a unitary similarity transformation as (Moreira et al., 2013, Lee and Pottier, 2009):

$$[T] = [U][\Lambda][U]^{-1} \quad (2.26)$$

$$\text{With } [\Lambda] = \begin{bmatrix} \lambda_1 & 0 & 0 \\ 0 & \lambda_2 & 0 \\ 0 & 0 & \lambda_3 \end{bmatrix}, \text{ the eigenvalues and } [U] = \begin{bmatrix} e_{11} & e_{12} & e_{13} \\ e_{21} & e_{22} & e_{23} \\ e_{31} & e_{32} & e_{33} \end{bmatrix} = [\vec{e}_1, \vec{e}_2, \vec{e}_3],$$

the eigenvectors. Hereby, it can be decomposed into the non-coherent sum of three independent coherency matrices representing the scattering matrix of three independent targets like:

$$\begin{aligned} [T] &= [U][\Lambda][U]^{-1} = [T_1] + [T_2] + [T_3] \\ &= \lambda_1(\vec{e}_1 \vec{e}_1^+) \\ &+ \lambda_2(\vec{e}_2 \vec{e}_2^+) \\ &+ \lambda_3(\vec{e}_3 \vec{e}_3^+) \end{aligned} \quad (2.27)$$

The eigenvectors can now be parameterized in terms of five angles (Cloude, 1997, Cloude, 1996):

$$\vec{e}_i = \begin{bmatrix} \cos \alpha_i e^{i\psi} \\ \sin \alpha \cos \beta_i e^{i(\delta+\psi)} \\ \sin \alpha \sin \beta_i e^{i(\gamma+\psi)} \end{bmatrix}, \quad (2.28)$$

with, β_i the orientation angles and δ, ψ and γ the phases (Ji and Wu, 2015). α_i is the only roll invariant parameter. This means it remains invariant for rotation around the radar line of sight and thus is independent of the basis used for measuring the scattering matrix. It can therefore be used to identify the dominant scattering mechanism (Lee and Pottier, 2009). The mean scattering angle α is then defined as (Ji and Wu, 2015):

$$\alpha = \sum_{i=1}^N P_i \alpha_i \quad (2.29)$$

α_i ranges continuously from surface scattering ($\alpha_i = 0$) to dipole or single scattering from a cloud of anisotropic particles ($\alpha_i = 45$) to double bounce and dihedral scattering from metallic surfaces ($\alpha_i = 90$) (Lee and Pottier, 2009).

Two statistical parameters can be derived from the eigenvalues of the coherency matrix. The entropy H is given, according to Von Neumann as the logarithmic sum of the eigenvalues (Lee and Pottier, 2009, Moreira et al., 2013):

$$H = - \sum_{i=1}^N P_i \log_N(P_i), P_i = \frac{\lambda_i}{\sum_{j=1}^N \lambda_j} \quad (2.30)$$

Since the eigenvalues are roll-invariant, H is roll invariant, too. For low entropy ($H < 0.3$), the target is weakly depolarizing, so the process can be described by a single scattering matrix, corresponding to the largest eigenvalue. If entropy is high, the target is depolarizing and there is no longer a single dominant scattering mechanism. When $H = 1$, the polarization information becomes zero and the scattering is a random noise process. Therefore, H describes the randomness of the scattering process.

The polarimetric anisotropy A is complementary to the entropy H . It measures the relative importance of the second and the third eigenvalues. If the eigenvalues have been ordered as $\lambda_1 > \lambda_2 > \lambda_3 > 0$, anisotropy A is given as:

$$A = \frac{\lambda_2 - \lambda_3}{\lambda_2 + \lambda_3} \quad (2.31)$$

It is most informative for $H > 0.7$, because the second and third eigenvalues are highly affected by noise for lower entropies. It is roll invariant as well (Moreira et al., 2013, Lee and Pottier, 2009).

Sentinel-1 measures not the full polarization state but the dual polarimetric S_{vv} and S_{vh} components. The Sinclair matrix is in that case reduced to (Ji and Wu, 2015):

$$[S] = \begin{bmatrix} 0 & S_{vh} \\ S_{vh} & S_{vv} \end{bmatrix} \quad (2.32)$$

and the scattering vector k becomes:

$$k = \begin{bmatrix} S_{vv} \\ 2S_{vh} \end{bmatrix}. \quad (2.33)$$

The coherency matrix T is then defined as (Cloude, 2007):

$$T_v = \begin{bmatrix} \langle |S_{vv}|^2 \rangle & \langle S_{vv} S_{xx}^* \rangle \\ \langle S_{xx} S_{vv}^* \rangle & \langle |S_{xx}|^2 \rangle \end{bmatrix} \quad (2.34)$$

The off-diagonal elements of T_v can only be measured by coherent radar systems, like for example Sentinel-1. For radars that drop the coherent receive mode like Envisat ASAR, the Entropy/Alpha decomposition may not be applied (Cloude, 2007).

The Entropy/Alpha decomposition for the dual-pol case of coherent SAR systems is called H2 α decomposition to be distinguishable from the H/ α decomposition. Entropy and mean alpha angle can be calculated also for the dual-polarimetric case with (2.29-2.30). Anisotropy can be calculated according to (2.31) as:

$$A = \frac{\lambda_1 - \lambda_2}{\lambda_1 + \lambda_2} \quad (2.35)$$

As for the dual polarimetric case not three but only two different scattering mechanisms can be distinguished, A it is no longer clearly distinguishable from H . It is therefore no measure of secondary scattering mechanisms. The interpretation of dual-polarimetric H - A combinations has not yet been researched in detail (Heine et al., 2016).

2.3 Soil Moisture and its Measurement

Soil moisture only sums up to about 0.05% of the worldwide freshwater resources (Shiklomanov, 1993). Still, it plays an important role in the water and energy cycles on the soil surface.

Soil water that is contained in every soil under natural conditions is the part of the water in the soil that can be removed at a temperature of 105 °C. The soil is then defined as oven-dry. Water that vanishes only at higher temperatures is no soil water but crystal water that is bound to the solid soil particles (Chen and Hu, 2004, Blume et al., 2009a).

Assuming vertical fluxes only, precipitation and ground water charge the soil water that can be differentiated into two types. The first one is the water that percolates into deeper layers and feeds the ground water. The second type is the soil moisture that stays in the soil. The soil moisture is retained in the pores against gravity. In contrast to that, ground water is not retained in the soil matrix and is therefore also called free water (Blume et al., 2009a).

Engman (1991) defines soil moisture as a temporal reservoir of precipitation water within a thin layer of the earth that is generally limited to the vadose zone. According to Robock (2003), this layer is the active soil layer, which typically encompasses the uppermost 1-2 m of the soil. This vadose or unsaturated zone is characterized by pores that are partly filled with water and partly filled with air. In contrast to that stands the phreatic zone, or ground water zone where all pores are filled with water (Todd and Mays, 2004, Viessman and Lewis, 2003).

Soil moisture can be expressed gravimetrically as well as volumetrically (Kutflek and Nielsen, 1994, Warrick, 2003):

$$\theta_g = \frac{m_w}{m_s}, \quad (2.36)$$

with θ_g = gravimetric soil moisture, m_w = weight of water in the soil, m_s = total weight of soil and:

$$\theta_v = \frac{v_w}{v_s}, \quad (2.37)$$

with θ_v = volumetric soil moisture, v_w = volume of water in the soil and v_s = total volume of the soil. Soil moisture is dimensionless but is often expressed in percentage or in the units [g/g] or [m³/m³] respectively, to differentiate volumetric and gravimetric measurements.

2.3.1 Relevance of Soil Moisture

Near surface soil moisture influences two important exchange processes at the land atmosphere interface: both the water and the energy balance are affected by the moisture and temperature state of the soil.

Regarding water transport, soil moisture affects the partitioning of precipitation into infiltration and runoff. If the uppermost soil layers are saturated, precipitation will run off. If the soil is unsaturated, precipitation water will infiltrate. Therefore, spatial and temporal patterns of soil moisture have a high influence on the formation of surface runoff as well as on interflow and ground water (Blume et al., 2009b).

Soil moisture supplies water for plant growth and the availability of soil moisture has therefore a direct impact on agriculture. Via evapotranspiration, near-surface soil moisture regulates the partitioning of incoming energy at the land surface into sensible and latent heat. This becomes evident from the energy budget after (Marshall and Holmes, 1979) :

$$R_n = S + LE_t - G \quad (2.38)$$

with R_n = net radiation at the soil surface (incoming – outgoing short and long wave radiation), S = sensible heat, LE_t = latent heat consumed by evapotranspiration (= evaporation + transpiration) and G = soil heat flux.

If soil moisture is available, the incoming radiation is mainly converted to latent heat by the process of evapotranspiration. If the soil is dry, the energy budget must be balanced by thermal radiation and the sensible heat flux, resulting in the heating of the soil or the air. Soil moisture has also a huge influence on the heat capacity of the soil and influences hereby sensible heat and the soil heat flux.

Water and energy fluxes at the land surface influence the profile of water vapour and temperature of the atmosphere. This has in turn an effect on cloud development and the net radiation.

Therefore, soil moisture plays a major role in the complex interaction of land surface and atmosphere and is an important input parameter for climate models and weather predictions (Wei, 1995, Entekhabi et al., 1996).

2.3.2 Measurement of Soil Moisture

There are different methods to measure soil moisture that can be differentiated as direct and indirect methods as well as destructive and non-destructive methods.

Whereas direct methods measure the amount of soil moisture directly, indirect methods measure a physical characteristic of the soil, which is related to soil moisture.

For destructive methods soil samples are taken and analysed in the laboratory. This hinders the repetition of the measurement on the exactly same location. Additionally, those methods are labour-intensive. Therefore, destructive methods are not suitable for measurements with high temporal repetition.

For non-destructive methods, a sensor is usually permanently installed or repeatedly inserted into the soil. The indirectly measured soil moisture can directly be readout (e.g. TDR- / FDR-probes). This enables regular measurements without destroying the soil profile (Kutilek and Nielsen, 1994).

The classical gravimetric method is a direct and destructive method. Usually a soil sample is taken, weighed, oven-dried at 105°C and then weighed again. The difference between wet- and dry-weight of the soil sample is the soil moisture. If the density of the soil matrix is known, the gravimetric soil moisture can be converted to volumetric soil moisture. Despite being labour- and time-intensive, the gravimetric method is a wide spread standard method, as it is easy to perform and does not need expensive equipment (Hanks, 1992). Therefore, it is often used as a standard to calibrate indirect measurement methods (Kutilek and Nielsen, 1994). Nevertheless, the quality of the measurement depends on the quality of the sample-taking. One must avoid for example that water drips out of the sample or that water evaporates between sample-taking and weighing.

To estimate the soil moisture content on a frequent basis, usually indirect, non-destructive measurement methods are preferred. They can be based on electrical resistance like with the gypsum block method (Häckel, 2016) or on the transmission of different types of pulses, since the soil moisture content greatly influences this transmission. Therefore, the transmission or absorption of the signal can be scaled against gravimetric soil moisture content. Electrical conductance, thermal conductivity, gamma rays or cosmic rays can be used as a signal to estimate the soil moisture content (Scheffer & Schachtschabel, 2002).

Methods that use the electrical conductance as signal are based on the dielectric constant of water that is high in comparison to the surrounding soil matrix. Therefore, changes in the dielectric constant can be attributed mainly to changes in the volumetric soil moisture content. The principle of time-domain-reflectometry (TDR) is that the reflection of an electric pulse is delayed stronger, the higher the dielectric constant of the surrounding medium is (Scheffer & Schachtschabel, 2002). In a TDR probe, a pulse is generated that is transmitted by metallic conductors, which are inserted into the upper soil layer. When the pulse reaches the end of the conductor, it is reflected. As the transmission velocity of the wave is inversely proportional to the square root of the dielectric constant, the dielectric constant can be estimated easily. To calculate the volumetric soil moisture from the dielectric constant, usually an algorithm by (Topp et al., 1980) is used (WMO, 2014). Frequency-Domain-Reflectometry (FDR), which is the method used in our ground truth campaigns, functions likewise but uses changes in the frequency rather than changes in transmission velocity (Robock et al., 2000). The FDR as well as the TDR method can be applied either manually by using handheld probes or by installing a soil moisture sensor permanently within a measurement station.

All methods mentioned here, are well established but only provide point wise soil moisture information. Measurements on a large scale with sufficient measurement density are not feasible with the before mentioned methods due to the costs and the high amount of labour that is involved. As patterns of soil moisture are highly heterogeneous it is also not trivial to interpolate soil moisture for a region from few local measurements.

Therefore, it is obvious to consider remote sensing for the estimation of soil moisture, as this is the only method that allows regular monitoring on large scales. Despite that, the before mentioned methods do not lose their relevance as they are important means to calibrate and validate remote sensing observations.

With active or passive microwave remote sensing, near-surface soil moisture can be estimated, because microwaves have the capacity to penetrate the uppermost soil layers. Passive sensors measure the natural thermal emission of the soil surface in the microwave region (the so-called brightness temperature). It describes the temperature that a hypothetical black body would need to have to emit a comparable microwave intensity. This intensity can be connected to soil moisture. A downside of passive microwave remote sensing of soil moisture is the low spatial resolution (Jackson et al., 1996, Moran et al., 2004). The SMOS (Soil Moisture and Ocean Salinity) mission of ESA and the NASA SMAP (Soil Moisture Active Passive) mission are examples of passive satellite-based remote sensing of soil moisture. Here, global maps of soil moisture are produced with a spatial resolution of 50 km and 36 km, respectively.

As mentioned earlier, the principle of soil moisture estimation from radar remote sensing is the influence of the relative dielectric constant on the backscatter and the attenuation of the incoming microwave pulse, because the relative dielectric constant of a medium determines the transmission of waves in the medium (Schmugge et al., 1980).

The relative dielectric constant ϵ_r , also called relative permittivity, is given by the ratio of absolute permittivity to the permittivity of a vacuum ϵ_0 , also called electric constant ($\epsilon_0 = 8,85 \cdot 10^{-12}$ [C²/Nm²]). The relative dielectric constant is a measure for the effect of a dielectric, an electrically isolating material. Through a dielectric, the electric field for a given charge distribution is weakened (Halliday et al., 2008). Therefore, the relative dielectric constant ϵ_r describes the effect of a specific medium on the force of an electric field, as e.g. that of an electromagnetic wave, compared to the effect of a vacuum on the same electric field. The relative dielectric constant of a vacuum is defined as 1, the relative dielectric constant of air is approximately 1 that of soil particles is 5 and that of water 80, when referring to a wavelength of more than 5 cm (Jackson et al., 1996, Engman, 1991). The relative dielectric constant is a complex number and therefore consists of a real part ϵ_r' and an imaginary part ϵ_r'' . Because the imaginary part of the relative dielectric constant is small compared to the real part, the imaginary part can be neglected (Topp et al., 1980).

The relative dielectric constant of water is up to 20 times higher than that of dry soil, because water molecules are permanent dipoles that align with the impacting electric field. This large difference in dielectric constant of water and the surrounding soil enables the estimation of soil moisture using passive or active microwave sensors (WMO, 2014, Engman, 1991).

When looking at the interaction of an incoming microwave with a vegetated surface in a simplified model, one can set up an equation like this (Ulaby, 1981):

$$\sigma_0 = A \sigma_0^{veg} + B \sigma_0^{soil} + C \sigma_0^{sv} \quad (2.39)$$

With A describing the attenuating effect of vegetation on the direct backscatter from vegetation σ_0^{veg} , B describing the effect of soil moisture and surface roughness on direct soil surface backscatter σ_0^{soil} and C describing the effect of soil and vegetation interactions on indirect backscatter from vegetation and soil surface σ_0^{sv} . Therefore, to estimate soil moisture from SAR remote sensing the influence of vegetation and surface roughness on the backscatter must be known. Usually models to estimate soil moisture from SAR consist of two steps: At first, the influence of vegetation and surface roughness is corrected so that the backscatter can be correlated to the relative dielectric constant. Then, an empirical relationship between the relative dielectric constant and soil moisture is used to calculate volumetric soil moisture e.g. (Topp et al., 1980, Roth et al., 1992). Ulaby et al. (1986) however, proposed a direct linear relationship

between surface soil moisture and SAR intensity in dB, without the conversion to the relative dielectric constant. This relationship has been used in various studies (Cognard et al., 1995, Le Hegarat-Masclé et al., 2002, Quesney et al., 2000, Zribi et al., 2005).

2.3.3 Factors Influencing Soil Moisture Variability

The spatio-temporal distribution of near-surface soil moisture is very heterogeneous and is influenced by different static or dynamic factors. This becomes already evident when we consider that soils themselves are highly variable. Differences in the bedrock and the vegetation (e.g. by its root system) influence the variability of the soil matrix even on short distances. Therefore, soil characteristics vary from one location to the other (Kutílek and Nielsen, 1994). Those characteristics encompass the soil type, the amount of organic matter and the channel system created by roots or soil organisms. They are defined as static influences on the soil moisture distribution (Reynolds, 1970) and act mainly by their influence on infiltration rate, percolation, and storage capacity. Furthermore, effects of topography, hillslope and aspect are static influences.

Dynamic factors encompass the amount and the variability of precipitation (in the form of antecedent precipitation), the insolation (hereby the evaporation) the vegetation cover (hereby the transpiration and root water uptake) as well as the thatch layer, that can store large amounts of water (Reynolds, 1970). Also anthropogenic influences like fertilization or ploughing activities belong to the dynamic factors (Reynolds, 1970).

Static and dynamic factors can have different influences on soil moisture patterns (Famiglietti et al., 1998). Hillslope for example influences infiltration, percolation, and runoff. Therefore, steeper areas tend to be drier than flat terrains. The aspect of a slope influences insolation, hereby the evapotranspiration and eventually the soil moisture. Vegetation mainly influences soil moisture patterns by interception, canopy drip and the steering of evapotranspiration. The importance of the vegetation influence depends on the type and density of the vegetation and the season.

A variety of studies (Famiglietti et al., 1998, Reynolds, 1970, Bell et al., 1980, Vereecken et al., 2007, Pan et al., 2003) has found that spatial soil moisture variability depends also on the mean soil moisture state such that soil moisture variability is high for medium mean soil moisture states and low for high or low soil moisture states. Different influencing factors for wet and dry conditions can explain this unimodal shape: under wet conditions, spatial variability of soil moisture is controlled by spatial variability of soil properties like porosity and field capacity. When the soil dries, and reaches medium moisture conditions, spatial variability of soil moisture is regulated by spatial differences in evapotranspiration. As evapotranspiration is

highly heterogeneous, this causes an increase in variability of soil moisture. When the soil dries further the moisture distribution is influenced by spatial differences in the wilting point (which is less heterogeneous than evapotranspiration), thus decreasing the variability (Vereecken et al., 2007, Bell et al., 1980).

For the Rur catchment in Germany, Koyama et al. (2010b) observed an increasing variability of soil moisture with increasing mean soil moisture, based on in-situ measurements and ENVI-SAT-data. Based only on in-situ measurements of soil moisture, Korres et al. (2010) analysed the influence of different factors on the spatial and temporal variability of near-surface soil moisture on pasture and arable land in the fertile loess plain of the Rur catchment. Regarding spatial variability, soil type, stone content and differences in management practices were the dominating factors on arable land. The temporal variability on grassland was mainly influenced by the organic carbon content. In a study of spatial soil moisture patterns from different data sets (in-situ measurements, modelling and radar remote sensing) in the Rur catchment, Korres et al. (2015) identified the vegetation (in the form of temporal differences of evapotranspiration rates of the different crops), management (in the form of field size, planting dates, harvesting dates) and soil parameters (via porosity and field capacity) as main influences on the spatial variability of soil moisture in the fertile loess plain of the Rur catchment.

The multitude of influencing factors and the heterogeneity of soil moisture stresses the importance of using methods of remote sensing to derive spatially distributed soil moisture information as in-situ measurements can hardly be interpolated.

2.4 Surface Roughness and its Effect on SAR Backscatter

As stated in equation (2.39), surface roughness has an influence on the backscatter intensity from bare fields as well as from vegetated surfaces. This is due to the coherent nature of the SAR backscatter process that consists of the superposition of waves reflected by small scatterers at the earth surface. In that context, the sensitivity of the backscatter intensity to surface roughness depends on the wavelength of the SAR system, as only scatterers at scales comparable to the wavelength of the incoming wave will have an influence on the backscatter. Using longer wavelengths, the same target will appear much smoother than at smaller wavelengths (Marzahn and Ludwig, 2009). Regarding the SAR configuration, the backscatter is more sensitive to soil roughness at high incidence angles, whereas it is least affected by surface roughness at incidence angles between 7 and 15° (Ulaby and Batlivala, 1976). This applies of course also to the local incidence angle that is determined by local terrain. Regarding the polarization that is most sensitive to surface roughness, inconsistent results have been found in different studies

(Verhoest et al., 2008). For roughness measurements on bare soil fields in the Rur catchment, Koyama and Schneider (2010) found a strong correlation to the Crosspol Ratio (= crosspol / copol backscatter) and the dual-polarimetric Anisotropy. A relationship to Anisotropy has also been found by Cloude (1999).

Soil surface roughness can be defined as a varying height of the soil surface towards a reference surface (Ulaby et al., 1982). Generally, rough surfaces can be divided into deterministic (showing periodic irregularities) and randomly rough surfaces, with natural surfaces in general belonging to the latter (Davidson et al., 2000). Surface roughness can be considered as the sum of different components at different scales (Verhoest et al., 2008): 1) individual soil aggregates and grains, 2) soil clods, which represent the random component, 3) furrows and tillage rows and 4) topographic trends, which constitute the reference surface. For agricultural fields, the roughness depends on the direction that is considered: ploughed fields will have a different roughness in the row direction compared to the direction perpendicular to that (Verhoest et al., 2008). Therefore, the orientation of the rows relative to the look direction of the satellite is important. For application of SAR remote sensing on agricultural fields in the Rur catchment 2) and 3) of the before-mentioned components will be of importance as their scales are comparable to the scale of microwaves.

While extensive research is carried out for the correct characterization of surface roughness and its scale dependency, e.g. by using multiscale descriptions through fractal dimensions (Bennaceur et al., 2003), studies to retrieve surface soil moisture from SAR mostly prefer the root-mean-square height (rms) and the autocorrelation length (acl) as input to account for the roughness effect on backscatter (Rahman et al., 2007, Zribi et al., 2000, Verhoest et al., 2008). For that, rms and acl are usually measured in transects during field measurement campaigns (Bryant et al., 2007). The rms-height s [cm] is calculated for a one-dimensional surface roughness profile consisting of N points with surface height z_i [cm] as (Ulaby et al., 1982):

$$s = \sqrt{\frac{1}{N} [(\sum_{i=1}^N z_i^2) - N\bar{z}^2]}, \quad (2.40)$$

with

$$\bar{z} = \frac{1}{N} \sum_{i=1}^N z_i. \quad (2.41)$$

The autocorrelation length, acl [cm], describes the horizontal distance over which a surface profile is auto-correlated with a value larger than e^{-1} (Ulaby et al., 1982). For that, the autocorrelation function

$$acf = \sqrt{\frac{1}{N} [(\sum_{i=1}^{N-k} z_i - \bar{z})^2]}, \quad (2.42)$$

is calculated for measurement pairs with increasing distance. acl is then the distance in cm, at which acf results in e^{-1} with $e = 2.7183$ (Davidson et al., 2003).

To calculate effective roughness descriptors and compensate for the wavelength-dependent sensitivity, both s and acl have to be scaled to the actual wavelength using the wavenumber k within the following equation (Marzahn and Ludwig, 2009):

$$k_s = s \cdot k = s \cdot \frac{2\pi}{\lambda}. \quad (2.43)$$

2.4.1 Field Measurement of Surface Roughness

To calculate k_s or acl , field measurements of the surface height z_i have to be performed first. Amongst the different techniques to measure surface height (Thomsen et al., 2015) are:

- A pinboard: A device with moveable pins that is lowered to the ground surface. The position of the pins then follows the soil surface and the deviation from the reference surface can be either read out electronically or by photographing and digitizing the pin profile.
- A roller chain (e.g. a bicycle chain) with a known length is rolled out on the soil surface. The projected length is then measured and the rms height can be calculated from the difference of the measured length and the known length of the chain.
- A terrestrial 3D laser scanner that produces a 3-d model of the surface.
- Stereophoto images that are constructed by linking several images with slightly different viewing angles using a dedicated image processing software, to derive height differences.
- Depth-sensing technologies like Microsoft Kinect or Asus Xtion Pro, which originate from the gaming industry and send out infrared patterns that are reflected and recorded by a sensor. Depth information for the surface is achieved by a triangulation process (Marinello et al., 2015).

While a 3D laser scanner gives highest accuracy and resolution in surface description (Thomsen et al., 2015), it is not practical on vegetated areas. Like also stereophoto images or depth sensing technologies, it would rather measure the vegetation canopy than the soil surface. Apart from being time-consuming and impractical in the field, the spatial resolution of the two contact methods (roller chain and pinboard) seems to restrict their applicability (Thomsen et al., 2015) A laser profiler that is mounted on a moving platform and measures the distance to the ground

with a given frequency and over a transect with a known length can be used to estimate the surface height under vegetation, as long as the vegetation is not too dense. Therefore, it seems to be a practical and economic way to measure surface roughness on agricultural fields.

2.5 Vegetation Influence on SAR Backscatter

On a vegetated surface, besides surface roughness, the vegetation layer influences the microwave backscatter by its structure and water content. Vegetation causes a two-way attenuation of the backscatter from the land surface, and the vegetation contributes to total backscatter predominantly by volume scattering but also by surface scattering from the canopy itself or by double-bounce scattering induced by ground-stem interactions (Bindlish, 2001, Paloscia et al., 1999). While scattering mechanisms on vegetated areas are rather complex, several studies identified different characteristics of the scattering behaviour. In terms of polarization, HH polarized backscatter is more sensitive to surface scattering and HV polarized backscatter to volume scattering on vegetated areas. HV polarization is often used to determine vegetation parameters and HH polarization to retrieve ground parameters (Veloso et al., 2017). VV polarized backscatter correlates to both effects (Veloso et al., 2017). The backscatter component from the soil surface of VV polarized backscatter is only the dominant backscatter component for high incidence angles ($> 35^\circ$), as experiments under a wheat canopy have shown (Brown et al., 2003). Backscatter from the soil surface under wheat canopies at VH polarization is the dominant backscatter component for all but the largest incidence angles. Since the direct cross-pol backscatter from soil is assumed to be low, this is accredited to stem-ground double bounce scattering (Brown et al., 2003). Therefore, adding a crosspol-ratio VH/VV to the analysis of backscatter signatures, could reduce the effects of double bounce scattering from vegetation in the signatures (Veloso et al., 2017) and improve soil moisture retrieval.

In terms of incidence angle, high incidence angles increase the path length through vegetation and maximize the vegetation component of backscatter, whereas low incidence angles reduce the vegetation attenuation (Blaes et al., 2006). Therefore, high incidence angles are favourable for vegetation studies but less optimal for soil moisture studies.

Soil moisture retrieval from vegetated terrain requires the separation of the soil from the vegetation scattering components. SAR polarimetry allows addressing this separation by modelling individual scattering contributions (Jagdhuber et al., 2015). However, fields covered with vegetation have a rather complex scattering behaviour, so that model-based decompositions have been proposed to decompose the individual scattering contributions (Hajnsek et al., 2009,

Freeman and Durden, 1998, Yamaguchi et al., 2005). As modelling of the vegetation component is challenging, it is often approximated by a cloud of equally shaped particles, defined by the electromagnetic density of the volume layer, the shape, and the orientation distribution of the volume particles (Hajnsek et al., 2009). Such models are used in complex physical soil moisture retrieval models, whereas simpler retrieval schemes usually resort to using models like the Water-Cloud-Model (Attema and Ulaby, 1978) that assumes that a canopy can be represented by a cloud of randomly distributed water droplets, so that the vegetation dielectric constant is dominated by the dielectric constant of water. Empirically based soil moisture retrieval models usually use the sensitivity of the microwave backscatter to certain vegetation characteristics like Leaf-Area Index (LAI), biomass or vegetation water content (VWC) to correct for its influence on the backscatter even though they cannot describe the physical interactions between the incident waves and the vegetation. While vegetation cover with a closed canopy and high biomass amounts (like e.g. a forest) is likely to attenuate most of the incoming microwaves, Alexakis et al. (2017) even found an attenuating effect of sparse vegetation on VV polarized backscatter in Sentinel-1 data with high incidence angles. They used the optically derived Normalized Difference Vegetation Index (NDVI) for the correction of the vegetation influence to enable soil moisture retrieval.

In a sensitivity-study assessing the effects of bulk VWC in maize to the backscatter coefficient in different wavelengths and incidence angles, van Emmerik et al. (2015) found a strong influence of VWC on the backscatter coefficient in L- and C-Band. VWC affects the transparency of the vegetation canopy layer to the microwaves such that high VWC results in a low penetration capacity and vice versa. Still, for C-band backscatter in VV polarization even at larger incidence angles of 35° and 55° , the attenuated soil backscatter dominates the total backscatter. For HH polarization at 35° and 55° the total backscatter becomes increasingly sensitive to VWC, so that a decrease in VWC leads to a decrease in total backscatter. Therefore van Emmerik et al. (2015) concluded, that VV polarization is less sensitive to VWC than HH polarization in C-Band with high incidence angles. In general however, with increasing incidence angles, the total backscatter from the soil surface decreases, as the path through the vegetation increases and therefore a larger portion of the incoming microwaves will scatter and not reach the soil surface (van Emmerik et al., 2015, Joseph et al., 2010).

In contrast to interactions with crops on arable land, the backscatter mechanisms on grassland are different, as grassland shows less structure as for example wheat or maize fields that strongly influence the backscattered signal by vertically oriented stems (Brown et al., 2003).

Here, interactions between above-ground biomass, the thatch layer and the underlying soil constitute a challenge for the estimation of soil moisture (Koyama et al., 2010b, Martin et al., 1989). For differences in backscatter intensity on grassland fields with constant soil moisture content Dubois et al. (1995) found a strong influence of the varying amount of dry biomass with C-band backscatter. Therefore, they proposed an attenuation factor accounting for the dry biomass influence.

3 State of the Art of Soil Moisture Estimation with SAR

To estimate soil moisture from SAR remote sensing and thus to solve equation (2.39), generally three different approaches are known (Thoma et al., 2006b, Verhoest et al., 2008): physical or theoretical approaches, semi-empirical approaches, and empirical approaches.

Physical approaches are based on scattering models that predict the backscatter of microwaves based on their frequency, the incidence angle, surface roughness and the dielectric constant. Physical approaches are usually restricted to non-vegetated surfaces, as the influence on vegetation structure on the microwaves is complex.

In that context the Integral Equation Model (IEM) (Fung et al., 1992) is the most widely used model as it covers a broad range of wavelengths and surface parameters (Thoma et al., 2006). Other theoretical scattering models encompass the Small Perturbation Model (SPM) or the Kirchhoff Approximation (KA), which are described in detail by Fung (1994), Beckmann and Spizzichino (1987) and Ogilvy (1992). For the SPM, Hajnsek et al. (2003) developed an extension called the Extended or X-Bragg model to broaden the validity range of the SPM so that it is applicable for surface roughness values typically found on agricultural fields (Thoma et al., 2006, Koyama et al., 2010). Despite being spatially transferable in general, theoretical models are limited to the application on a restrictive range of input parameters, especially regarding surface roughness (Thoma et al., 2006a). Altogether, physical retrieval models require many input parameters that are typically not available under practical conditions.

A so-called hybrid approach is applied to vegetated areas and uses polarimetric decomposition, to identify the surface or Bragg scattering term and distinguish it from volume scattering, induced by the vegetation layer. The backscatter is then in a next step corrected for surface and vegetation influences to retrieve soil moisture (Jagdhuber et al., 2012, Jagdhuber et al., 2014b). Those approaches are so far limited to full polarimetric SAR or SAR systems measuring both co-polarized channels (Jagdhuber et al., 2014a).

Semi-empirical approaches add empirical data to physical considerations and extend theoretical models, to minimize the amount of input data (Thoma et al., 2006).

They improve the results of theoretical models and widen their possible area of application on the one hand, but require many field measurements on the other hand. Examples of semi-empirical models can be found in Oh et al. (1992), Oh (2004), Dubois et al. (1995) and Baghdadi et al. (2004). Those models can be applied to full polarimetric data and dual-polarimetric co-polarized data but are restricted to bare-soil conditions. Koyama (2012) tested the Oh- and the Dubois-model for the bare soil case on L-band data of the Rur catchment but found large under-

and overestimation respectively. Therefore, Koyama and Schneider (2010) and Koyama (2012) developed a new semi-empirical retrieval scheme for L-band SAR data from bare-soil and under vegetation, that can be applied to dual-polarimetric data with only one co- and one cross-pol channel. It uses the dual-pol $H2\alpha$ decomposition, to increase the observation space for the semi-empirical retrieval of soil moisture and vegetation parameters based on in-situ data.

Empirical or regression based approaches enable the direct retrieval of soil moisture from SAR backscatter. They are based on equations like equation (2.39), which directly calculates soil moisture in case the other influencing factors are known or constant. To assess the influences of soil moisture, vegetation and roughness parameters on SAR backscatter, they need an extensive data basis of ground measurements. An additional downside of purely empirical approaches besides the extensive field measurements is that they are usually restricted to their development region or need recalibration (Thoma et al., 2006, Koyama et al. 2010). For example, when applying the empirical approach by Rombach and Mauser (1997), which was developed for a research area in Bavaria in southern Germany, to our research area in western Germany in previous work, a systematic overestimation was observed that needed recalibration of the approach. Therefore, without sufficient ground truth measurements of soil moisture and vegetation for calibration, the application of empirical approaches to different research areas is prone to errors.

In contrast to physical approaches, empirical approaches can be used to retrieve soil moisture under vegetation and are simple to implement. They can be applied also to single-channel SAR data and do not necessarily need data from polarimetric systems. Amongst the empirical approaches that have been developed in the last years are: Koyama and Schneider (2010), Rombach and Mauser (1997), Quesney et al. (2000), Loew et al. (2006) and Álvarez-Mozos et al. (2005). Recently, several empirical approaches were developed and tested that employed an Artificial Neural Network (ANN) to optimize retrieval algorithms (Paloscia et al., 2013, Alexakis et al., 2017, Paloscia et al., 2010, Pasolli et al., 2011).

A different category of procedures includes **time-series or change-detection based approaches** that concentrate more on the retrieval of qualitative than quantitative soil moisture information but require few input parameters. They exploit multiple SAR acquisitions rather than using single acquisitions. Usually, instead of giving discrete soil moisture values, they produce a relative index ranging between high and low amounts of soil moisture. The best-known soil moisture index approach is the method developed by Wagner et al. (Wagner et al., 1999a, Wagner et al., 1999b) that uses information from different incidence angles as provided by the ERS scatterometer or the ASCAT instrument on METOP-A to retrieve soil moisture

operationally on a global scale but with low spatial resolution of about 25 km. The approach has been extended to ENVISAT ASAR data with 1 km resolution but recommended spatial averaging to 3-10 km to reduce noise (Pathe et al., 2009). Tomer et al. (2015) tested a time-series based approach on Radarsat-2 data and the delta index model (Thoma et al., 2006a, Sano et al., 1998) used pairs of acquisitions from ERS-2 and Radarsat-1 to evaluate the soil moisture of a wet scene relative to a dry reference scene. Qualitative soil moisture information as provided by such approaches is interesting for monitoring soil moisture changes e.g. for drought monitoring or to observe soil moisture patterns and their temporal evolution. The SMOSAR-algorithm (Balenzano et al., 2013) was developed on L-band ALOS-1 and X-Band COSMO-Sky-Med data and transforms time-series of single or dual-pol SAR images over agricultural areas or short vegetation areas to quantitative soil moisture maps with 1 km resolution. It has recently been adapted to Sentinel-1 data (Mattia et al., 2015) in southern Italy.

4 Materials & Methods: Analysing two Methods to Derive Land Surface Parameters from C-Band SAR

Depending on the intended application and the available data, different approaches to derive soil moisture and vegetation information from C-band SAR are possible.

If the goal is to generate a long time-series of SAR-derived soil moisture data for pattern analysis, such soil moisture information is only available from historic datasets, like the ERS image archives. For such datasets as well as for data from remote areas, usually no ground truth information of soil moisture and vegetation parameters is available, so that only qualitative information will be retrievable.

If the goal is to derive high-resolution soil moisture and vegetation information from state-of-the-art C-band satellites like Sentinel-1, dedicated ground truth measurements can be performed, to develop a quantitative soil moisture retrieval scheme. The intent of developing such high-quality soil moisture and vegetation retrieval schemes is to develop routines to monitor soil moisture and vegetation parameters e.g. for precision farming.

Obviously, two different approaches are needed to meet the requirements of the two application intents and will be presented in this thesis. The first approach is a qualitative soil moisture index, ranging from low to high amounts of soil moisture that is based on a time-series of ERS-1 & -2 images and corresponding land use maps. The second approach is empirical and uses an extensive set of ground measurements of soil moisture and vegetation parameters corresponding to S1A acquisitions. This chapter introduces the datasets that are used for the two approaches, the study area and the two methods.

4.1 Study Area

The study area is the catchment of the river Rur, located at the German-Belgium-Dutch border region (Figure 4.1). It is the research area of the Transregional Collaborative Research Centre (TR) 32: Patterns in Soil-Vegetation-Atmosphere-Systems.

From its source in Belgium to the outlet into the Maas River in the Netherlands, the river Rur has a length of approximately 165 km. Almost 90 % of the catchment area is on German territory, the other parts belong to Belgium and the Netherlands. The catchment covers an area of approximately 2354 km² and can be separated into two major landscape units, the low mountain range with Eifel and Hohes Venn in the south and the flat fertile loess plain of the Jülich-Zül-picher Boerde in the north (Bogena et al. 2005).

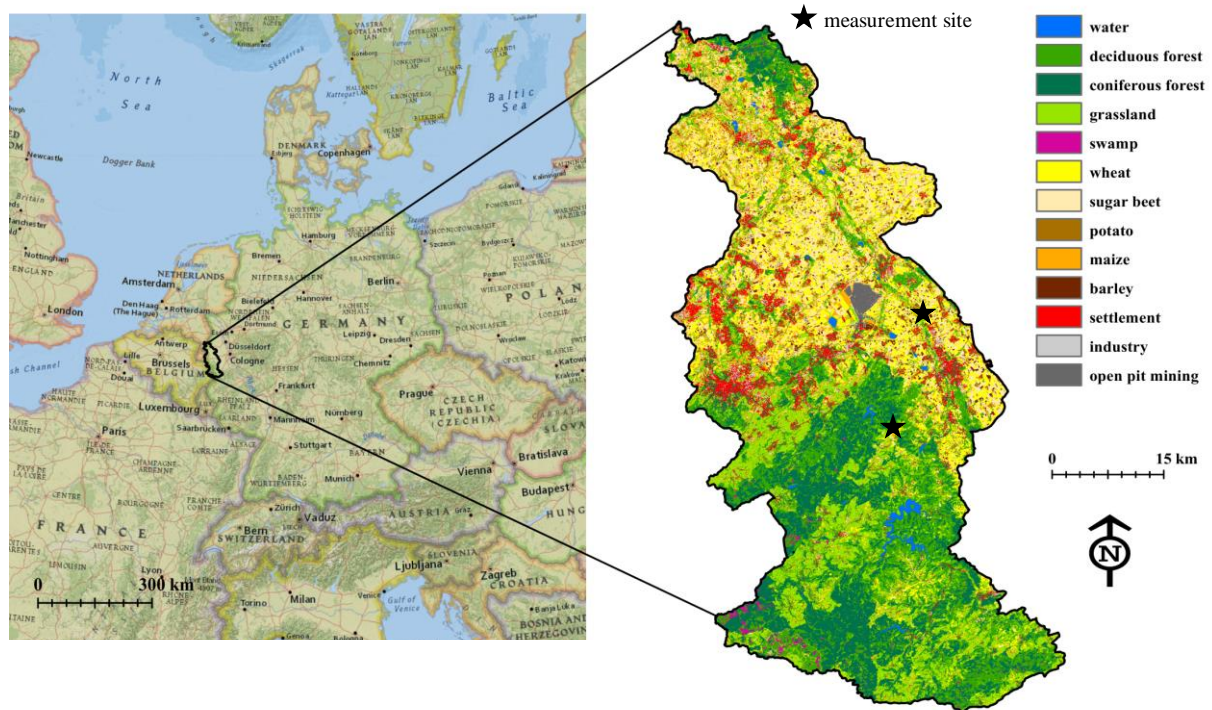


Figure 4.1. Catchment of the River Rur with main land use types 2001 (Bogena et al. 2005). The northern part of the catchment, a fertile loess plain with mainly agriculture and the measurement site Selhausen can clearly be distinguished from the southern part, the low mountain range of the Eifel with dominating grasslands and forests and the test site Hürtgenwald.¹

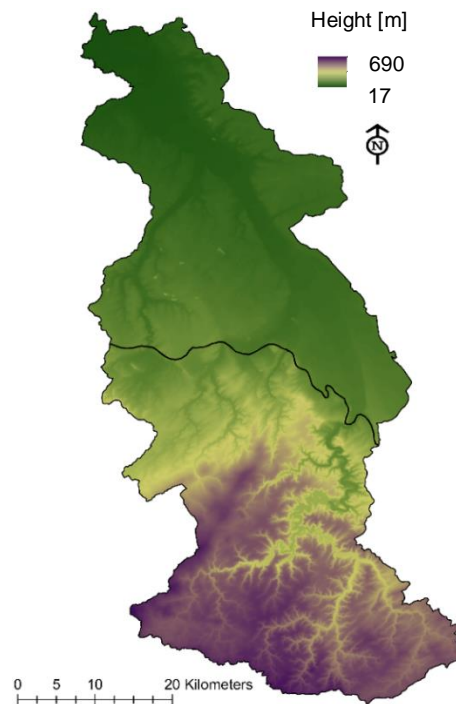


Figure 4.2. Map of the Digital Elevation Model of the Rur catchment without anthropogenic structures (sciland GmbH, 2010). The black line shows the border between the fertile loess plain in the north and the low mountain range of the Eifel in the south.

¹ The background map was created using ArcGIS® software by Esri. ArcGIS® and ArcMap™ are the intellectual property of Esri and are used herein under license. Copyright © Esri.

Major parts of the Rur catchment are agriculturally used, especially in the fertile loess plain, where arable land covers 47 % of the total area (Reichenau et al., 2016). In the low mountain range, forests and grasslands are the dominant land use classes. 5% of the catchment area is built-up area and Aachen and Düren are the major cities with 260.454 and 92.486 inhabitants, respectively (Statistisches Bundesamt, Zensus 2011). In the centre of the catchment, the soft coal open pit mine Inden constitutes a striking feature (Figure 4.1). The elevation reaches from 17 m above sea-level in the floodplains of the Boerde up to 690 m in the Eifel (Figure 4.2).

4.1.1 Geology and Soils

The Rur catchment is an interesting research area, since it is situated on the boarder of two major German landscape units: the Lower Rhine Basin (Niederrheinische Bucht) in the north and the Rhenish Massif (Rheinisches Schiefergebirge) in the south (Brunotte et al., 1994). The northern part of the catchment – the Jülich-Zülpicher-Boerde belongs to the landscape unit of the Lower Rhine Basin and the southern part – the Eifel belongs to the Rhenish Massif (Liedtke and Marcinek, 2002).

The Rhenish Massif is the oldest part of the federal state of North Rhine Westphalia (NRW) and consists of the Eifel on the left side of the river Rhine and Bergisches Land, Sauerland, Siegerland and Wittgensteiner Land on the right side of the river Rhine in NRW (Geologischer Dienst NRW, 2016). In total, the Rhenish Massif and its extension in the Ardennes stretches from Mons in Belgium via the Eifel and Westerwald to the Kellerwald near Bad Wildungen (Meschede, 2015). The basement rock developed during variscan orogeny (Liedtke and Marcinek, 2002) in Palaeozoic and has been mainly uplifted in the Quaternary, while the Lower Rhine Basin, that had already developed as a transform fault in the Tertiary, subsided. The Rhenish massif with the Eifel consists of Devonian and Carboniferous sedimentary rocks mainly encompassing sandy slate, sandstone, greywacke, quartzite and pure slate (Meschede, 2015). The bedrock in the Eifel is characterized by low permeability and small groundwater runoff (Montzka et al., 2013). The characteristic soils for the Eifel are shallow Cambisols and Leptosols.

The Lower Rhine Basin is a landscape of moraines created by older glaciation from the Saale Ice Age that reached to the boarder of the low mountain range (Liedtke and Marcinek, 2002, Meschede, 2015). It is characterized by loess, which accumulated on Tertiary and Quaternary depositions of the rivers Rhine and Meuse (Montzka et al., 2013, Brunotte et al., 1994). The sediment loess was deposited during the Weichsel Ice Age in the former periglacial area in front of the glaciers by aeolian transport and originated from the moraine area and the glacial outwash

plain (Brunotte et al., 1994). The loess forms a so-called loess-belt across Europe and marks, with a width of 20-80 km, the border between low mountain ranges and North German basin. Due to its high chalk content, extremely fertile soils developed on the loess (Liedtke and Marcinek, 2002). The soils are dominantly luvisols that have a good air- and water budget and optimal nutrient supply. Therefore they are used intensively for agriculture (Brunotte et al., 1994).

The dominant soil textural class in the Rur catchment is strongly clayey silt, with sandy soils in the very northern part of the Rur catchment, which belongs to the Netherlands.

4.1.2 Climate

The climate in the Rur catchment is oceanic with cool summers and mild winters. Precipitation occurs throughout the whole year and originates mainly from cyclones brought up by the west wind drift. According to the Koeppen-Geiger classification (Kottek et al., 2006) the climate in the watershed is humid and temperate without dry season and with warm summer (Cfb). In summer and winter, there is also a dry-warm and cold-warm influence of continental anticyclones. According to the main pathway of the cyclones, the main wind direction is from the west. During the influence of continental anticyclones, wind occurs also from the east (Brunotte et al., 1994).

The precipitation distribution is influenced by the relief. The Rhenish Massif that runs diagonal to the predominant wind direction provokes elevation effects. Therefore, westerly winds descend from Hohes Venn and Eifel in the southern area of the Jülich-Zülpicher Boerde and warm adiabatically. This results in warm and dry air (Brunotte et al., 1994). Consequently, within the two major landscape units, significant differences in the rainfall distribution can be observed. Whereas rainfall is homogenous in the northern part of the catchment, ranging from 700 to 900 mm/a, the rainfall patterns in the southern part of the catchment are more heterogeneous, due to the elevation effects. Here, rainfall ranges between 700 mm/a windward and 1200 mm/a downwind (Bogena et al., 2005).

4.1.3 Test Sites

For the intensive field measurements corresponding to S1A acquisitions, two test sites have been established. The first measurement site “Selhausen” is situated in the Boerde Region close to the city of Düren and the village Selhausen (Figure 4.1). It is a pure crop test site and is highly instrumented by multiple projects of TR32. Main soils that are found on the Selhausen measurement sites are Cambisol and Luvisol with a high amount of coarse alluvial deposits of

a former river terrace (Montzka et al., 2013). Our field measurement campaigns took place on five selected fields each in 2015 and 2016 (Figure 4.3). Cooperating farmers cultivated these fields conventionally and granted us access for the measurement campaigns.

The second measurement site “Hürtgenwald” is a mixed test site in the Eifel Region (Figure 4.3) near the village of Kleinhau. Here, crops as well as pasture can be found. In 2015 and 2016, four fields each year, cultivated by a cooperating farmer, were measured during campaigns (Figure 4.3). An in-depth description of the measurement campaigns is given in chapter 4.5.

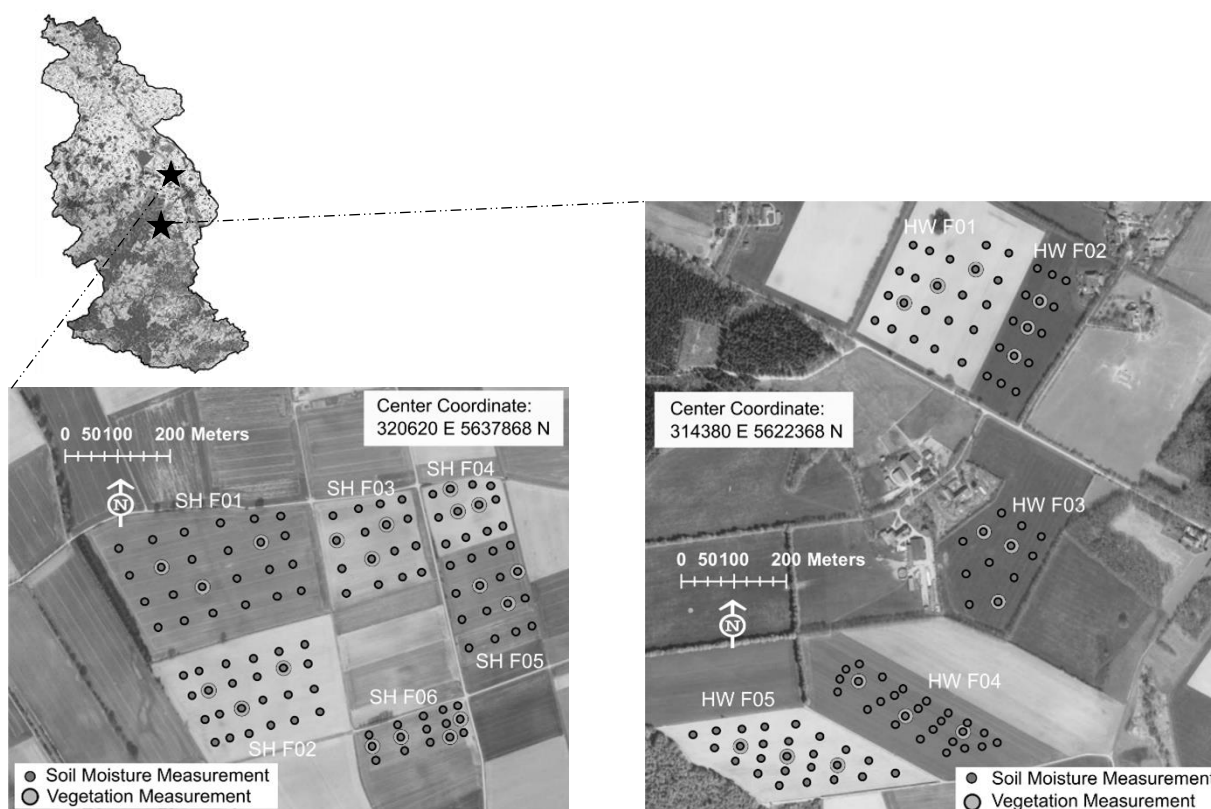


Figure 4.3. Schematic overview of measurement sites Selhausen (left) and Hürtgenwald (right). Coordinates are given in UTM (WGS84) Zone 32U.²

4.2 SAR Data

This chapter describes the SAR data that were used in the two studies and is subdivided into a chapter on ERS data and a chapter on the S1A data.

4.2.1 ERS-SAR Data

In the first part of the study, we used 84 SAR Single Look Complex (SLC)-images from the ERS-1 and -2 satellites, covering most parts of the catchment area. ERS-1 and -2 are twin satellites developed and operated by ESA from 1991-2000 and from 1995-2011 respectively.

² The background layer was created using ArcGIS® software b Esri. ArcGIS® and ArcMap™ are the intellectual property of Esri and are used herein under license. Copyright © Esri.

Table 4.1. Overview of the 84 ERS-acquisitions. ERS-1 acquisitions are given in italics to be differentiated from ERS-2 acquisitions.

| Date | Satellite | Pass | Date | Satellite | Pass | Date | Satellite | Pass |
|-------------------|--------------|-----------------|-------------------|--------------|----------------|------------|-----------|----------|
| <i>1995-03-17</i> | <i>ERS-1</i> | <i>397 asc</i> | <i>1996-10-22</i> | <i>ERS-1</i> | <i>29 asc</i> | 2000-04-11 | ERS-2 | 108 desc |
| <i>1995-04-11</i> | <i>ERS-1</i> | <i>29 asc</i> | 1996-20-23 | ERS-2 | 29 asc | 2000-04-21 | ERS-2 | 258 asc |
| <i>1995-04-27</i> | <i>ERS-1</i> | <i>258 asc</i> | 1997-03-18 | ERS-2 | 108 desc | 2000-05-10 | ERS-2 | 29 asc |
| 1995-05-22 | ERS-2 | 108 desc | 1997-03-28 | ERS-2 | 258 asc | 2000-05-16 | ERS-2 | 108 desc |
| 1995-06-02 | ERS-2 | 258 asc | 1997-04-16 | ERS-2 | 29 asc | 2000-05-26 | ERS-2 | 258 asc |
| <i>1995-06-20</i> | <i>ERS-1</i> | <i>29 asc</i> | 1997-04-21 | ERS-2 | 108 desc | 2000-06-20 | ERS-2 | 108 desc |
| <i>1995-07-06</i> | <i>ERS-1</i> | <i>258 asc</i> | <i>1997-05-20</i> | <i>ERS-1</i> | <i>29 asc</i> | 2000-07-25 | ERS-2 | 108 desc |
| 1995-07-07 | ERS-2 | 258 asc | 1997-05-21 | ERS-2 | 29 asc | 2000-08-29 | ERS-2 | 108 desc |
| <i>1995-07-31</i> | <i>ERS-1</i> | <i>108 desc</i> | 1997-05-27 | ERS-2 | 108 desc | 2000-09-08 | ERS-2 | 258 asc |
| 1995-08-01 | ERS-2 | 108 desc | 1997-06-06 | ERS-2 | 258 asc | 2000-10-03 | ERS-2 | 108 desc |
| <i>1995-08-29</i> | <i>ERS-1</i> | <i>29 asc</i> | 1997-07-01 | ERS-2 | 108 desc | 2001-03-27 | ERS-2 | 108 desc |
| <i>1995-09-04</i> | <i>ERS-1</i> | <i>108 desc</i> | 1997-08-05 | ERS-2 | 108 desc | 2001-05-01 | ERS-2 | 108 desc |
| <i>1995-10-03</i> | <i>ERS-1</i> | <i>29 asc</i> | 1997-08-15 | ERS-2 | 258 asc | 2001-06-05 | ERS-2 | 108 desc |
| 1995-10-04 | ERS-2 | 29 asc | 1997-09-09 | ERS-2 | 108 desc | 2002-04-16 | ERS-2 | 108 desc |
| <i>1996-03-26</i> | <i>ERS-1</i> | <i>29 asc</i> | <i>1997-10-07</i> | <i>ERS-1</i> | <i>29 asc</i> | 2002-04-26 | ERS-2 | 258 asc |
| 1996-03-27 | ERS-2 | 29 asc | 1999-03-23 | ERS-2 | 108 desc | 2002-05-31 | ERS-2 | 258 asc |
| <i>1996-04-11</i> | <i>ERS-1</i> | <i>258 asc</i> | <i>1999-04-20</i> | <i>ERS-1</i> | <i>29 asc</i> | 2002-06-25 | ERS-2 | 108 desc |
| 1996-04-12 | ERS-2 | 258 asc | 1999-04-27 | ERS-2 | 108 desc | 2002-07-05 | ERS-2 | 258 asc |
| <i>1996-04-30</i> | <i>ERS-1</i> | <i>29 asc</i> | 1999-05-07 | ERS-2 | 258 asc | 2002-07-30 | ERS-2 | 108 desc |
| 1996-05-01 | ERS-2 | 29 asc | 1999-05-26 | ERS-2 | 29 asc | 2002-08-09 | ERS-2 | 258 asc |
| <i>1996-06-04</i> | <i>ERS-1</i> | <i>29 asc</i> | 1999-06-01 | ERS-2 | 108 desc | 2002-09-03 | ERS-2 | 108 desc |
| <i>1996-06-10</i> | <i>ERS-1</i> | <i>108 desc</i> | <i>1999-06-10</i> | <i>ERS-1</i> | <i>258 asc</i> | 2002-10-08 | ERS-2 | 108 desc |
| <i>1996-06-20</i> | <i>ERS-1</i> | <i>258 asc</i> | 1999-07-06 | ERS-2 | 108 desc | 2003-03-07 | ERS-2 | 258 asc |
| 1996-06-21 | ERS-2 | 258 asc | 1999-07-16 | ERS-2 | 258 asc | 2003-04-01 | ERS-2 | 108 desc |
| <i>1996-07-09</i> | <i>ERS-1</i> | <i>29 asc</i> | 1999-08-04 | ERS-2 | 29 asc | 2003-05-06 | ERS-2 | 108 desc |
| <i>1996-07-25</i> | <i>ERS-1</i> | <i>258 asc</i> | 1999-08-10 | ERS-2 | 108 desc | 2003-06-10 | ERS-2 | 108 desc |
| 1996-08-14 | ERS-2 | 29 asc | 1999-09-14 | ERS-2 | 108 desc | 2003-07-15 | ERS-2 | 108 desc |
| 1996-08-30 | ERS-2 | 258 asc | 2000-03-07 | ERS-2 | 108 desc | 2003-09-23 | ERS-2 | 108 desc |

The SAR-instrument on both satellites is included in the Active Microwave Instrument (AMI) and works in C-band (5.6 cm / 5.3 GHz) and in VV-polarization. ERS-1 and -2 operated with a fixed incidence angle of 23°. The SAR data was processed and georeferenced to quadratic 20 m pixels. They represent the backscattering coefficient sigma nought. All SAR processing tasks were performed with the software package SARscape 5.0 (sarmap SA, Purasca, Switzerland) for SAR processing and with ENVI 5.1 (Exelis Visual Information Solutions, Inc., Boulder, USA).

Table 4.1 gives an overview of the ERS images that have been used in the analysis. Amongst them are images acquired in ascending and in descending node, thus incorporating different acquisition geometries. As only relative backscatter intensities are relevant for this study, it has been tested whether there are systematic differences between the distribution of means and variances of backscatter intensities for each orbit. Statistical f- and t-tests that were performed with the software R (R Core Team 2015), showed no significant differences between the distributions of backscatter intensities from ascending and descending orbits. Similar tests have been performed between ERS-1 and -2 data and showed no significant differences. Hence, we used images from ascending and descending orbits and from ERS-1 and -2 jointly.

4.2.2 Sentinel-1A Data

Sentinel-1 A and B are twin C-band SAR satellites by ESA from the Copernicus Program (formerly known as GMES – Global Monitoring for Environment and Security), that is headed by ESA and the European Commission (EC). They are heritage missions to the former ESA C-Band SAR Missions ERS-1 & -2 and ENVISAT. Sentinel-1A has been launched on 2014-04-03 and Sentinel-1B on 2016-04-25. Operating in constellation, they offer a repeat cycle of six days. The future launch of similar Sentinel-1C and D satellites has been announced to guarantee data availability for the next years. For simplification, we will talk only about Sentinel-1 for the rest of the text, encompassing both Sentinel-1A and 1B when not stated otherwise. Sentinel-1 employs a sun-synchronous near-polar orbit with 175 orbits in a 12 day repeat cycle. The SAR instrument operates in C-band with a centre frequency of 5.4 GHz (ca. 5.5 cm wavelength) and either dual HH-HV (for sea ice and polar areas) or VV-VH (otherwise) polarization or single HH or VV polarization. The sensor is right looking with an incidence angle between 20-46° depending on the range position. It allows four different acquisition modes: Stripmap, Interferometric Wide Swath (IW), Extra Wide Swath and Wave.

We use exclusively data from the IW mode. It is the predefined observation mode over land, as given by the ESA high-level observation plan and therefore the only acquisition mode that is available for our study area. IW mode covers a swath width of 250 km, divided into three sub swaths. A new form of ScanSAR imaging, that is the conventional imaging mode to allow wide swaths, is used for acquisitions in IW mode: TOPSAR (Terrain Observation with Progressive ScanSAR). It steers the beam in azimuth direction for each burst, in addition to steering the beam in range direction as for conventional ScanSAR. Hereby homogenous image quality throughout the whole swath shall be guaranteed (Sentinel-1 Team, 2013).

For the second part of the study we used 21 S1A acquisitions with accompanied field measurements (Table 4.2). The S1A acquisitions were chosen based on the following criteria: 1) Acquisitions from the same orbit/track to ensure stable radar geometry, 2) ascending orbits that provide acquisitions in the evening so that measurements can be performed in advance during the day and to avoid dew effects that can occur during early morning acquisitions, 3) same-day acquisition of at least one other satellite (Radarsat-2 or ALOS-2) to create synergies. This led to a 24-day cycle of soil moisture and plant measurements in general from which we departed in case of precipitation occurrence (Table 4.2 & Table 4.3).

Table 4.2. Overview of Sentinel-1A acquisitions with corresponding measurement campaigns. Precipitation information for Selhausen from a climate station³. Precipitation information for Hürtgenwald from observations during measurement campaigns. The dates shaded in grey are those that are later on excluded from the analysis.

| Date | Acquisition Time (GMT) | Precipitation between start of measurements and acquisition | |
|------------|------------------------|---|---|
| | | Selhausen | Hürtgenwald |
| 2015-03-28 | 17:24 | 2 mm / campaign aborted | campaign aborted |
| 2015-04-21 | 17:24 | - | - |
| 2015-05-15 | 17:24 | - | - |
| 2015-07-02 | 17:24 | - | - |
| 2015-07-26 | 17:24 | 1.8 mm between 18:30-19:30 | light precipitation after measurements |
| 2015-08-19 | 17:24 | - | - |
| 2015-09-12 | 17:24 | 6.8 mm between 14:30-18:30 | light precipitation between 15:00-15:15 |
| 2015-10-06 | 17:24 | 0.3 mm / measurement campaign aborted | no measurements performed |
| 2015-10-18 | 17:24 | - | - |
| 2015-10-30 | 17:24 | - | - |
| 2015-11-23 | 17:24 | - | - |
| 2016-03-22 | 17:24 | - | Light precipitation between 14:05-14:21 |
| 2016-03-29 | 17:16 | 1.5 mm between 15:50-16:20 / measurement aborted | no measurements performed |
| 2016-04-15 | 17:24 | - | - |
| 2016-05-09 | 17:24 | - | - |
| 2016-06-02 | 17:24 | - | - |
| 2016-07-20 | 17:24 | - | - |
| 2016-08-13 | 17:24 | - | - |
| 2016-09-06 | 17:24 | - | - |
| 2016-09-30 | 17:24 | - | - |
| 2016-11-17 | 17:24 | - | - |

All acquisitions are from the same ascending orbit with an acquisition time at 17:24 GMT. Images have been processed to 15 m ground resolution using the Sentinel-1 Toolbox of the ESA Sentinels Application Platform (SNAP) 5.0 (ESA, 2017) and the before mentioned Digital Elevation model of the Rur Catchment. The corresponding processing chain is described in detail in chapter 4.8.

³Data from Eddy Covariance / Climate Station Selhausen from the data portal of the TERENO project (teodor.icg.kfa-juelich.de).

Apart from the acquisition of 2016-03-29, that has been chosen outside of the regular measurement campaign cycle, all acquisitions have the same orbit and track (88/14) and thus a constant incidence angle ranging between 38.6-40.8 ° in the Rur catchment. This ensures a stable radar geometry. Four out of the 21 acquisition/measurement dates had to be discarded because precipitation occurred in the time frame between field measurements and satellite acquisition leading to a mismatch of the soil moisture state during field and satellite observations (Table 4.2).

4.3 Land Use Information

To account for the vegetation impact on the backscattering coefficient in the analysis of ERS data, land use information is needed. For the period of the historic ERS datasets, Landsat 5 Thematic Mapper (TM) and Landsat 7 Enhanced Thematic Mapper Plus (ETM+) images were used to derive annual land use maps. Landsat 5 TM and 7 ETM+ are multispectral optical and thermal sensors by NASA. Land use information, which is needed for the land use classifications, has been acquired through interviews with farmers and the analysis of their field and management records. Utilizing a maximum likelihood classification, land use maps for every year were produced with a spatial resolution of 30 m. Since C-band penetrates only short vegetation types and bare soil, we concentrate on agricultural areas. Built-up areas, forests and water bodies are excluded from our analysis.

Within the agricultural areas, we differentiate between cereal, sugar beet and grassland, as we assume their roughness and dielectric properties are significantly different. Those are the main agricultural land use types in the Rur catchment, with a coverage of 15% (cereals), 13% (sugar beet) and grassland (15%) in 2001 (Figure 4.1) in the Rur catchment. Maize, is of minor importance compared to the aforementioned land use classes, but still covers 6% of the catchment area (Montzka 2008). Nevertheless, since the ground truth data only comprises very few maize fields, resulting in many misclassifications, maize fields were masked from the final land use classifications. Due to missing ground truth data between 1991 and 1994 and missing cloud-free Landsat data for 1998, land use information is only available from 1995-1997 and 1999-2003. The overall accuracy of the land use maps for all years is between 82.4 % (for 1999) and 99.4 % (for 2001), and the Kappa-Coefficient is between 0.59 (for 1999) and 0.98 (for 2001). More detailed information on the land use maps is given in the appendix.

No land use map is needed for the empirical approach that uses Sentinel-1 data, because we concentrate on data from the measurement sites. Therefore, the land use types for these fields are known.

4.4 Soil Moisture and Precipitation Data for the Soil Moisture Index Approach

No in-situ surface soil moisture data is available for the period of the ERS time-series. Therefore, precipitation data is used to evaluate the soil moisture index approach. The German Weather Service (DWD) provides daily-mean precipitation datasets for several stations within the Rur catchment over a long period. Ten stations, shown in Fig. 8, recorded data over the whole period of 1995-2003. The data is available through the German Weather Service (DWD Climate Data Center (CDC)).

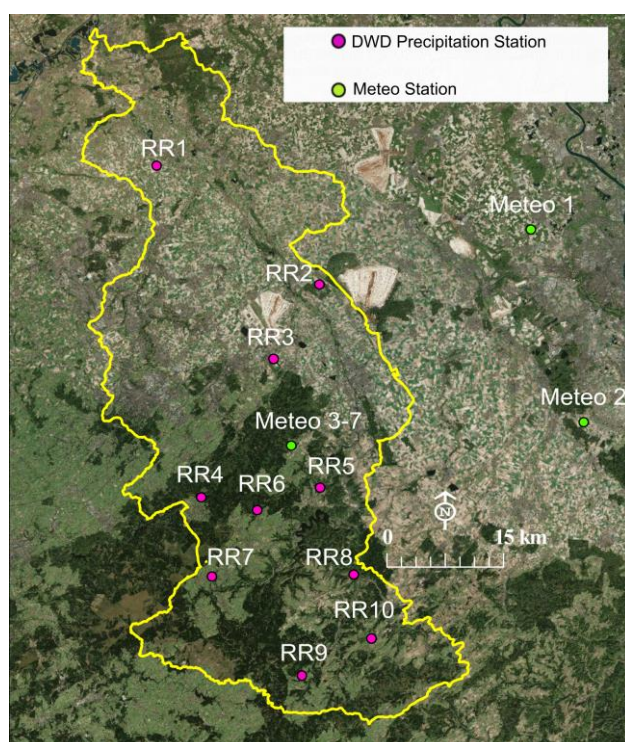


Figure 4.4. Overview of the locations of the precipitation measurements as provided by DWD with corresponding station numbers and the locations of the meteo stations.⁴

To evaluate the soil moisture index approach, data from seven meteo stations (Campbell Scientific, Logan USA) has been used. The stations recorded continuous precipitation heights and soil moisture at 5 cm depth. Volumetric soil moisture is measured with CSC616 (Campbell Scientific, Logan USA) soil moisture sensors, using a time-domain method and precipitation is measured with an ARG100 raingauge (Campbell Scientific, Logan USA). The stations were set up on agricultural fields from cooperating farmers in the Rur catchment. Daily precipitation

⁴ The background layer was created using ArcGIS® software by Esri. ArcGIS® and ArcMap™ are the intellectual property of Esri and are used herein under license. Copyright © Esri.

sums and soil moisture were calculated. The measurements provided by the seven meteorological stations, were checked for consistency and homogeneity.

4.5 Field Measurements of Soil Moisture, Vegetation, and Surface Roughness for the Quantitative Approach

Table 4.3. Overview of the field measurements and corresponding SAR-Acquisitions. WW = Winter Wheat, WB = Winter Barley, GL = Grassland, DI = Spelt, SB = Sugar Beet, TR = Triticale, MA = Maize, TSX = TerraSAR-X

| Field measurements | SAR Acquisitions | | | | Soil moisture measurements | Plant measurements |
|--------------------|------------------|------------|--------|-----|----------------------------|---|
| | S1A | Radarsat-2 | ALOS-2 | TSX | | |
| 2015-03-28 | ✓ | ✓ | | | ✓ | WW, GL |
| 2015-04-21 | ✓ | | | | ✓ | WW, DI, GL, TR |
| 2015-05-15 | ✓ | ✓ | | ✓ | ✓ | WW, DI, SB, MA, GL, TR |
| 2015-07-02 | ✓ | ✓ | ✓ | | ✓ | WW, DI, SB, MA, GL, TR (crop residues) |
| 2015-07-26 | ✓ | ✓ | | | ✓ | WW (crops, + crop residues), DI (crop residues), SB, MA, GL |
| 2015-08-19 | ✓ | ✓ | | | ✓ | WW (crop residues), SB, MA, GL |
| 2015-09-12 | ✓ | ✓ | | | ✓ | MA, GL, SB, crop residues: on 10.09.15 |
| 2016-10-06 | ✓ | ✓ | | | ✓ | SB, crop resid., MA, GL |
| 2015-10-18 | ✓ | | | | ✓ | |
| 2015-10-30 | ✓ | ✓ | | | ✓ | SB, WW (residues + new sprout), DI (crop residues), MA (residues), GL |
| 2015-11-23 | ✓ | ✓ | | | ✓ | WW (resid. + n. sprout), DI (resid. + n. sprout), MA (resid.), GL |
| 2016-03-22 | ✓ | ✓ | | | ✓ | WW, WB, resid., GL |
| 2016-03-29 | ✓ | | | | ✓ | |
| 2016-04-15 | ✓ | ✓ | | | ✓ | WW, WB, TR, GL |
| 2016-05-09 | ✓ | ✓ | | | ✓ | WW, WB, TR, SB, GL |
| 2016-06-02 | ✓ | | | | ✓ | WW, WB, TR, SB, GL, MA |
| 2016-07-20 | ✓ | ✓ | | | ✓ | MA, SB, GL, WB: on 21.7.16; |
| 2016-08-13 | ✓ | ✓ | | | ✓ | MA, GL, WB, SB: on 12.8.16; some samples destroyed |
| 2016-09-06 | ✓ | ✓ | | | ✓ | SB, n. sprout, resid.: on 7.9.16 |
| 2016-09-30 | ✓ | ✓ | | ✓ | ✓ | SB, n.sprout, MA, GL |
| 2016-11-17 | ✓ | | | | ✓ | New sprout, GL |

To supply in-situ data simultaneously to S1A acquisitions, dedicated field measurement campaigns were performed. The dates for the field measurement campaigns depended on the S1A acquisitions, therefore we performed soil moisture and plant measurements about every 24 days

(Table 4.3). On some dates plant measurements had to be performed one day before or after the S1A acquisition, due to planning conflicts. In 2015 and 2016, we measured on five fields in Selhausen and four fields in Hürtgenwald, respectively. On each test site, we had to change the location of one field due to a change in land use in 2016.

4.5.1 Soil Moisture Measurements

On each field, we measured soil moisture at up to 26 locations (Figure 4.3) with each location consisting of six single measurements. The six single measurements, for which we used handheld FDR-probes, were performed within a radius of one meter at most around the measurement location. The purpose of six single measurement instead of only one measurement per location, is to account for the small scale heterogeneity of soil moisture and possible measurement errors. On each measurement location, the mean, the median and the standard deviation of the six single soil moisture measurements was calculated for the later analyses.

According to the length of the metal conductors of the FDR-probe, that are inserted into the soil, the measured soil moisture represents an average value for the uppermost six cm of the soil column, which is well in line with the maximum C-Band penetration depth that is up to five cm for dry soil (Ulaby et al., 1982, Bruckler et al., 1988). Altogether each measurement day sums up to more than 1000 single soil moisture measurements. On each measurement point we noted the GPS coordinates. Measurement points with erroneous coordinates were checked manually and either assigned to the mean of the coordinates that have been noted for the same location on other measurement days or were discarded.

Our dataset encompasses very dry to very wet soil moisture conditions. The minimum mean soil moisture that has been measured is 1.1 Vol. % and occurred on 2015-07-02 on SH F05 (Figure 4.3) under winter wheat. This summer day was hot and dry, reaching temperatures above 30° C. The DWD Meteo-Station in Aachen-Orsbach, within the Rur catchment, recorded a mean temperature of 27.8°C and a maximum temperature of 34.8°C. Up to six days in advance no precipitation occurred. Therefore, the soils were dry. In general on that day soil moisture was < 5 Vol. % for SH F05 and SH F04 and under 11 Vol. % on all fields in Selhausen. In Hürtgenwald soil moisture values between 9 and 23 Vol. % have been measured.

The highest mean soil moisture has been recorded on 2015-11-23 on HW F03 under grassland with 63.3 Vol. %. Temperatures on that day were low (1.3 ° C in mean with a minimum temperature of -2 ° C in Aachen-Orsbach) and up to seven days in advance high amounts of precipitation were recorded (e.g. 15.4 mm on 2015-11-19), whereas no precipitation occurred on 2015-11-23 itself. On that day all fields in Hürtgenwald showed soil moisture values > 25 Vol.

%, whereas in Selhausen soil moisture between 13 and 35 Vol. % has been measured.

In the whole data set, soil moisture values > 45 Vol. % only occurred under grassland. The range of soil moisture in Selhausen spans from 1.1 – 43.1 Vol. % and the range in Hürtgenwald is 5.9 – 63.3 Vol. %. Table 4.4 shows a summary of the mean field measurements of soil moisture. It indicates that in mean, soil moisture is lowest on SH F04. This field is characterized by a high stone content and lower harvest yields compared to the other Selhausen fields. In 2015, spelt was cultivated on SH F04 and in 2016 sugar beet. Highest soil moisture is found on HW F03 and HW F04, which both are grassland fields. Here standard deviation is high as well. Despite being cultivated with the same vegetation types in 2015 and 2016, fields HW F01-F03 show lower mean soil moisture and higher standard deviation in 2016 compared to 2015. Apart from that, no trend in mean soil moisture from 2015 to 2016 can be observed.

Table 4.4. Overview of field measurements of soil moisture for single fields and years giving the field mean and standard deviation based on the mean soil moisture (from the six single measurements) of each measurement point. A missing value indicated that no measurement was performed on that field in this year.

| Field | Mean | | Standard Deviation | |
|--------|------|------|--------------------|------|
| | 2015 | 2016 | 2015 | 2016 |
| SH F01 | 21.0 | 21.9 | 7.9 | 9.9 |
| SH F02 | 19.4 | - | 7.5 | - |
| SH F03 | 19.0 | 16.0 | 8.9 | 7.0 |
| SH F04 | 13.8 | 12.5 | 6.9 | 8.1 |
| SH F05 | 14.7 | 16.8 | 7.7 | 8.7 |
| SH F06 | - | 20.4 | - | 9.4 |
| HW F01 | 25.6 | 17.3 | 7.4 | 8.3 |
| HW F02 | 36.8 | 32.0 | 12.2 | 15.5 |
| HW F03 | 40.0 | 35.1 | 13.2 | 16.5 |
| HW F04 | 25.7 | - | 7.7 | - |
| HW F05 | - | 20.1 | - | 11.5 |

4.5.2 Vegetation Measurements

At three of the soil moisture measurement locations on each field, we performed additional destructive vegetation measurements, consisting of the measurement of plant height, row distance, the number of plants per area and the collection of samples. These samples were handled further in the laboratory to determine fresh and dry weight (for cereals, maize and sugar beet also organ specific), vegetation water content (VWC) and green and brown LAI. The green

and brown LAI was estimated in the laboratory using a conventional Epson DIN-A0 flat bed scanner and the image processing software Image J (<http://imagej.net>). Vegetation data was checked for outliers and quality. Only data with the highest quality standard was kept in the analysis. Table 4.5 gives an overview of the vegetation data from the field measurements by showing the maximum measured value for each vegetation type and vegetation parameter in mean per field and year. This depends of course on the phase of the phenological cycle of the different plants in which the ground measurement took place. This can explain for example, why winter barley LAI and biomass is much higher than that for winter wheat. Table 4.5 shows that sugar beet has the overall highest fresh and dry weight (= fresh and dry biomass) and the highest volumetric water content. Most of the biomass and water is stored below ground in the root, however. Maize plants grow highest with up to 2.4 m in mean. For maize, no brown LAI was measured on the field because the mature plants were harvested before the next possible measurement campaign. For grassland and triticale no LAI was estimated.

Table 4.5. Maximum of measured vegetation parameters averaged per field and year for the different vegetation types.

| Vegetation | Green LAI | Brown LAI | Fresh Weight [g/m ²] | Dry Weight [g/m ²] | VWC [Vol. %] | Canopy Height [cm] |
|---------------|-----------|-----------|----------------------------------|--------------------------------|--------------|--------------------|
| Winter Wheat | 3.1 | 0.8 | 4819 | 1624 | 82 | 82 |
| Winter Barley | 6.3 | 1.8 | 7584 | 2124 | 86 | 100 |
| Sugar Beet | 5.6 | 1.2 | 14580 | 2403 | 97 | 50 |
| Maize | 4.8 | - | 6840 | 1119 | 93 | 240 |
| Grassland | - | - | 1644 | 374 | 85 | 30 |
| Triticale | - | - | 3483 | 589 | 87 | 59 |

4.5.3 Roughness Measurements

Soil roughness measurements were performed on bare soil fields, cereal, sugar beet and maize fields in Selhausen and Hürtgenwald at the vegetation measurement locations. For the measurements, a custom laser scanner has been used (Figure 4.5). This scanner consists of a laser distance measurement device mounted on a platform moving with a known velocity. It measures with a spatial resolution of 1.1-1.2 mm in horizontal direction and 0.1-0.5 mm in vertical direction over 1 m. As the laser scanner was not ready for the 2015 measurement campaigns, measurements have been performed only in 2016. Due to the high workload, roughness measurements have not been performed on the days of vegetation and soil moisture measurements but with a delay of up to 14 days. Therefore, only measurements without tillage operations between SAR acquisition and roughness measurement can be used in the analysis.

For each of the three vegetation measurement points on the fields, three roughness measurements have been performed. For the three measurements, the measurement device was arranged in the directions 0° , 45° and 90° to the row direction on bare soil. This orientation is of importance, as the looking direction of the SAR sensor will influence the way it perceives the roughness on the ground. The flight direction of S1A in ascending orbit is from NNW (about 350°) to SSE (about 170°). With a right-looking mode, the sensor looks approximately in the direction of 260° . This direction is in line with the direction of the crop and sugar beet rows in Selhausen and is perpendicular to the row direction of the maize plants in Hürtgenwald. All other vegetation types in Hürtgenwald were not sown in rows. Therefore, for bare soil data from Selhausen the roughness measurements in 0° direction can be used, whereas for the maize fields in Hürtgenwald the 90° direction will be chosen. For the vegetated fields, only measurements in row direction can be performed as it is not possible to install the measurement device across the rows. Still, measurements on vegetated fields are not trivial, as leaves in the path of the laser scanner must be avoided. For that, two wooden boards were used, to keep the leaves out of the field of view of the laser scanner.



Figure 4.5. Custom laser scanner for roughness measurements. The laser distance measurement device is mounted to a moving platform. (Image: Esch, S., 2016)

The roughness data have been filtered for outliers, that have been caused e.g. by leaves hanging in the line-of-sight of the scanner or by crop residues. For that, a two-step approach has been used. It deletes 1) all data points with a deviation of more than 10 cm from the median of all measurements values in a row and uses 2) an overlapping moving window encompassing 20 measurements point that applies a median absolute deviation (MAD) filter:

$$MAD = b M_i(|x_i - M_j(x_j)|), \quad (4.1)$$

with x_i as single observations, $M_j(x_j)$ the median of the measurement series, M_i the median of deviations from the single measurements to the median of the measurement series and with value $b = 1.4826$, an empirical constant (Huber, 2011, Leys et al., 2013).

4.6 Soil Moisture Index Approach

The following section describes the methodology to develop and evaluate the soil moisture index approach that shall enable the retrieval of qualitative soil moisture information from historic ERS-SAR data.

The method to derive the soil moisture index is based on two main assumptions: i) the extreme states of soil moisture limit the range of surface soil moisture: saturation as the upper limit (wet) and the minimum water content of a given soil as the lower limit (dry) and ii) for a given land use type, variations of backscatter due to vegetation properties and surface roughness are much smaller than the variations of backscatter due to soil moisture. The upper and lower limits of soil moisture are soil texture specific properties. The soil moisture index is a relative value between these two extremes. Against the backdrop of the climate conditions prevailing in our test area and the large number of ERS-1 / -2 observation it can be assumed that within this data collective, both states, the dry and the saturated one, are represented.

However, as the backscatter signal depends not only on the surface soil moisture content but is also influenced by the vegetation properties (backscatter induced by vegetation geometry and plant water content, see chapter 2.5) and soil surface roughness (see chapter 2.4) (Ulaby et al., 1996), estimating the soil moisture state from the backscattering coefficient requires the reduction or even elimination of these influencing factors. In agricultural areas, both, vegetation properties and surface roughness can be described as a function of land use type (crop type, grassland, and bare soil) and time of year (phenological state and management activities). Assuming homogeneity of the backscatter impact of vegetation and surface roughness within a given land use class, variations of the backscatter for this class depend only upon differences of soil moisture. Thus, all backscatter data were grouped according to land use type and month. Grouping by months made sure, that the vegetation is at a comparable phenological state. These assumptions imply, that spatial heterogeneities in biomass within a given land use type are small compared to spatial heterogeneities in soil moisture. Based on our biomass measurements in the field, this assumption should be reasonably valid for an intensively used agricultural area such as our test area.

4.6.1 Developing the Soil Moisture Index Scheme

The available land use maps for each year distinguish sugar beet, cereals, and grassland pixels. All other areas are masked out, since soil moisture retrieval with C-Band is only possible for bare soil and agricultural land use types. The land use maps for each year are resampled to 20 m resolution using a majority method and then georeferenced to a corresponding SAR scene. This was done for the ascending and descending nodes respectively. To avoid mixed pixel effects, border pixels between two different land use types are masked using a dedicated filter that masks out pixels that are surrounded by more than 60% of pixels with a different land use type. Resampling and geo-referencing were performed using ArcGIS (ESRI, Redlands, USA). For each land use group (cereals, sugar beet, and grassland) and month, histograms of the sigma nought values in dB were produced. The soil moisture index was then scaled to the 5th and 95th percentiles of each histogram. Pixels outside of this range were discarded. Limiting the histogram analysis to these percentiles reduces spurious effects due to speckle or outliers. The interval between the two percentiles is then used to normalize the sigma nought values based on their position in the histogram. The soil moisture index value (SMI) is calculated similar to (Wagner et al., 1999b) as:

$$SMI = \frac{\sigma_0 - \sigma_{0dry}}{\sigma_{0wet} - \sigma_{0dry}} \cdot 100 \quad (4.2)$$

With σ_{0dry} being the 5th percentile and thus representing the dry state and σ_{0wet} being the 95th percentile, representing the wet state. A simple linear indexing is used because the relationship between surface soil moisture and radar signals is well described by linear relationships (Ulaby et al., 1986). The SMI can range between 0 and 100.

4.6.2 Evaluating the Soil Moisture Index Maps

Typically, ground measurements taken during the satellite overflight are used to validate remotely sensed surface soil moisture data. However, for historic data these measurements are usually not available. Therefore, because no ground-truth measurements of soil moisture that would allow for a traditional validation are available, we use the following two-step approach to validate the SMI: i) by comparing soil moisture index maps of two consecutive days and investigating the drying and wetting behaviour using precipitation measurements and ii) correlating the qualitative soil moisture index maps with antecedent precipitation at DWD stations.

One option for validation is to use the ERS-Tandem acquisitions. From 1995-08-17 until 1996-06-02, ERS-1 and -2 operated in the so-called tandem phase. During this phase but also beyond,

several acquisitions were made from the same path with 24 hours delay between the two satellite overpasses. Those tandem scenes can be used to observe short-term changes in soil moisture, like drying or wetting of the soil surface. Other parameters that may influence the backscatter intensity (surface roughness, vegetation cover) can be assumed constant on such a short time scale. Seven of those tandem scenes are available for our area and observation period. By calculating the differential SMI (ΔSMI) from two consecutive days and comparing it to precipitation data, we can evaluate if our resulting maps capture the changes in soil moisture. Therefore, the index value of the earlier tandem date is subtracted from the index value of the later tandem date. As the SMI comprises the values between 0 and 100, ΔSMI can take integer values between -100 (drying) and 100 (wetting).

The second method used to validate the soil moisture index approach is to use antecedent precipitation data as a comparable quantity. Antecedent precipitation is used as an approximation to soil moisture when soil moisture data is unavailable (Pan et al., 2003, Ali et al., 2010). As antecedent precipitation is based on measurements at meteorological stations, its spatial resolution is rather coarse. Substituting antecedent precipitation with the SMI would result in an improved spatial representation. However, this requires that a strong relationship between the soil moisture index and antecedent precipitation is found.

For this analysis, ten DWD RR stations (Figure 4.4) which provide a complete time series of measurements and are located within our test area were chosen. The mean SMI value for a region encompassing a one-kilometre radius around the DWD RR stations was calculated. It was then compared to the antecedent precipitation from the DWD RR stations.

A refined form of antecedent precipitation that shall account for the effects of subsurface flow and evapotranspiration loss is an Antecedent Precipitation Index (API). There are many algorithms to calculate the API with different levels of complexity. Several studies used an antecedent precipitation index (API) as an indicator of soil moisture in remote sensing approaches, especially in comparison with passive microwave remote sensing data (e.g. (Teng et al., 1993, Choudhury and Golus, 1987, Choudhury et al., 1986). A study of L-band SAR derived soil moisture (Mattia et al., 2009) in northern Germany used a simple version of the API as a-priori soil moisture information. They define the API_i for day i as:

$$API = \gamma_i \cdot API_{i-1} + P_i, \quad (4.3)$$

where P_i is the observed precipitation [mm] of day i and γ_i is the API recession coefficient which is used to parameterize the loss of water in the soil column due to evapotranspiration,

groundwater recharge and lateral soil water fluxes. For γ_i the parameterization proposed by (Crow and Zhan, 2007) is used, where γ_i is defined as:

$$\gamma_i = 0.85 + 0.1 \cdot \cos\left(\frac{2\pi \cdot JD}{365}\right), \quad (4.4)$$

which roughly estimates the seasonal effects of evapotranspiration loss, with JD = Julian Date. To keep our approach simple and without the need of additional data we follow this simple approach to calculate the API for the 10 DWD stations. We initialized the calculation on 1994-03-17, to have a one-year spin-up phase. The API is then compared to the mean soil moisture index that has been calculated for the different stations.

4.7 Geospatial Analysis of SMI Maps

One purpose of this thesis is to understand the spatial patterns of surface soil moisture in the Rur catchment. Spatial heterogeneity can be expressed by the two measures of spatial variability and spatial structure (for example the autocorrelation structure) (Garrigues et al., 2006, Reichenau et al., 2016).

Patterns of spatial variability can be examined by analysing the distribution of standard deviation throughout the Rur catchment. Therefore, standard deviation and mean SMI values have been calculated in 140 m x 140 m non-overlapping boxes.

The spatial structure can be assessed using semivariograms. The experimental semivariogram describes how data correlate at distinct distances (given by the lag). The shape of a semivariogram can be described by the three parameters range, sill and nugget. To find their values, theoretical semivariogram, must be fitted to the experimental semivariogram. It produces a continuous representation of the semivariogram which can be used to estimate the nugget from the intercept with the y-axis, the range from the distance of the first plateau of the semivariogram and the sill as the semivariance value of the first plateau of the theoretical semivariogram. The range parameter of the theoretical semivariogram can be used to describe the break between spatially correlated and uncorrelated values and hereby provides information about the spatial organization of soil moisture patterns (Korres et al., 2015). The sill parameter of the theoretical semivariogram describes the variance of uncorrelated values and the nugget parameter describes micro-scale variability and measurement error. Patterns in those parameters can reveal patterns in the distribution of surface soil moisture. Experimental semivariograms have been calculated using the R package *gstat* (Pebesma, 2004), utilizing a maximum lag of 25 km and a lag class size of 200 m. For fitting the theoretical semivariograms, the ordinary-least-squares method has been used, employing an exponential model.

4.8 Sentinel-1 Processing and Algorithm Development

This section describes the methods used in the second approach presented in this thesis: the development of a quantitative soil moisture and vegetation parameter retrieval scheme for dual-polarized S1A data. To be able to work with SAR data from S1A, the data must first be processed using an appropriate processing chain. Besides the intensity images, we are interested in the polarimetric information as given by the $H2\alpha$ decomposition. Therefore, we must work with complex data, which are given in products of SLC level. An overview of the single processing steps is given in Figure 4.6. As the final product shall encompass two intensity images and the polarimetric derivatives H , A , and α , we have to work with two different processing chains as we must apply different types of radiometric calibration.

After importing the images to SNAP, thermal noise removal is applied in the intensity processing chain to get intensity information with the highest possible radiometric accuracy. Thermal noise is caused by movements of the electrons in the circuits of the satellite and affects the SNR, especially when the backscatter level is low, as for cross-pol data and on very dark targets. Although an effect of thermal noise on polarimetric data has been found as well (Villano, 2014), thermal noise effects intensity data close to the noise-floor, like VH backscatter from smooth surfaces (e.g. water bodies) most. In addition, in SNAP 5.0 and PolSARpro 5.0 no thermal noise correction for polarimetric data was available. The next step in both processing chains is the application of the exact orbit information, before the data is calibrated. For the radiometric calibration to γ_0 , β_0 , σ_0 and the digital number (DN), four Look-Up Tables (LUT) are available that apply a range dependent gain including the absolute calibration constant.

While in the polarimetric processing chain, the data is calibrated to sigma nought with complex output to perform subsequent polarimetric decompositions, intensity data is calibrated to beta nought to perform state-of-the-art radiometric terrain flattening later. Radiometric terrain flattening is a better description of how the radar sees the ground than conventional radiometric calibration methods (like using the local incidence angle, LIA), as it can mimic the radar's image formation process, whereby each radar pulse is convolved with the landscape (Atwood et al., 2012). If uncorrected, terrain will not only influence the position of a given point on the earth surface but will also affect the brightness of the radar return as expressed in radar geometry. SAR sensors that provide state vectors and timing with higher absolute accuracy (as e.g. Sentinel-1) allow accurate geolocation and therefore advanced calibration methods like the radiometric terrain flattening (Small, 2011). H , A and α are independent of the intensity, so they are also independent of the radiometric variation induced by topography (Atwood, 2012). Therefore, no terrain flattening is applied in the polarimetric processing chain.

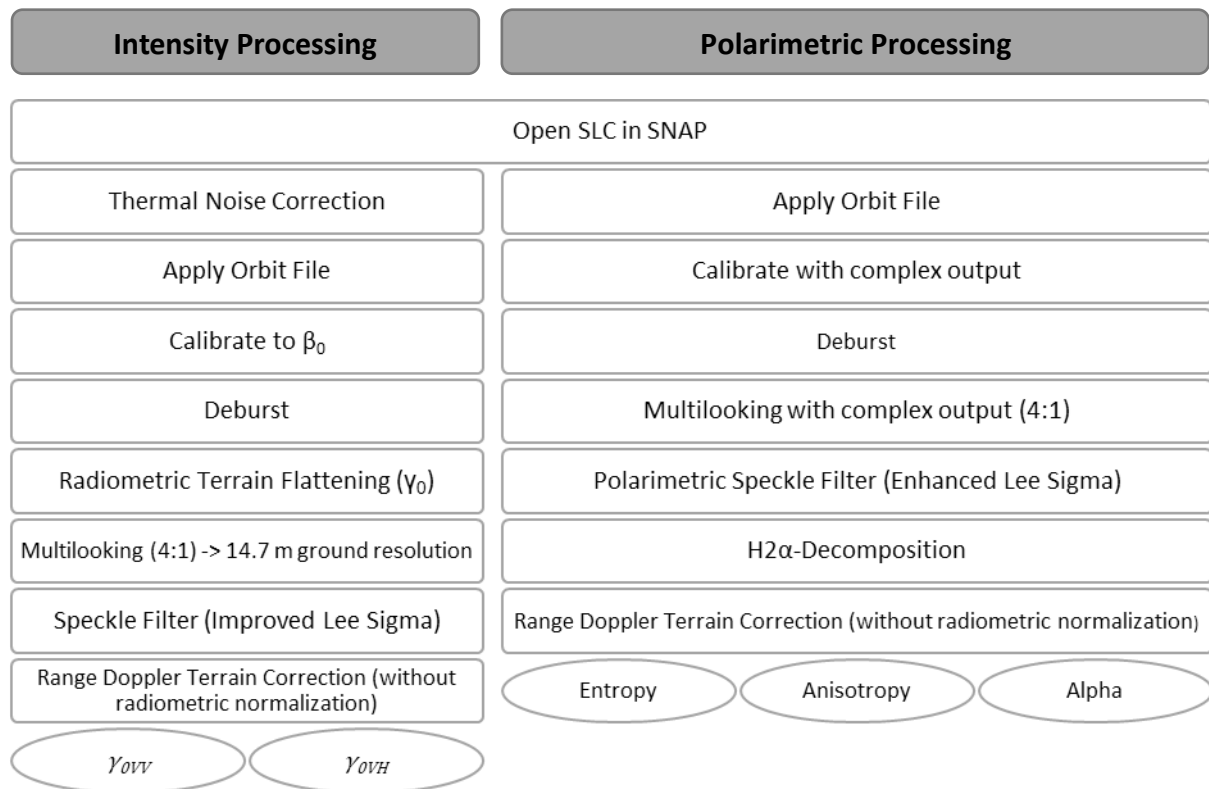


Figure 4.6. Processing chain for Sentinel-1 SLC data.

After radiometric calibration, both processing chains apply debursting, which is obligatory for Sentinel-1 images that are acquired in TOPSAR mode and therefore consist of single bursts that must be merged. After debursting (and after the radiometric terrain flattening for the intensity processing chain), the complex and the intensity data is multilooked with a factor 4:1 resulting in 14.7 m ground resolution. With multilooking, speckle reduction is induced for the intensity images, but no speckle reduction is reached for the complex data (as described in chapter 2.1.3).

The next step is the application of an Improved Lee Sigma Filter and an Enhanced Lee Sigma Filter (the polarimetric extension of the Improved Lee Sigma Filter) for speckle reduction, with standard settings as described in the reference literature (Lee et al., 2009, Lee et al., 2015). While the intensity data is directly projected to ground coordinates using Range Doppler Terrain Correction (that also corrects for the geometric distortions described in chapter 2.1.1), the complex data is decomposed first using the H2 α decomposition described in chapter 2.2. The final products of the processing chain are speckle reduced, ground projected, radiometrically and geometrically corrected images of γ_{ovv} , γ_{ovh} , H , A , α . γ_{ovv} and γ_{ovh} are then converted to dB. The Crosspol Ratio is calculated as the ratio γ_{ovh} to γ_{ovv} and is converted to dB as well.

4.8.1 S1A Radiometric Calibration Refinement

During the commissioning phase, a radiometric and polarimetric channel imbalance regarding the gain of S1A was found. After a calibration campaign on DLR sites in spring/summer 2015 this imbalance could be characterized and corrected for, leading to improved radiometric stability (ESA, 2015), as shown in Table 4.6.

Table 4.6. Radiometric calibration refinement for Sentinel-1A

| Radiometric Stability 2015 IW mode | Radiometric Stability 2015 IW mode after refinement |
|------------------------------------|---|
| 0.67 dB +/- 0.45 dB | 0.00 dB +/- 0.34 dB |

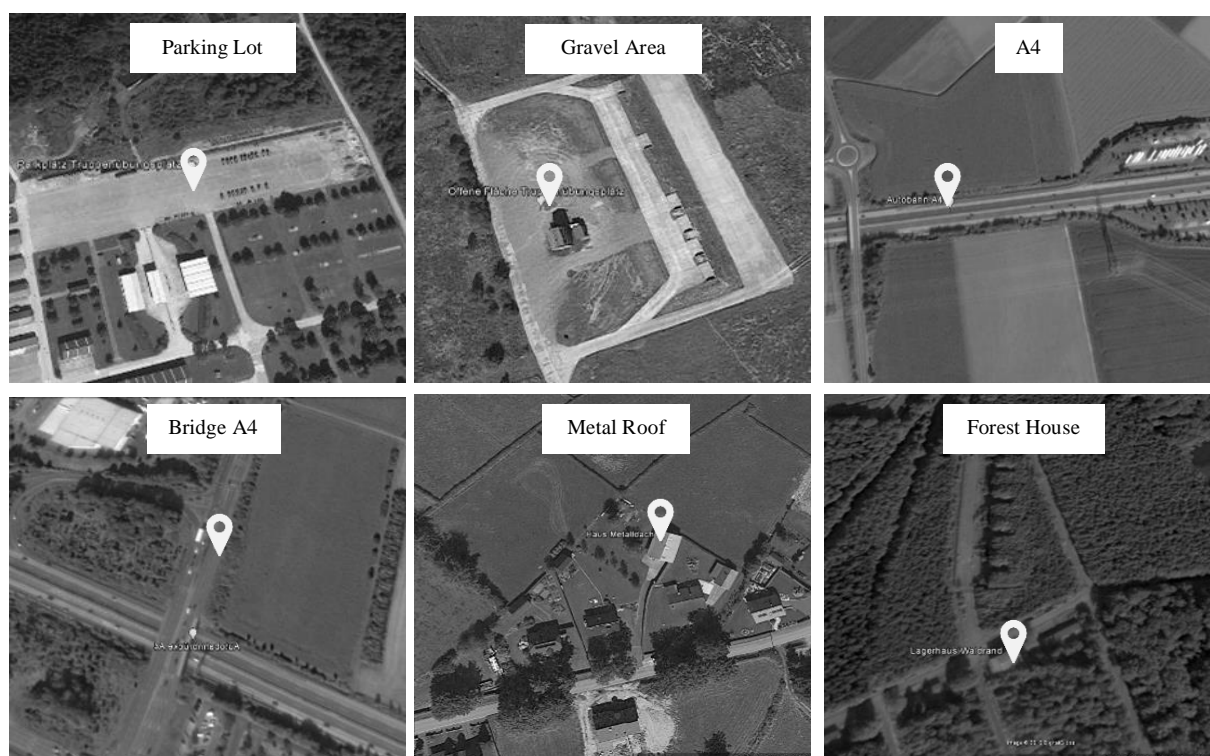


Figure 4.7. Stable targets for radiometric accuracy study.⁵

This calibration refinement is applied to all S1A acquisitions with a sensing time after 2015-11-26 and could therefore have effects on time-series data using both acquisitions before and after this date. The effect of this refinement has been studied by (El Hajj et al., 2016) using three different stable targets: a race track, a forest in France and an evergreen tropical forest in Gabon. They found, that on average, sigma nought from the period between the end of the commissioning phase in March 2015 and 2015-11-25 was about 0.9 dB higher than sigma nought in the period from 2015-11-26 – 2016-02-01. As we want to use data from 2015 and

⁵Source: 50°28'03.53" N 6°11'21.18" E. 2016-09-09., 50°28'30.99" N 6°12'24.67" E. 2016-09-09., 50°50'08.87" N 6°25'06.80" E. 2014-04-10., 50°50'20.15" N 6°27'12.16" E. 2014-04-10., 50°25'51.88" N 6°18'16.84" E. 2016-09-09., 50°46'20.55" N 6°24'27.39" E. 2014-04-10. **Google Earth**. 2017-11-09.

2016 in our study jointly, we must consider this effect. Therefore, we performed a study of the radiometric stability within our catchment as well, to check whether we find a notable effect. We chose six stable targets in our catchment as shown in Figure 4.7. They were identified either as very dark pixels (parking lot, gravel area and highway A4) or very bright pixels (metal roof, house at the edge of the forest and highway bridge A4). We compared the backscatter at these targets for our acquisitions before and after 2015-11-25 (Table 4.1).

Table 4.7. Mean and Standard Deviation (SD) of γ_0 in different polarizations for the different stable targets over all acquisitions in 2015 (before the calibration refinement) and 2016 (after the calibration refinement). Δ describes the change of the mean from 2015 to 2016.

| | γ_{0VV} [dB] | | | | γ_{0VH} [dB] | | | |
|---------------------|---------------------|-------|------|------|---------------------|-------|------|------|
| | Mean | | SD | | Mean | | SD | |
| | 2015 | 2016 | 2015 | 2016 | 2015 | 2016 | 2015 | 2016 |
| Parking Lot | -14.3 | -17.6 | 3.7 | 0.9 | -23.8 | -25.2 | 1.8 | 2.0 |
| | $\Delta = -3.3$ | | | | $\Delta = -1.39$ | | | |
| Gravel Area | -1.6 | 3.5 | 5.0 | 3.0 | -17.6 | -19.0 | 2.4 | 2.3 |
| | $\Delta = 5.1$ | | | | $\Delta = -1.4$ | | | |
| A4 | -14.2 | -14.9 | 1.0 | 1.6 | -20.3 | -20.7 | 1.2 | 1.5 |
| | $\Delta = -0.7$ | | | | $\Delta = -0.4$ | | | |
| Bridge A4 | -0.3 | 2.4 | 2.3 | 1.1 | -18.0 | -18.7 | 1.4 | 1.1 |
| | $\Delta = -2.1$ | | | | $\Delta = -0.7$ | | | |
| Metal Roof | 21.8 | 24.0 | 2.2 | 2.4 | 12.4 | 15.1 | 2.4 | 2.5 |
| | $\Delta = 2.2$ | | | | $\Delta = 2.7$ | | | |
| Forest House | 8.5 | 4.5 | 3.8 | 6.3 | -11.6 | -13.0 | 1.6 | 1.4 |
| | $\Delta = -4.0$ | | | | $\Delta = -1.4$ | | | |

Table 4.7 gives an overview of the mean backscatter over all acquisitions before and after the calibration refinement for the different stable targets and the different polarizations. It shows that for all targets, except for the gravel area in VV-polarization and the metal roof in VH-polarization, the standard deviation within one year is higher than the difference of the mean values from 2015 and 2016. This means that the change in mean intensity that we observe between acquisitions before and after the recalibration is small or of similar magnitude compared to the variability that naturally occurs within the two test years. We also found no trend in the mean values and standard deviations for the single years. Finally, a Levene- and a T-test proofed that for 2015 and 2016, the variance and the mean show no significant difference.

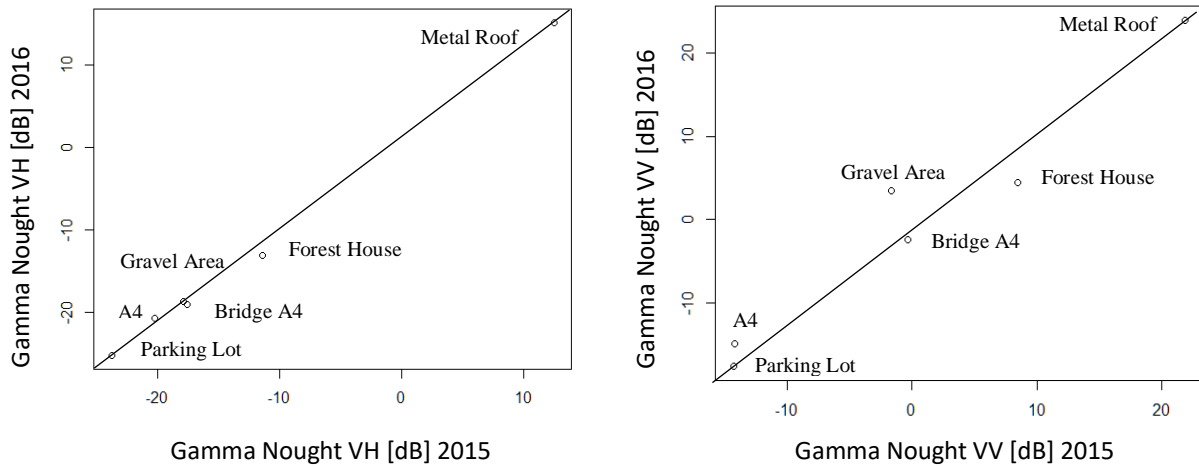


Figure 4.8. Comparison of γ_{0VV} (left) and γ_{0VH} (right) for 2015 and 2016. The solid line is the zero line.

The mean backscatter of 2015 plotted against the mean backscatter of 2016 for each stable target (Figure 4.8) shows, that in VH polarization all targets show a perfect linear relationship. In VV polarization, backscatter is higher in 2016 compared to 2015 for the gravel area. The forest house caused lower backscatter in 2016 compared to 2015. Nevertheless, we must keep in mind that our targets are not perfectly stable. Especially the gravel area and the forest house show high standard deviations.

To sum up, for our purpose of deriving soil moisture and vegetation information, the changes in radiometric stability before and after the radiometric calibration refinement are within the range of natural backscatter variations from one acquisition to the other. Slight deviations can only be identified for VV backscatter that is more sensitive to surface scattering than VH backscatter. As this occurred only on targets that are not perfectly stable, we do not need to split or calibrate our 2015 and 2016 datasets.

4.8.1 Algorithm Development for the Retrieval of Soil Moisture, Plant Parameters, and Surface Roughness

Before being able to develop retrieval schemes for land surface parameters we must analyse their relationship with S1A observables. Therefore, for every ground measurement, the respective SAR observable must be extracted from the SAR images first (Figure 4.9). Due to spatial uncertainties of the GPS system and of our GPS device that was used to determine the location of the ground measurements, we did not extract pixel sharp values but extracted the median pixel value within a buffer of 30 m around the GPS coordinate. This procedure additionally helps to minimize leftover speckle effects and is helpful when a measurement point is exactly on the edge of two neighbouring pixels.



Figure 4.9. Excerpt from S1A γ_{0vv} image from 2015-04-21 showing the Selhausen test sites with the measurement scheme and buffer (not drawn to scale). The bright area in the northern part of the image is a transformer station with electricity pylons in the eastern part of the image. In the south-western part of the image we can recognise train tracks and a settlement as bright area.

After extraction, the sensitivity of SAR signals to different in-situ measurements was assessed.

The in-situ measured parameters that we examined are:

- mean soil moisture (SM_mean), which is the mean of the six single measurements per measurement point,
- total fresh biomass (Biomass_total), the sum of fresh biomass per square meter,
- total dry biomass (Biomass_dry_total), the sum of dry biomass per square meter,
- biomass density (Biomass_density), which is Biomass_total divided by the canopy height,
- vegetation water content (VWC), which is the difference between Biomass_total and Biomass_dry_total,
- green LAI (Green_LAI),
- brown LAI (Brown_LAI) and
- canopy height (Canopy_height).

We also tested median soil moisture and the standard deviation of soil moisture from the six single measurements to substitute mean soil moisture, but found that the SAR signals were more sensitive to the mean soil moisture and resulted in higher correlations.

First, we performed a linear correlation analysis of the SAR observables and the in-situ parameters and visualized the results using correlation heat maps. These heat maps show the linear

Pearson correlation coefficient between the different SAR and in-situ parameters. Next, we performed a signal analysis, in which we examined the temporal course of different SAR measures using boxplots. The boxplots show the median value, the 25th and 75th percentile and whiskers that represent 1.5 times the interquartile range (IQR). The boxplots are distinguished by land use class and are compared to barplots that show field mean values of soil moisture. Vegetation parameters (canopy height, green LAI, brown LAI, wet biomass, dry biomass and VWC) were consulted to find possible influences on the course of the SAR observables or regarding differences between fields.

The results of both analyses of sensitivity of SAR observables to in-situ parameters were then used to optimize the development of empirical models which can explain the relationship between SAR measurements and soil moisture, or plant parameters. Regression analysis is then performed for the different land use types. We tested linear and non-linear, uni- and multivariate regressions to find the optimal model and calculated the adjusted R^2 . The strongest relationships were selected and validated using leave-one-out cross-validation (LOOCV) and ten- and five-fold bootstrapping. LOOCV performs $n-1$ runs and leaves out one observation in each run. The model is calculated on the $n-1$ observations and is then used to estimate the left-out observation. The result is a mean RMSE between the prediction and the real value of the left-out observation for all runs. The principle of the k -fold (here $k = 10; 5$) bootstrapping is similar. Instead of leaving out only one observation, the data set is split in k subsamples of similar size. In $k-1$ runs, a different subsample is left out and predicted, respectively. As the composition of the subsamples is random, we repeated the whole process 1000 times and calculated the mean RMSE of these 1000 repetitions.

5 Results & Discussion: Soil Moisture and Vegetation Parameters from C-band SAR

This section gives an overview of the two retrieval methods and the resulting products. Whereas both methods produce surface soil moisture products from C-band SAR, the first approach will produce the qualitative SMI product whereas the second approach results in high spatially resolved quantitative soil moisture and/or vegetation parameters depending on the land use type.

5.1 The Qualitative ERS Soil Moisture Index

The first step in interpreting the soil moisture index results is to evaluate its performance. In the following paragraphs the temporal course of backscatter for different land use types is assessed. Later, backscatter is compared to precipitation information in terms of wetting and drying events and antecedent precipitation.

In order to account for the effects of land use type, surface roughness and growing vegetation on the backscatter, we keep their influence at a comparable magnitude by grouping the pixels by land use type and month (approximating phenological state). Herewith we are able to calculate a comparable index for each group. We opted for a monthly subdivision to represent vegetation dynamics. While on the one hand a weekly or biweekly subdivision might better represent the vegetation dynamics during phases of high vegetation growth rates, it would drastically reduce the sample size per group on the other hand. A large enough sample size is mandatory to ensure that wet and dry pixels are contained in the sample. By using the monthly subdivision, a clear dependence of sigma nought on the vegetation state can be seen for cereals and sugarbeet (Figure 5.1). This is expected as both crops have a unique growing cycle. Therefore, a monthly subdivision is appropriate.

Corresponding to increasing biomass, the backscatter intensity of cereals decreases from April to June. This can be explained by higher attenuation rates. In July, where cereals are dry, the biomass is highest in the fruit and no longer in the leaves and cereals are usually harvested, the backscatter intensity increases again. After harvest, in August, September and October, the backscatter intensity stays relatively constant on a high level. The range of the whiskers, representing extreme data points, is small compared to the other months.

The seasonality of sugar beet is less prominent than for cereals. Sugar beet generally accumulates biomass between the end of June and October, when it is harvested. In contrast to cereals, most biomass is located below ground. The sugar beet root also stores high amounts of water. This could have an amplifying instead of attenuating effect on the backscatter intensity, which explains the higher backscatter intensity during the growth period in July to October. For both

cereal and sugar beet backscatter, intensity is highest in March. This could be due to frozen soils or ploughing activities. Indeed, March is the coldest month within the vegetation period, so that frozen soil could occur. For our observation years, the DWD climate station in Aachen recorded a mean air temperature of 6.1° C. On 1996-03-27 in the early morning and late evening air temperatures below or close to zero were recorded in Aachen. Since the ERS acquisition on that date was at 21:40, frozen soils are possible. However, since frozen soils are reported to result in a decrease in backscatter intensity (Rignot et al., 1994, Smith et al., 2004, Wegmüller, 1990), we accredit the higher backscatter in March to ploughing activities. The ploughed soil could increase double bounce effects, due to high surface roughness and vertical surface structures.

No clear seasonal evolution is expected for grassland, as biomass development depends on cutting dates and not on a specific agricultural cycle. This is supported by the boxplot that shows no clear seasonality but long whiskers. As no information about cutting dates is available and to apply a consistent method to all land use types, a monthly subdivision is used for grassland as well.

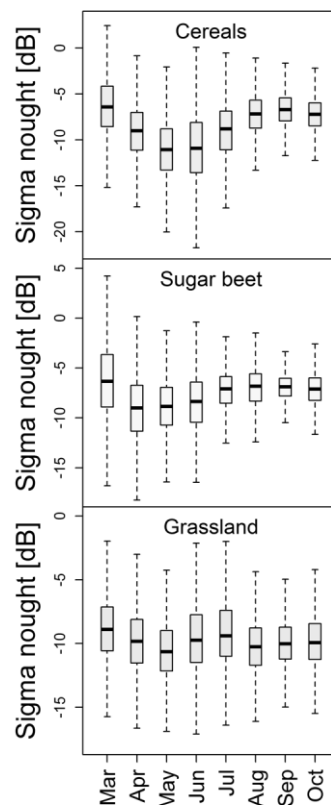


Figure 5.1. Monthly boxplots of backscattering coefficient sigma nought [dB] for different land use types during the vegetation periods of 1995-1997 and 1999-2003. The whiskers show the most extreme data point that is no more than 1.5 times the interquartile range.

By applying equation (4.2) to the 84 sigma nought maps, we produced maps showing the normalized SMI values. The map for the 25th of July 2000 (Figure 5.2) shows wetter soil conditions in mean compared to the map of 3rd of September 2002. When comparing to the daily average precipitation, from the 10 DWD RR-stations within the Rur catchment, this is reasonable, as there was only slight precipitation on 3rd of September 2002 (0.7 mm), with no rainfall the day before. Whereas there was higher rainfall on 25th of July 2000 (6.1 mm) with high rainfalls the day before (30.9 mm). This is a first indication that the soil moisture index can express changes in soil moisture. To analyse this more thoroughly, Δ SMI from the tandem acquisitions is compared to precipitation data in the next chapter.

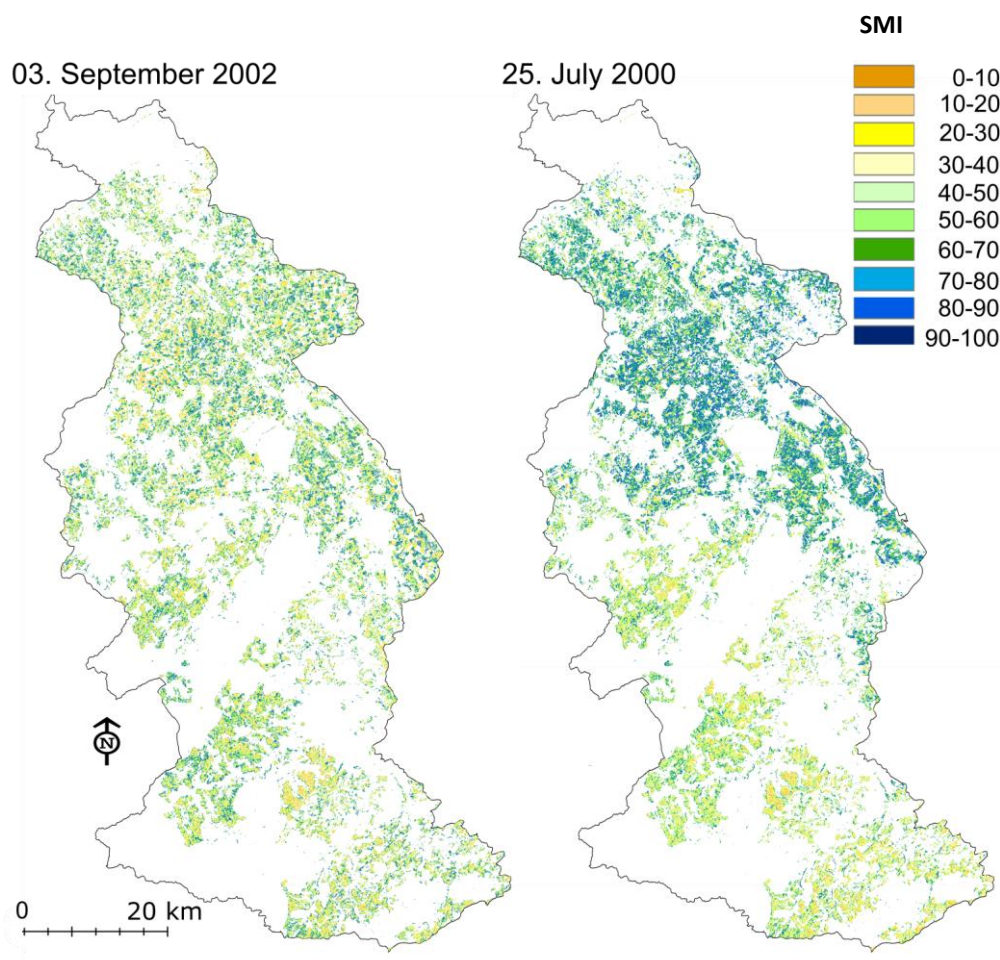


Figure 5.2. SMI maps based on single pixels from 03. September 2002 and 25. July 2000. SMI classes range from 0- very low, to 100- very high amount of soil moisture.

5.1.1 ERS-1 & 2 Tandem Scenes for the Evaluation of Drying and Wetting Processes

For the seven paired scenes of the tandem acquisition (Table 4.5), Δ SMI was calculated. On the map from 1996-03-26 and 1996-03-27 (Figure 5.3) we clearly see strong drying (red) whereas for 1996-04-30 and 1996-05-01 we see wetting (blue) of the area. This is well in line with the

measured daily precipitation at the 10 meteorological stations (Table 5.1). For the drying case, precipitation has been recorded at all stations on 1996-03-26. One day later, on 1996-03-27, only two stations show precipitation. This correlates with the “drying” indicated in the differential map. However, as frozen soils are possible on the acquisition of 1996-03-27, due to low air temperatures, the “drying” could have also been caused by that. For the wetting case, no precipitation has been recorded at the stations on 1996-04-30, whereas on 1996-05-01 all stations recorded precipitation. The Δ SMI captures this development well. Looking at all seven tandem pairs, statistical F-tests and Levene-tests between each tandem-pair showed inequality in variance for all cases. The subsequent Welch-tests showed significant differences in mean for each tandem pair. This indicates a clear change in the backscatter distribution from one to the next image in the tandem pairs. The mean Δ SMI and the number of pixels in each differential image, that display drying or wetting, were compared to precipitation at the different stations (Table 4.1). A positive Tandem mean Δ SMI shows that the mean of the differential image has a wetting tendency, a negative tandem mean Δ SMI shows a drying tendency.

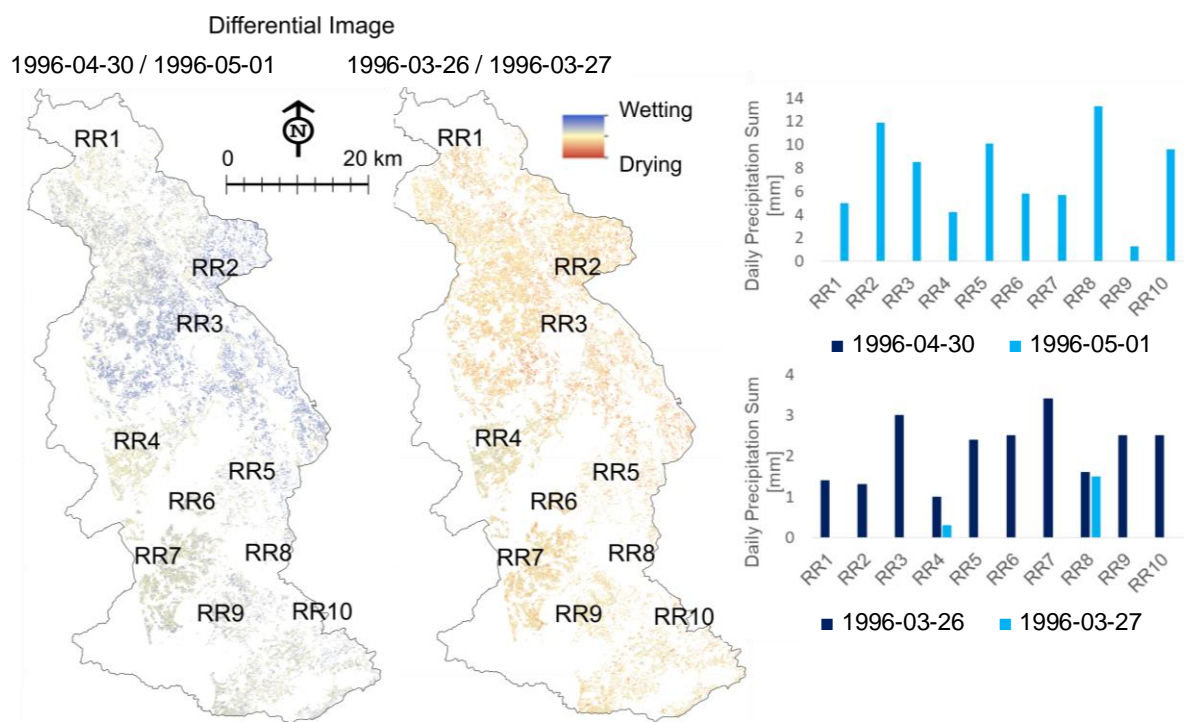


Figure 5.3. Maps of SMI differences (Δ SMI) from ERS tandem pairs with corresponding daily precipitation at the ten DWD stations introduced in Fig. 4.4.

The precipitation measured at the stations on dates of tandem acquisitions has been compared to the mean Δ SMI and the percentage of wetting and drying pixels (Table 5.1). The effect of precipitation is well represented by the change in the tandem images, which can be accredited to a change in soil moisture. Precipitation situations without a clear trend, like on 1995-10-

03/1995-10-04 and on 1997-05-20/1997-05-21, result in an almost equal percentage of pixels showing wetting and drying tendencies and the mean of the differential tandem image is close to zero. On dates with a clear difference of precipitation amount from one to the other date, there is also a clear tendency of wetting or drying and a mean value far from zero.

Table 5.1. Mean precipitation [mm] as measured at the ten different stations and standard deviation of precipitation [mm] for dates of tandem acquisitions with corresponding mean SMI difference (Δ SMI) and the percentage of wetting and drying pixels

| Date | Mean Precipitation [mm] | Standard Deviation [mm] | Tandem Mean | Percentage of Tendency | | |
|------------|-------------------------|-------------------------|-------------|------------------------|-----------|--------|
| | | | | drier | no change | wetter |
| 1995-10-03 | 3.3 | 2.1 | | | | |
| 1995-10-04 | 7.0 | 2.8 | 5 | 40 | 2 | 58 |
| 1996-03-26 | 2,2 | 0.8 | | | | |
| 1996-03-27 | 0.2 | 0.5 | -20 | 84 | 1 | 15 |
| 1996-04-11 | 3,5 | 1.4 | | | | |
| 1996-04-12 | 0,1 | 0.1 | -21 | 83 | 1 | 16 |
| 1996-04-30 | 0 | 0 | | | | |
| 1996-05-01 | 7.5 | 3.8 | 35 | 4 | 0 | 95 |
| 1996-06-20 | 5.8 | 1.4 | | | | |
| 1996-06-21 | 0.2 | 0.4 | -12 | 74 | 2 | 24 |
| 1996-10-22 | 0 | 0 | | | | |
| 1996-10-23 | 0 | 0 | -1 | 50 | 2 | 48 |
| 1997-05-20 | 6.3 | 2.1 | | | | |
| 1997-05-21 | 3 | 3.0 | 0 | 50 | 3 | 47 |

5.1.2 Comparing the Soil Moisture Index to Antecedent Precipitation

The previous chapter showed that the SMI can display soil moisture changes. In this chapter, we want to investigate whether the SMI behaves like an in-situ soil moisture data set. So, SMI mean values at each station and in-situ soil moisture data were compared to corresponding antecedent precipitation sums.

The general relationship between antecedent precipitation and surface soil moisture is influenced by different factors as meteorological conditions (e.g. wind, evapotranspiration), interception and saturation state of the soil that are not considered in our analysis. This means, different combinations of antecedent precipitation can cause different SMI values due to different

meteorological conditions but also due to the previous saturation state of the soil. So, from a theoretical point of view, a strong correlation between SMI and antecedent precipitation is not to be expected (Figure 5.4).

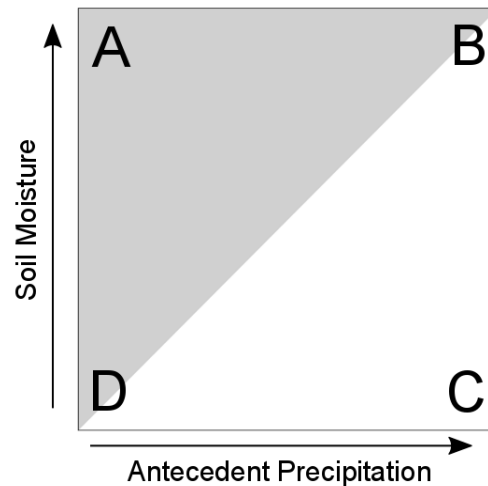


Figure 5.4. Theoretical relationship between soil moisture and antecedent precipitation. The grey triangle shows the theoretically plausible area of values.

Thus, the relation of antecedent precipitation to soil moisture has the shape of a triangle (Figure 5.4). Depending on the saturation state of the soil, low antecedent precipitation can result in low to high soil moisture. High antecedent precipitation can only result in high soil moisture unless there is sealing or crustification of the soil.

To check if in-situ measured soil moisture values fulfil our theoretical scheme, we compared daily measurements from seven soil moisture sensors at 5 cm depth with 7-day antecedent precipitation recorded at the same stations (Figure 5.5). The measurements are from periods in 2014 to 2016. Only measurements from the general vegetation period are used. The scatterplot fulfils the theoretical expectations and resembles Figure 5.4.

A comparison of soil moisture index and 7-day antecedent precipitation (Figure 5.6) at the 10 DWD stations also shows a behaviour consistent with theoretical considerations and resembles Figure 5.4. Low amounts of antecedent precipitation cause low to high SMI values but high amounts of antecedent precipitation do not cause low SMI values.

The fact that both SMI and in-situ measured soil moisture react to antecedent precipitation in a similar way, is an additional evidence that the SMI is representing soil moisture. As mentioned before, no clear relationship between antecedent precipitation and near surface soil moisture can be expected because of the many interacting factors that are involved (meteorological condition, saturation of the soil etc.). When reducing the influence of these interactions by averaging, we see a strong linear relationship between SMI and 7-day antecedent precipitation.

Therefore, we grouped the SMI into 100 and 10 classes, respectively. For each SMI class the antecedent precipitation was averaged. This approach shows by which antecedent precipitation height in average a specific SMI range is created (Figure 5.7).

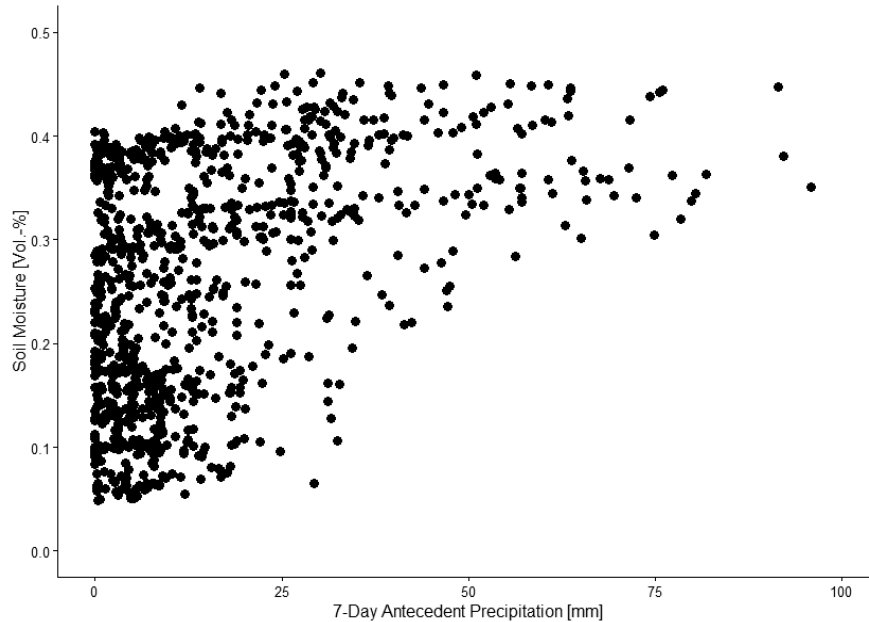


Figure 5.5. Comparison of 7-day sum of antecedent precipitation with daily mean soil moisture from 7 Meteo-Stations within the Rur-catchment. Continuous measurements were taken in 5 cm depth. Data are from vegetation periods in 2014-2016.

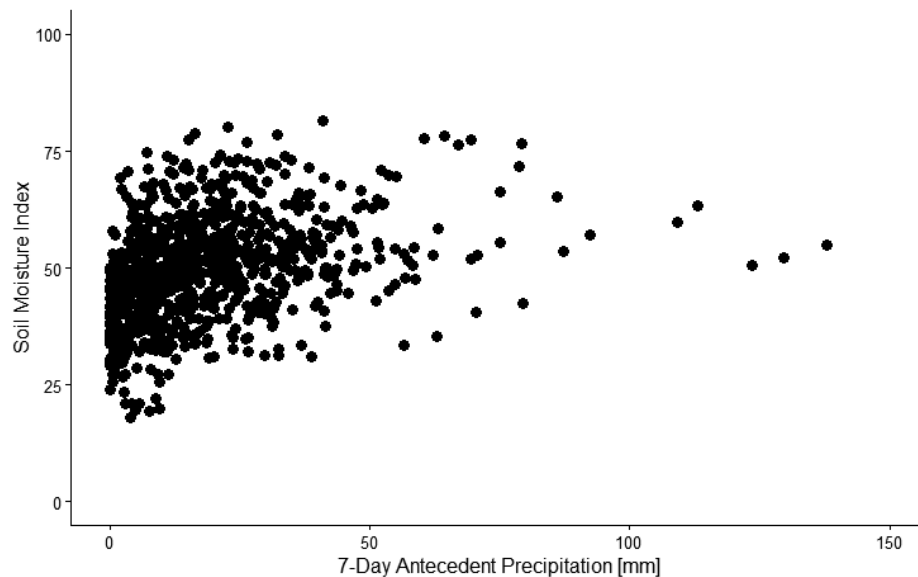


Figure 5.6. Comparison of 7-day sum of antecedent precipitation with mean SMI for all stations and ERS-scenes.

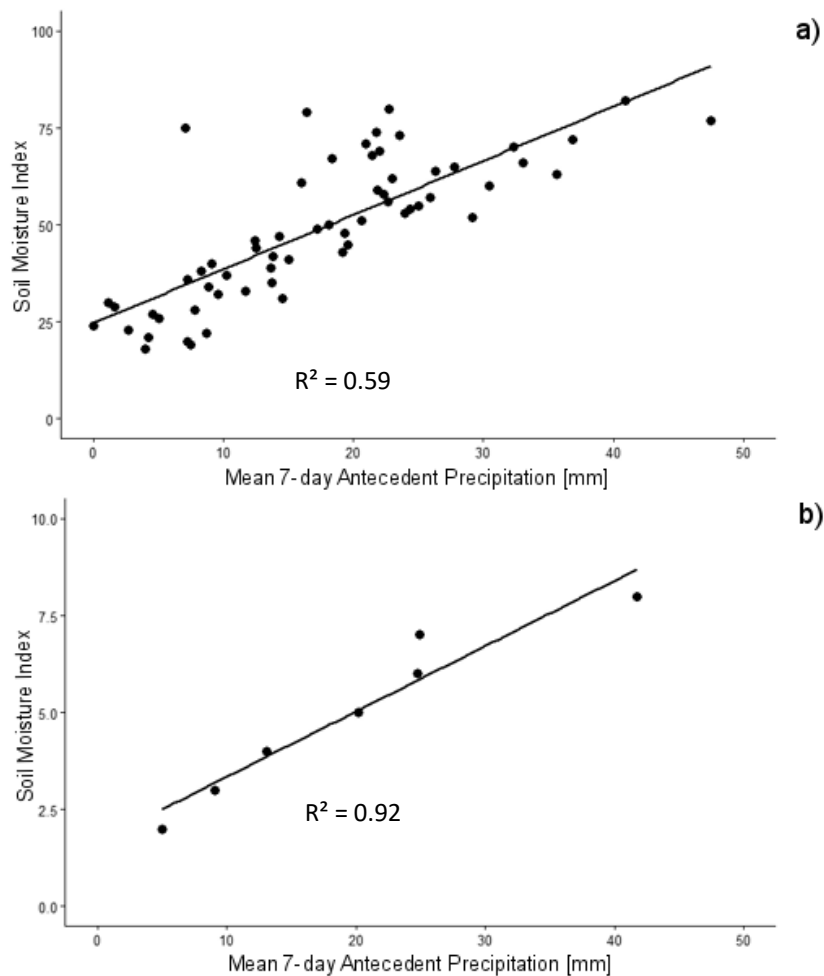


Figure 5.7. Comparison of 7-day sum of antecedent precipitation averaged by SMI class with mean SMI for all stations and ERS-scenes. With a) 100 classes ranging from 0-100 and b) 10 classes ranging from 0-10.

It can be seen immediately that when scatter, mainly induced by the interactions within the evolution of precipitation into soil moisture, is reduced, the linear correlation is highly significant and shows an R^2 of 0.59 for 100 classes and 0.92 for ten classes. It is in line with previous research, that ten classes of soil moisture are well distinguishable, as ERS based soil moisture estimates have been found to provide a RMSE of about 5-10 Vol% (Quesney et al., 2000, Rombach and Mauser, 1997), thus resulting in about 5-10 discernible soil moisture classes. Like also in Fig. 18, we must notice, that the lowest SMI values between 0 and 10 and the highest SMI values between 90 and 100 are almost not represented at all. This did not change significantly when we excluded additional extreme values by spanning the SMI between the 10th and 90th percentile instead of the standard interval between the 5th and 95th percentile (see 4.6.1). Very low and very high soil moisture is rarely found, especially when averaging over a larger area as we did within the one-kilometre buffer around the meteo stations. This does not

mean that our assumption of finding wet and dry pixels is wrong, but it means that when averaging over a larger area at few selected points in the Rur catchment, very dry and very wet situations are underrepresented.

No improvement has been seen when calculating the correlation between soil moisture index and antecedent precipitation restricted to the crop areas and restricted to grassland areas respectively. From that, we can conclude that there is no clear evidence that the soil moisture index works worse on one of the two land use types despite their different biomass development. We performed the same analysis using an Antecedent Precipitation Index (API) based on (Mattia et al., 2009) instead of antecedent precipitation and found comparable results:

The correlation between the soil moisture index and the API, calculated with (4.3) and (4.4), is low (Figure 5.8) and its form is comparable to the correlation between the soil moisture index and the 7-day antecedent precipitation (Figure 5.6). To test the relationship of in-situ measured soil moisture data and the API, we used five of the seven meteo stations described above. Two stations (Meteo 1 & Meteo 3) were discarded for calculating the API as they recorded data for no longer than one month during the vegetation period, which is not sufficient to initialize the API.

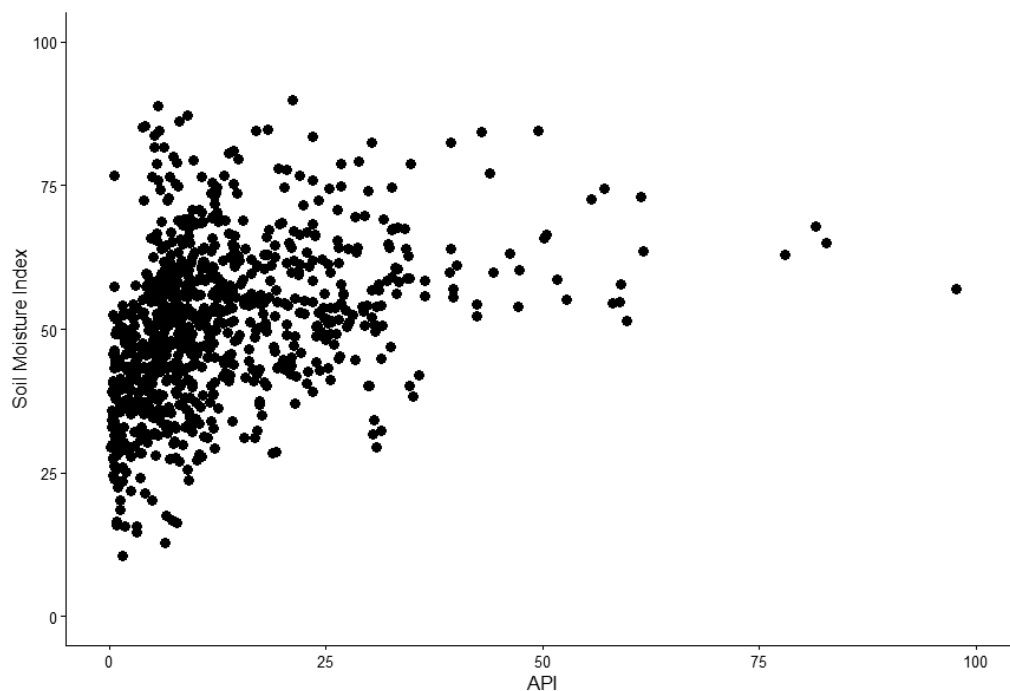


Figure 5.8. Comparison of Antecedent Precipitation Index (API) with corresponding SMI values.

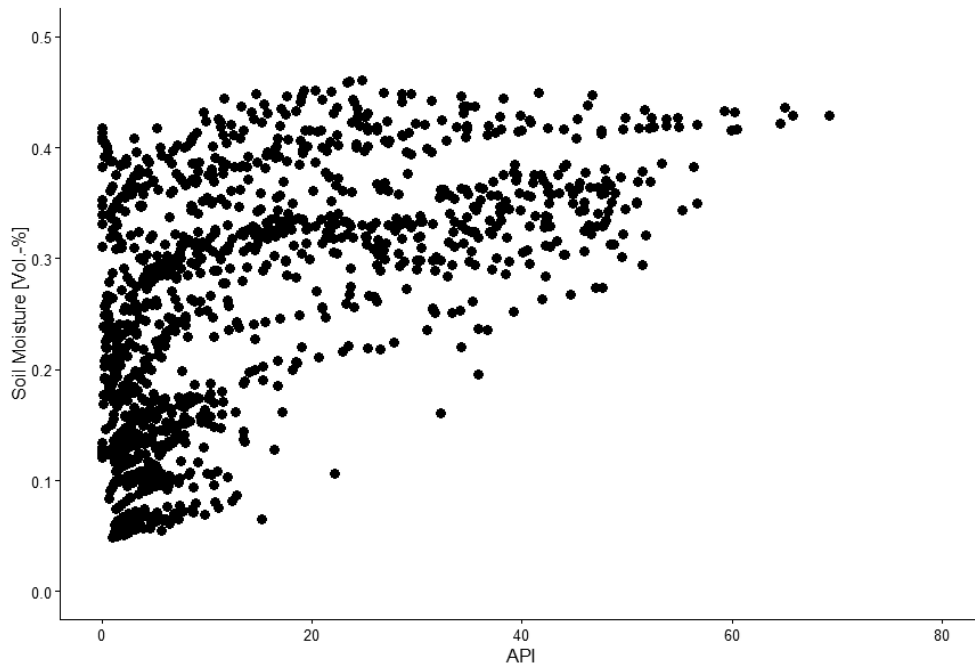


Figure 5.9. Comparison of Antecedent Precipitation Index (API) with daily mean soil moisture from 5 Meteo-Station within the Rur-catchment. Continuous measurements were taken in 5cm depth. Data are from vegetation periods in 2014-2016.

Again, a lot of scatter characterizes the relationship (Figure 5.9), like the relationships between soil moisture and the 7-day antecedent precipitation sum. This finding indicates that the API, at least in the simple form used here, is no good substitute for surface soil moisture applications and more comparable to an antecedent precipitation sum. It does not account correctly for the antecedent soil moisture and evapotranspiration and thus the evolution of precipitation into soil moisture. As the relationship between in-situ measured surface soil moisture and antecedent precipitation / API and the relationship between the SMI and antecedent precipitation / API show similar behaviour and fulfil theoretically expected distributions, the soil moisture index can be used as a proxy for in-situ measured near-surface soil moisture. To use an API as soil moisture information, a more sophisticated version of the API would be needed. In data scarce areas and for historic data sets the necessary input data is not available. In that context, our index approach is superior to the API because it needs no precipitation information.

5.1.3 Summary Qualitative ERS Soil Moisture Index

The two evaluations presented in the last chapters show that the qualitative Soil Moisture Index can display changes in the moisture state and behaves like in-situ soil moisture when compared to antecedent precipitation. It is very promising that by reducing the scatter by looking at the mean 7-day antecedent precipitation corresponding to each soil moisture index class, a very high positive correlation occurs. This means, that in general a higher antecedent precipitation

causes the assignment of a higher soil moisture index value if the influence of other interdependencies is reduced via averaging. Therefore, general patterns of SMI should be reliable although single pixel values are uncertain.

5.2 Analysis of Spatial Patterns of Soil Moisture in the Rur Catchment

Having a time series of SMI values at high spatial resolution gives the opportunity to examine the temporal or seasonal evolution of the spatial soil moisture structure and to find possible dependencies on soil moisture state. If we want to assess which factors regulate the spatial distribution of surface soil moisture in the Rur catchment, we must consider spatial heterogeneity of soil moisture first and then its structure.

It has been found that the theoretical relationship between standard deviation and mean soil moisture shows a unimodal shape, where standard deviation is highest at medium mean soil moisture values and is low in wet or dry areas (Vereecken et al., 2007, Bell et al., 1980). This shape has been explained in chapter 2.3.3.

To investigate whether similar behaviour can be found in the SMI data, mean SMI value and standard deviation have been calculated for the whole Rur catchment. We chose 140 x 140 m non-overlapping boxes for the calculations, as in this small area, antecedent precipitation heights, soil types and land use types are assumed to be homogenous. At intermediate mean SMI values, standard deviation shows a wide range of values up to a maximum standard deviation (Figure 5.10). In dry areas (with low SMI mean) and wet areas (with high SMI mean) the range of standard deviations is low and no high standard deviation values are found. Thus, the outline of the distribution follows the findings mentioned above and shows the theoretically expected behaviour of a soil moisture data set.

This behaviour is an important finding, as it contradicts the argument that the soil moisture index could possibly show pure effects of vegetation instead of soil moisture. If we would assume that what we observe with the soil moisture index is a plant signal and not a soil moisture signal, an increase in plant density would increase the plant heterogeneity and thus the variability in roughness or water content. This could lead to an increased backscatter variability (and hereby to an increased SMI variability). The relationship would probably saturate at a certain density but it would not decrease again. This indicates that the soil moisture index method, despite its crude way of minimizing the vegetation influence, represents soil moisture and not vegetation water content or interception.

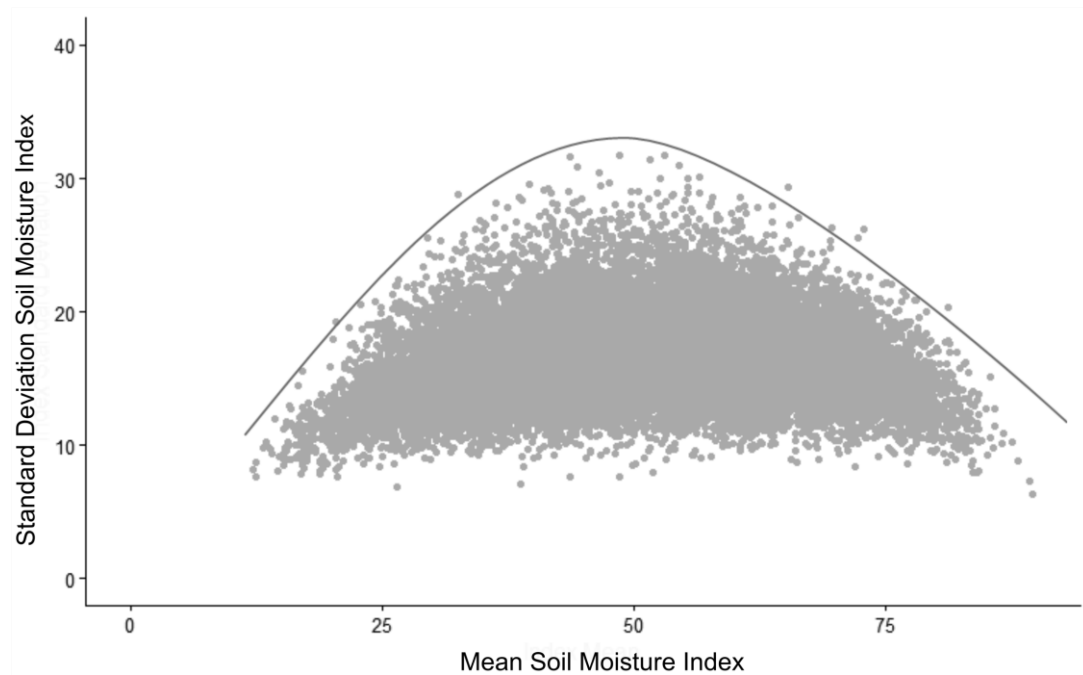


Figure 5.10. Comparison of SMI Standard Deviation and SMI Mean over the whole Rur-catchment and over all dates. The analysis has been performed in 140 m x 140 m non-overlapping boxes. The solid line shows the theoretical relationship between standard deviation and mean of soil moisture as described in Vereecken et al. (2007) and Bell et al. (1980).

Semivariogram analysis reveals spatial patterns in the data and enables to find causes of these patterns. In previous studies, a semivariogram analysis of surface soil moisture revealed temporal courses and dependencies on moisture state for range and sill values (Korres et al. 2015, Western et al., 1998). For the current study, experimental and theoretical semivariograms were generated for the three different spatial units: i) the whole catchment, ii) the low mountain range of the Eifel and iii) the fertile loess plain, respectively. Most semivariograms could not be fitted well by a conventional model, so that a nested approach had to be applied (Figure 5.11) where two semivariograms are added. This implies that there are at least two spatial patterns that have an influence on the SMI in the Rur catchment. Theoretical semivariograms were fitted for lags up to 10 km. In those cases, where simple and nested approaches failed to fit the experimental semivariogram, an exponential fit was used but restricted to a maximum lag of three km as only this resulted in acceptable fits. For the whole catchment, this was the case for four out of 84 dates, for the Eifel region the simple exponential fit had been applied to three dates but on four dates, no model could be fitted at all. For the fertile loess plain again all dates could be fitted, but for 16 out of 84 dates the simple exponential fit has been chosen. This means, that for these dates we find several underlying influences at distances of more than three km that cannot be

described. No commonality regarding season or soil moisture state could be found amongst these dates.

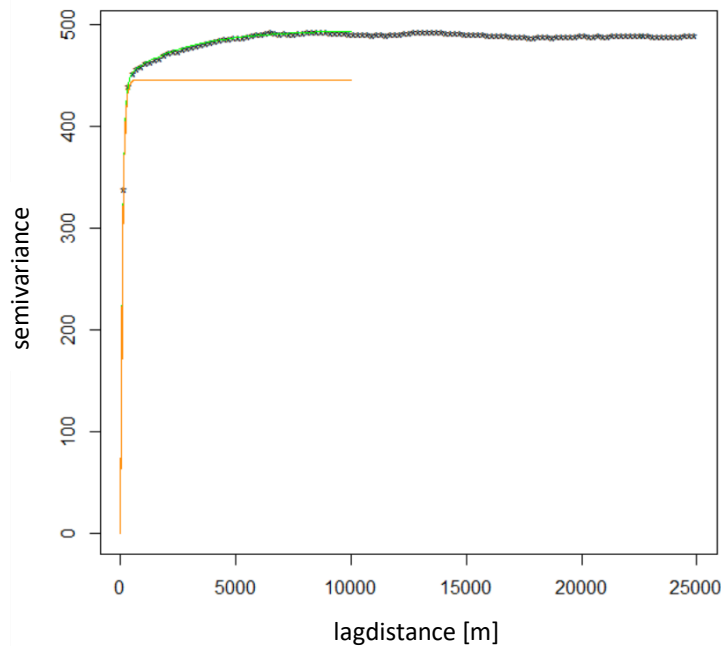


Figure 5.11. Exemplary empirical semivariogram with simple exponential (yellow) and nested exponential fit (green) showing 6th of June 1997. The maximum lag for fitting has been set to 10 km. Semivariance describes the variance in the spatial relationship and is inverse to autocorrelation.

The short ranges for the whole catchment span between 88 m and 202 m, for the fertile loess plain between 92 m and 224 m and those for the Eifel region between 82 m and 261 m. These scales correspond to typical field sizes found in the Rur catchment, so that we assume changes in agricultural management from one to the next field (e.g. crop type, phenological state, cutting dates on grassland) and thereby changes in evapotranspiration, are the dominating influence on the spatial structure of soil moisture on the smaller scale. Comparable ranges have been found by (Reichenau et al., 2016) when analysing the spatial structure of Leaf Area Index (LAI) on arable land in the fertile loess plain. To find factors that influence the spatial structure of soil moisture, we correlated the ranges determined in the semivariogram analysis with mean soil moisture and its standard deviation. We also searched for temporal patterns, e.g. distinctive features in specific years or months or specific temporal courses.

Short ranges are compared to standard deviation of soil moisture (which correlates with sill) in Figure 5.12. For the whole Rur catchment and for the fertile loess plain, a slight negative trend, though highly variable, can be observed. This negative trend is reasonable as we expect to find a faster decrease in autocorrelation with distance, the more variable soil moisture is. For the Eifel region alone, no significant trend is found in the data. The short range values for the Eifel

region are in general slightly higher but also more variable than in the other two areas. This is explained well by the fact that the Eifel is mainly characterized by grassland areas that usually have no clear field borders but span larger areas and are influenced by heterogeneous terrain. A comparison of short ranges with mean SMI neither shows a trend for the whole Rur catchment nor for the fertile loess plain or the Eifel region separately (Figure 5.13). Thus, in our data, the spatial structure of soil moisture is not correlated with the mean soil moisture state. This leads to the assumption, that soil moisture is too variable to be represented by a single value for the whole catchment (or fertile loess plain or Eifel region). Therefore a comparison between such mean value (that should represent the general moisture state of the observed area) and the short ranges might not be meaningful. The temporal evolution of the short range values is analysed in Figure 5.14. Here, no trend can be recognized either. This could be accredited to the low temporal frequency of the data, which makes small-scale changes invisible. What can be seen, is that in 2003 the short ranges do not reach values as low as in the other years. This might be an effect of the 2003 European heat wave that also struck Germany. Due to the drought, the vegetation influence on the spatial structure might have decreased, resulting in missing low short range values.

Korres et al. (2015) examined remotely sensed soil moisture products of the fertile loess plain of the Rur catchment with a spatial resolution of 15 m and 150. They found mean ranges at 432 m at 15 m resolution and 711 m at 150 m resolution using an unnested approach. These range values were associated with land use structure. In contrast to other data sets used in the study, no dependence on soil parameters was found for the remotely sensed soil moisture. (Reichenau et al., 2016) analysed spatial variabilities of LAI from modelling and remote sensing in the fertile loess plain of the Rur catchment. They used a nested approach and found short ranges between 150 and 320 m for separate crops and between 100 and 180 m for overall arable land which was attributed to field sizes. This is in line with the results of the current study.

Analysing the long ranges for the cases where a nested fit has been applied is more complicated, as these ranges vary a lot, up to maximum long ranges found at about 500 km, when the theoretical semivariogram does not converge optimally. In median, anyways, the long range is found at a length of about four km. The 10th and the 90th percentiles of the long range distribution are 1.8 km and 39.2 km, respectively, thus spanning a realistic range. Influences could be attributed to soil type, topography or local precipitation but cannot be clearly distinguished. The long ranges found in this study are higher than those found by Reichenau et al. (2016), but are at a comparable scale. They also attributed these range values to the effects of soil or weather.

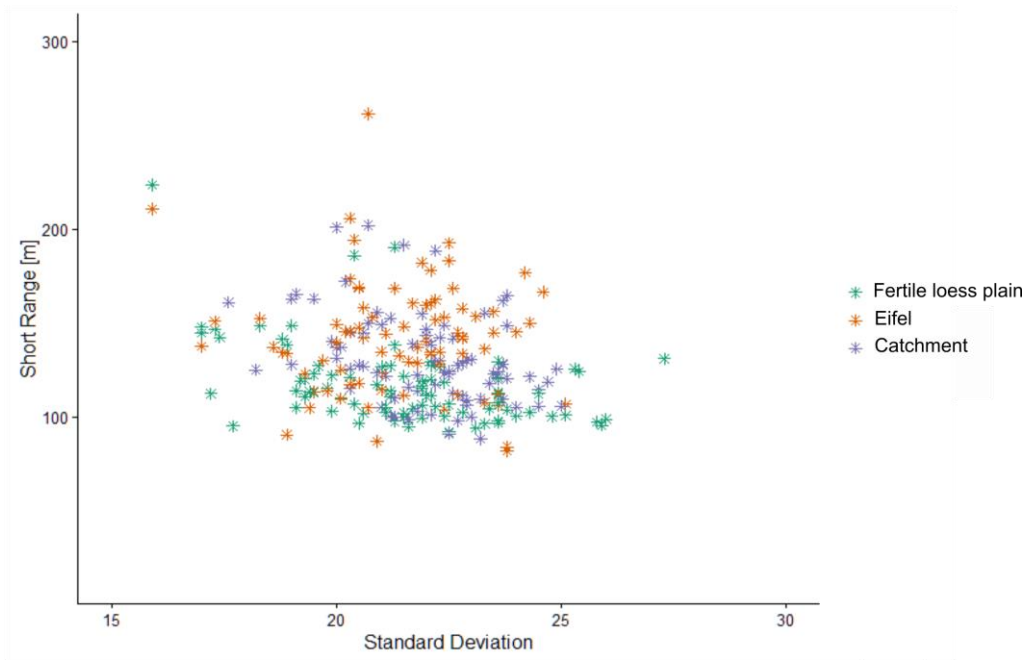


Figure 5.12. Relationship of short range to standard deviation for the fertile loess plain, Eifel and the whole catchment.

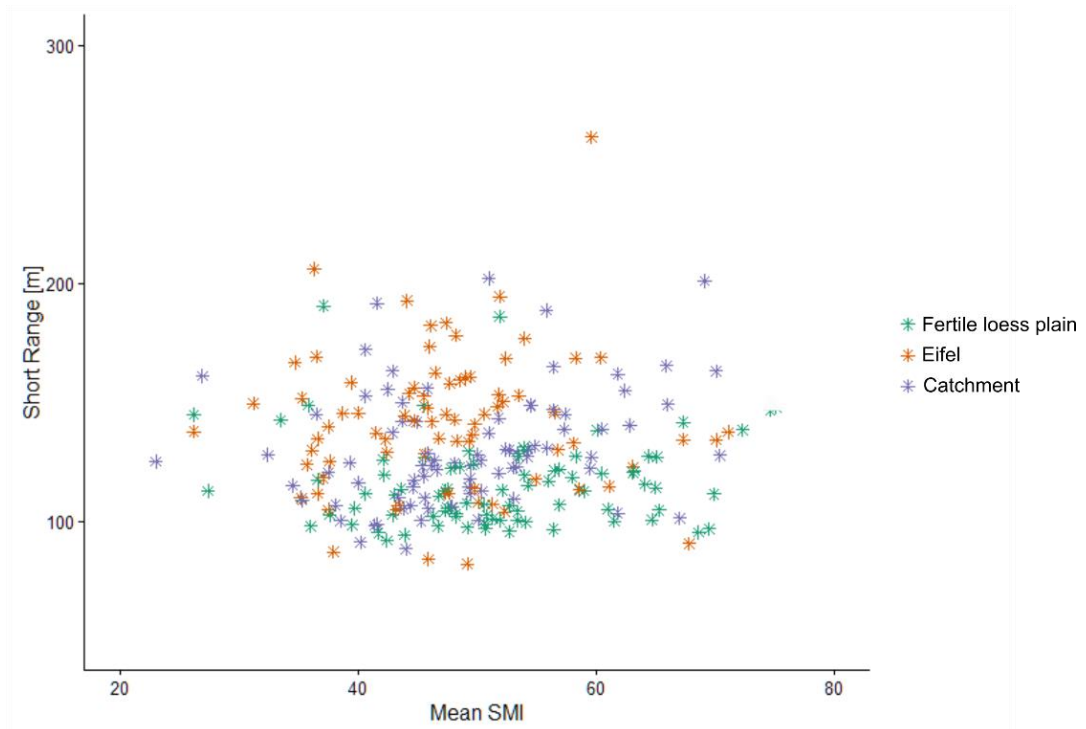


Figure 5.13. Relationship of short range to mean SMI for the fertile loess plain, Eifel and the whole catchment.

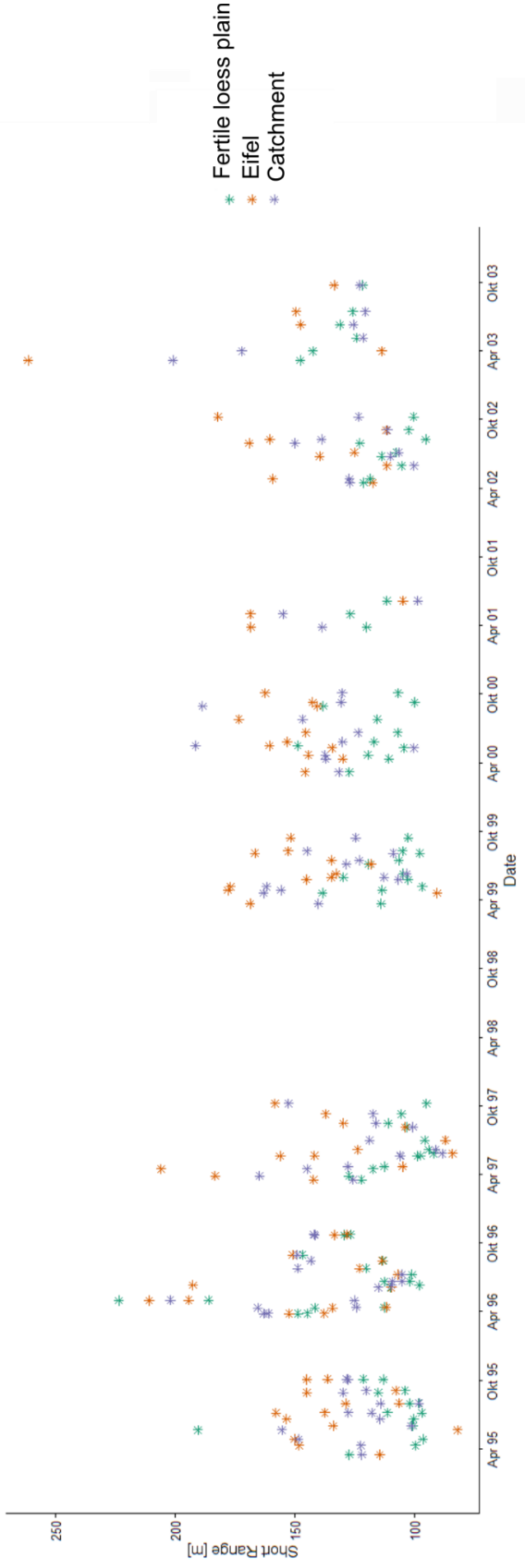


Figure 5.14. Temporal Evolution of short ranges in the whole Rur catchment, the Eifel region, and the fertile loess plain.

5.2.1 Summary Spatial Patterns of Soil Moisture in the Rur catchment

Regarding the spatial heterogeneity of soil moisture we found behaviour as described in literature, where standard deviation is highest at medium mean soil moisture values and is low in wet or dry areas.

The only clearly recognizable effect on the spatial structure of soil moisture in our study is the field size that represents differences in management and hereby for example differences in evapotranspiration between the fields. The same influence has been found in the Rur catchment before (Reichenau et al., 2016, Korres et al., 2015). As we had the opportunity to analyse a long time series of soil moisture data, we had expected to find temporal or seasonal trends in the soil moisture structure due to weather or climate influence on soil moisture distribution or a dependency on the soil moisture state like for soil moisture variability. Contrary to expectation, no trend or dependency has been found in our data, indicating that the SMI, at least with this spatiotemporal resolution, is not suitable to identify more complex factors that influence the structure of soil moisture.

5.3 Sensitivity of Sentinel-1A to Soil Moisture and Vegetation Characteristics

An analysis of sensitivity to different land surface parameters is the first step for developing (semi-) empirical retrieval schemes from SAR data. To examine the influence of soil moisture and vegetation parameters on SAR backscatter, we performed the analyses as described in chapter 4.8.2 and used correlation heat maps and signal analysis.

Overall, the correlation heat maps in the following chapters show, that H , A and α correlate strongly with each other ($\sim \pm 1$). They also correlate strongly ($> \pm 0.7$) with the crosspol-ratio, for all land use types except for grassland and triticale. This is interesting, as grassland and triticale are the only types of vegetation on our test sites that are not sown in rows and therefore supposedly exhibit a less ordered structure than e.g. wheat fields. A has no well-defined physical meaning for dual-pol data, and shows temporal courses that are identical to H in the signal analysis. Therefore, A is not analysed in detail.

The signal analysis also reveals, that H ranges between 0.5 - 0.9 in general when referring to the median and the IQR, thus indicating a medium to high depolarizing effect. Only for bare soil conditions and for vegetated areas with stubbles or very small plants (HW F01 2015-11-23 and HW F01 2015-05-15, SH F05 2015-11-23, SH F03 2016-05-09, SH F04 2016-05-09 respectively) H reaches values below 0.5, indicating a less depolarizing effect. The temporal course of Entropy resembles strongly the course of the crosspol-ratio for all types of vegetation

apart from grassland and triticale. Also for the crosspol-ratio, bare soil areas (and those with stubbles or very low vegetation or crop residues) produce much smaller values of under -10 dB compared to vegetated areas. Therefore, except for grassland and triticale, H is also no longer analysed in detail because H and the crosspol-ratio behave identically.

α stays in a range between 60° and 80° indicating multiple scattering as the dominant scattering effect. This is explained well by the fact that scattering from a natural surface is always a combination of scattering from the soil surface and the vegetation (or vegetation residues / stones etc. for the bare soil case) on the soil surface. There is no influence of land use type or vegetation stages on α and the temporal course of α shows no systematic variations. Therefore, it will not be considered during the signal analysis.

To sum up, H , A and α correlate strongly with each other and with the Crosspol Ratio and show either temporal courses that are identical to the Crosspol Ratio (in the case of A and H) or show no systematic variations at all (in the case of α). Therefore, we cannot use them as independent measures. Thus, it appears, that the polarimetric measures H , A and α do not add information to the analysis and therefore, examining γ_{0vv} , γ_{0vh} and the crosspol-ratio in the next chapters is sufficient. This would imply that the H2 α decomposition is unnecessary for our data (C-band, dual-pol, with high incidence angle) and application case. This is supported by Ji and Wu (2015) who found that for the dual-pol case the scattering mechanisms diffuse, so that clear classifications of different scattering mechanisms based on the H2A decomposition are difficult. This especially affects VV-VH or VV-HV SARs, like Sentinel-1, because the second copol-channel is missing.

5.3.1 Bare Soil Signal Analysis

Bare soil is the land use type for which most soil moisture retrieval models are developed (e.g. (Baghdadi et al., 2006, Fung, 1994, Hajnsek et al., 2003, Dubois et al., 1995)). Here, a high sensitivity of backscatter to soil moisture is expected, as no attenuating vegetation is present. Apart from the general observations made in chapter 5.3, the correlation heat map for bare soil (Figure 5.15) shows a medium positive linear correlation of soil moisture and γ_{0vv} and a smaller positive correlation with γ_{0vh} . For both polarizations, dry biomass has a weak negative correlation. This is reasonable, because backscatter should increase with increasing soil moisture but should be attenuated by increasing amounts of biomass on the field.

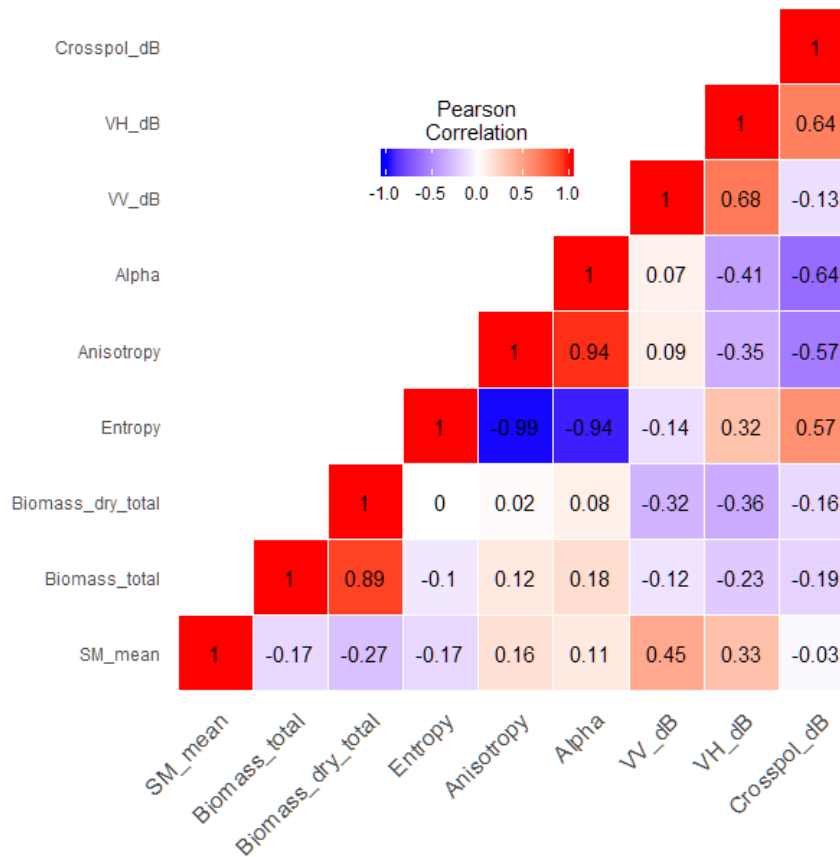


Figure 5.15. Correlation heat map for bare soil, showing the linear Pearson Correlation

For the signal analysis, the course of backscatter intensity on bare soil fields follows in general the trend of soil moisture, so that higher soil moisture produces higher backscatter. This trend can be seen more clearly in VV polarization. E.g. on 2015-11-23, 2015-08-19 and 2016-11-17 (Figure 5.16), γ_{0vv} mirrors the relatively high soil moisture and on 2016-09-30 the low soil moisture is expressed by low γ_{0vv} . When soil moisture stays constant, as for SH F04 on 2015-07-26, 2015-08-19 and 2015-10-30, γ_{0vv} stays constant as well. Strong differences in backscatter intensity with constant soil moisture can be attributed to strong differences in biomass in the form of harvest residues. For 2016-03-22, SH F04 shows soil moisture conditions comparable to the three before mentioned dates, but produces much lower γ_{0vv} . In contrast to the other three dates, where SH F04 is covered by harvest residues, it is completely bare in March.

On 2015-08-19, γ_{0vv} is significantly higher on SH F01 compared to SH F03 despite comparably high soil moisture conditions. SH F01 is only lightly covered by crop residues, whereas SH F03 is densely covered by crop residues and stubbles. This effect can only be observed in VV polarization and not in VH polarization. This indicates a strong effect of vertical structures (from the stubbles) to VV polarization as already described by Brown et al. (2003). In contrast to that,

the 2015-07-26 shows a much higher Crosspol Ratio on SH F05 than for the other dates or fields.

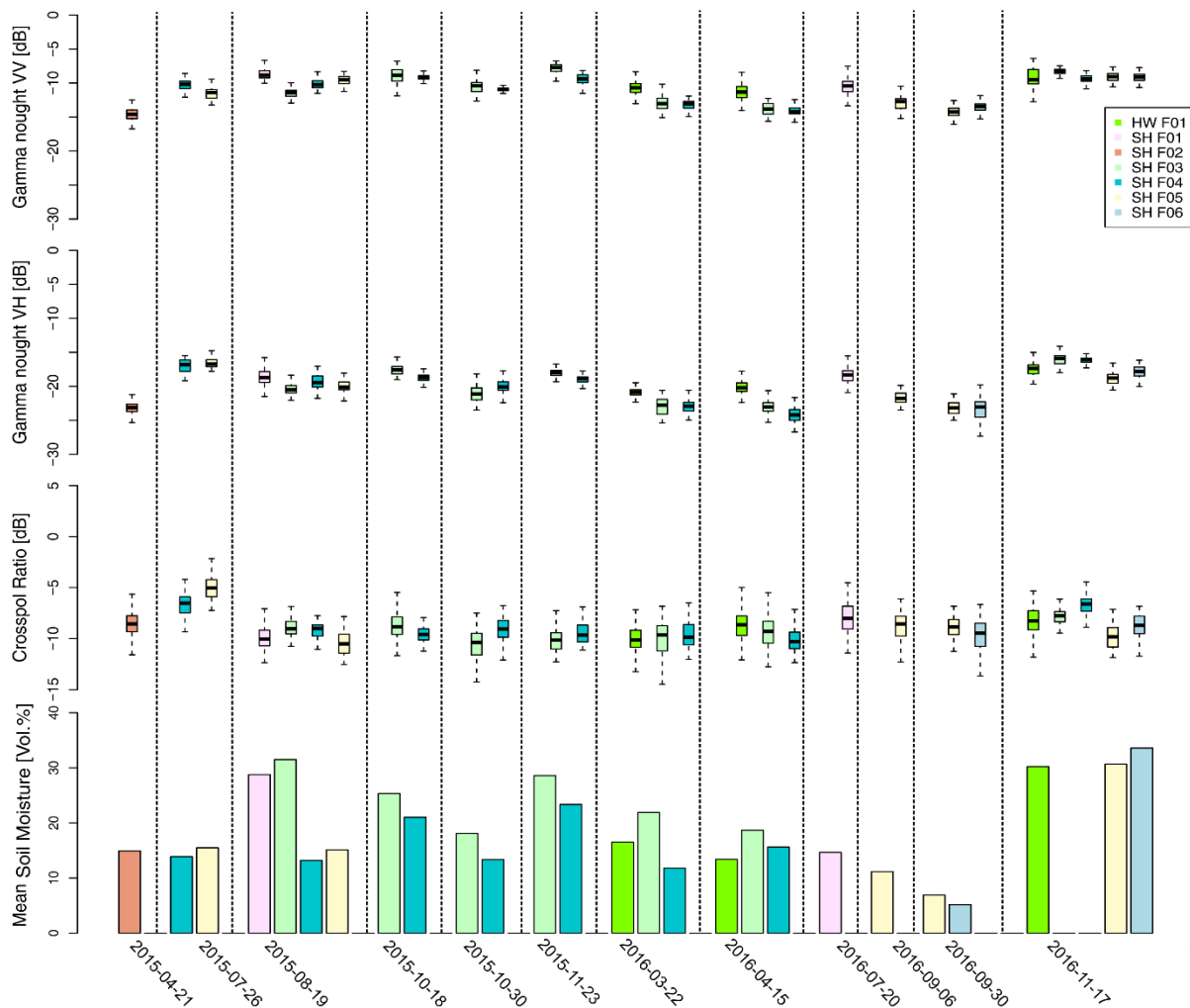


Figure 5.16. Histograms of backscatter per bare soil field in different polarizations and corresponding field mean soil moisture for different acquisition dates. Each date shows a different composition of bare soil fields, as they depend on harvest or seeding dates.

Indeed, this field was covered by huge piles of crop residues with very high biomass values. This effect cannot be seen in VV polarization, indicating that not only the amount of biomass but also its orientation (like more vertically oriented and distributed or unordered like in a pile) plays a major role in the backscatter process. As already mentioned in the last chapter, bare soil fields (and fields with stubbles or very small vegetation, as will be shown in the following chapters) show the overall smallest values in Crosspol Ratio, with median and the IQR around -10 dB. This can be well explained by the fact that the copol backscatter is high on bare soil fields in relation to the crosspol backscatter (Vecchia et al., 2008). Nevertheless, there are values above the IQR that reach backscatter levels comparable to those of vegetated areas. And vice versa for vegetated areas, values below the IQR can be found reaching as low as -10 dB in

Crosspol Ratio. This indicates that the Crosspol Ratio can be used to differentiate between vegetated areas and bare soil fields and could help to estimate harvest dates. But without prior knowledge of the vegetation type and its crop cycle or the field borders to calculate field mean values, the classification of bare soil pixels based only on the Crosspol Ratio is prone to errors. Still, this relationship can help to improve land use classifications or to set harvest dates in environmental models when it is applied to time series of SAR backscatter, or when field borders are known and field mean values can be calculated.

In summary, γ_{0vv} on bare soil fields, is influenced by the amount of soil moisture (acting amplifying) and the amount of biomass (acting attenuating) on the field. The VH polarization shows no systematic course and the Crosspol Ratio reacts only to large amounts of biomass like on vegetated areas, or areas with huge piles of harvest residues.

On 2016-11-17 for SH F03 and SH F04 no soil moisture information is available, because the fields were covered with puddles of rain.

5.3.2 Sugar Beet Signal Analysis

The Rur catchment is situated in one of the major sugar beet cultivation areas in Germany. Sugar beet is mainly used to produce sugar and is an important economic factor for the area, with several sugar factories nearby. Therefore, sugar beet makes up most of the arable land of the Rur catchment together with cereals. Sugar beet and root crops in general are different from cereals or maize, as most of their biomass is below ground. Therefore, we expect a distinct interaction with incoming microwaves.

The correlation heat map for sugar beet (Figure 5.17) reveals a very low positive correlation between soil moisture and γ_{0vv} and γ_{0vh} and a medium positive correlation between biomass, biomass density and VWC with both γ_{0vv} and γ_{0vh} . Both polarizations also show a high correlation with canopy height. Regarding the in-situ measured vegetation parameters, canopy height has a very strong positive linear correlation with all vegetation parameters, except for brown LAI. Also, green LAI correlates strongly with wet and dry biomass and VWC. This is very interesting, as biomass of sugar beet accumulates mainly below ground in the root and is not easy to detect from remote sensing. LAI and canopy height can either be assessed by optical remote sensing or can be easily measured, so that these parameters could be used to derive sugar beet biomass. In the boxplots (Figure 5.18) the most striking feature is the strong increase in backscatter intensity after 2015-05-15 and 2016-05-09. This is most significant in γ_{0vv} and

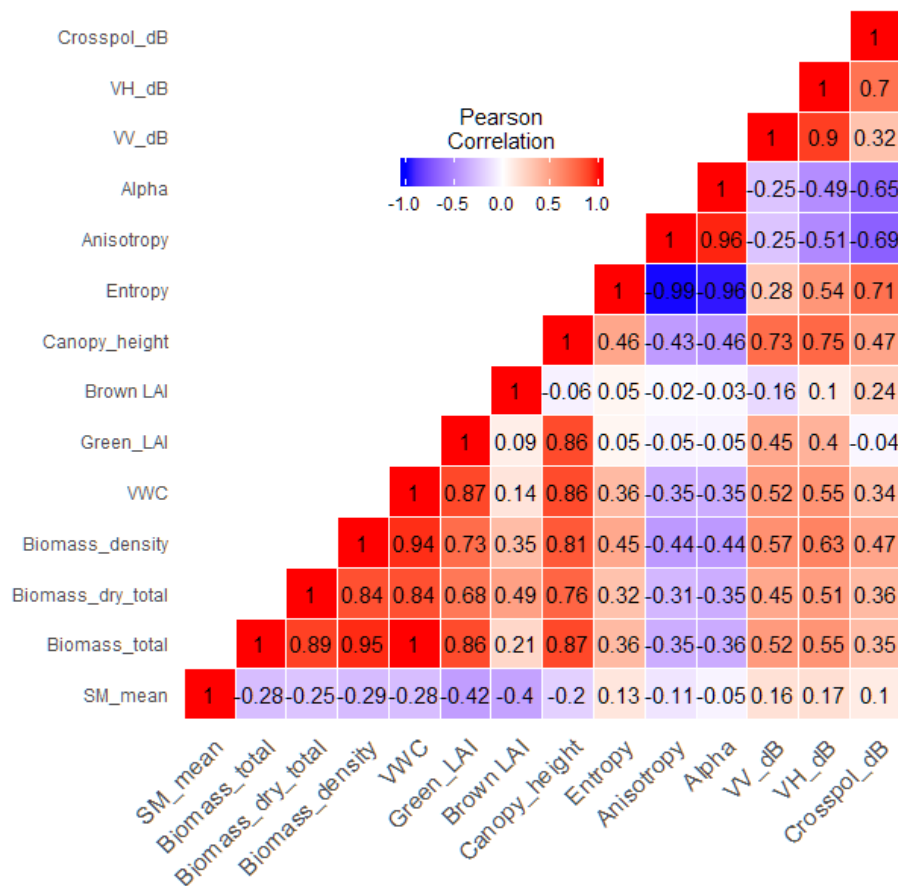


Figure 5.17. Correlation heat map for sugar beet, showing the linear Pearson Correlation.

γ_{0vh} and can be attributed to vegetation growth. On 2015-05-15 and 2016-05-09 the sugar beet plants are still very small, so that much bare soil is visible. On the following measurement dates, the plants are already high and the canopy is almost closed. After this canopy closure, biomass and LAI increase further, but γ_{0vh} stays constant. In VV polarization we find variations in the course that cannot be easily explained by soil moisture or vegetation parameters. In 2016, where we have two different sugar beet fields, we can make out a soil moisture influence in the sense that, in most cases the field with higher soil moisture content generates higher γ_{0vv} . The Cross-pol Ratio shows the exact opposite effect, resulting in higher backscatter from fields with lower soil moisture content.

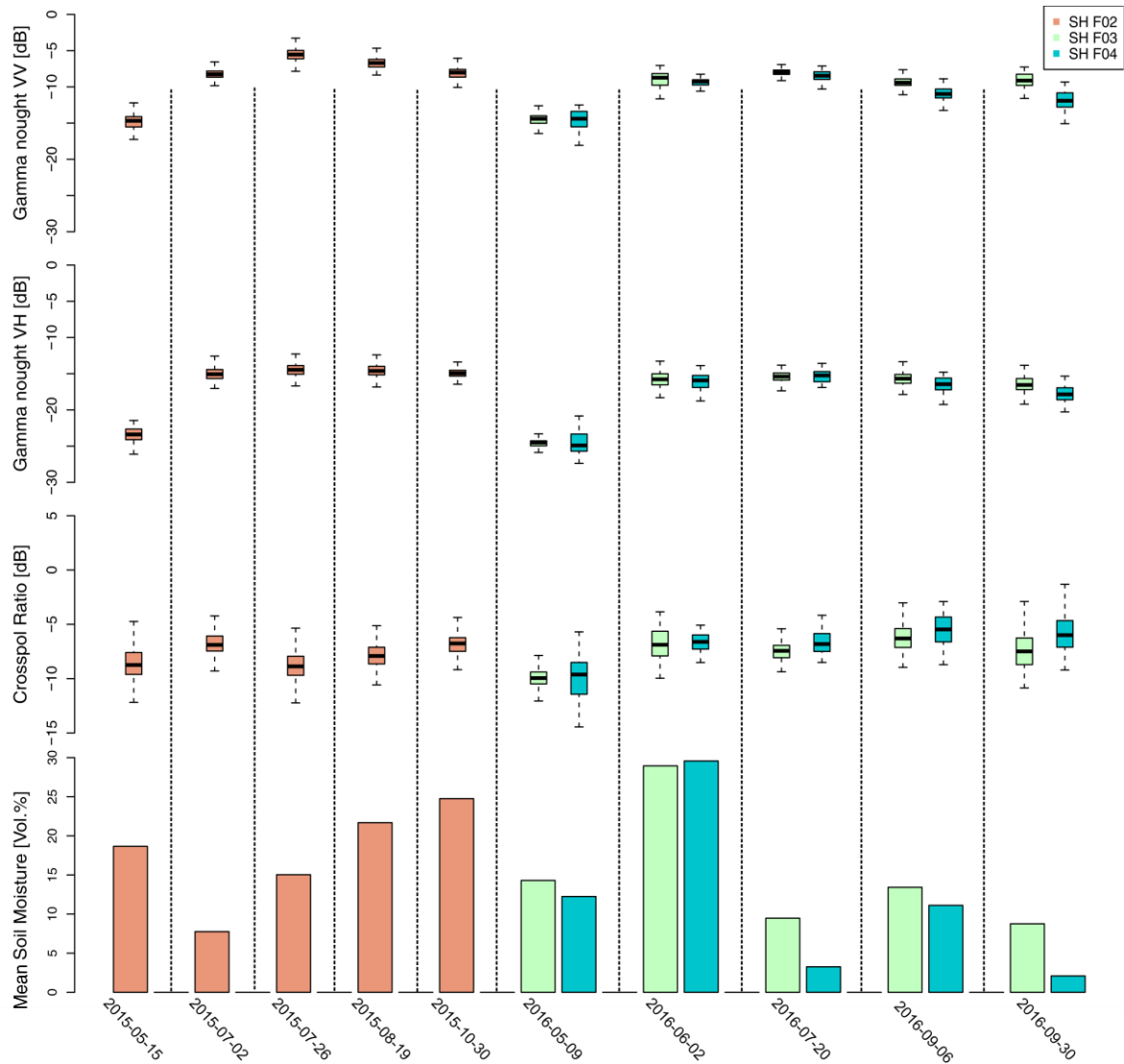


Figure 5.18. Histograms of backscatter per sugar beet field in different polarizations and corresponding field mean soil moisture for different acquisition dates. Whereas in 2015 one fields is covered with sugar beet, two fields are covered with sugar beet in 2016.

5.3.3 Cereal Signal Analysis

Cereals are the most important crops in the state of North Rhine-Westphalia in Germany and therefore also constitute the main crop in the Boerde region of the Rur catchment. Both winter wheat and winter barley are cereals that are, in contrast to triticale, sown in rows. Therefore, they will be analysed jointly in the following chapter.

Whereas both correlation heat maps (Figure 5.19 & Figure 5.21) show a medium to high linear correlation of Crosspol Ratio to green LAI, the Crosspol Ratio for winter barley is also sensitive to biomass density. Winter wheat shows a high linear correlation in γ_{0vv} to the green and brown LAI and for winter barley, γ_{0vv} correlates with a medium to high intensity with both green LAI and biomass density. Winter wheat shows a medium linear correlation between γ_{0vh} and dry biomass and brown LAI, whereas winter barley has a medium linear correlation of γ_{0vh} to soil

moisture. Winter wheat shows a low linear correlation to soil moisture for γ_{0vv} . This is in line with results from Mattia et al. (2003), who found high soil moisture sensitivity under winter wheat only for HH polarization, which is not available from our data. In contrast to our data, they used an incidence angle of 23° , which is furthermore less influenced by vegetation than a high incidence angle.

Regarding the ground measurements, we find medium to high linear correlations between canopy height and total and dry biomass for both crops and a high correlation with VWC for winter barley. The green LAI correlates strongly with biomass density for both crops, whereas for winter barley it correlates also strongly to VWC and total biomass. The brown LAI has a medium to strong correlation with dry biomass and biomass.

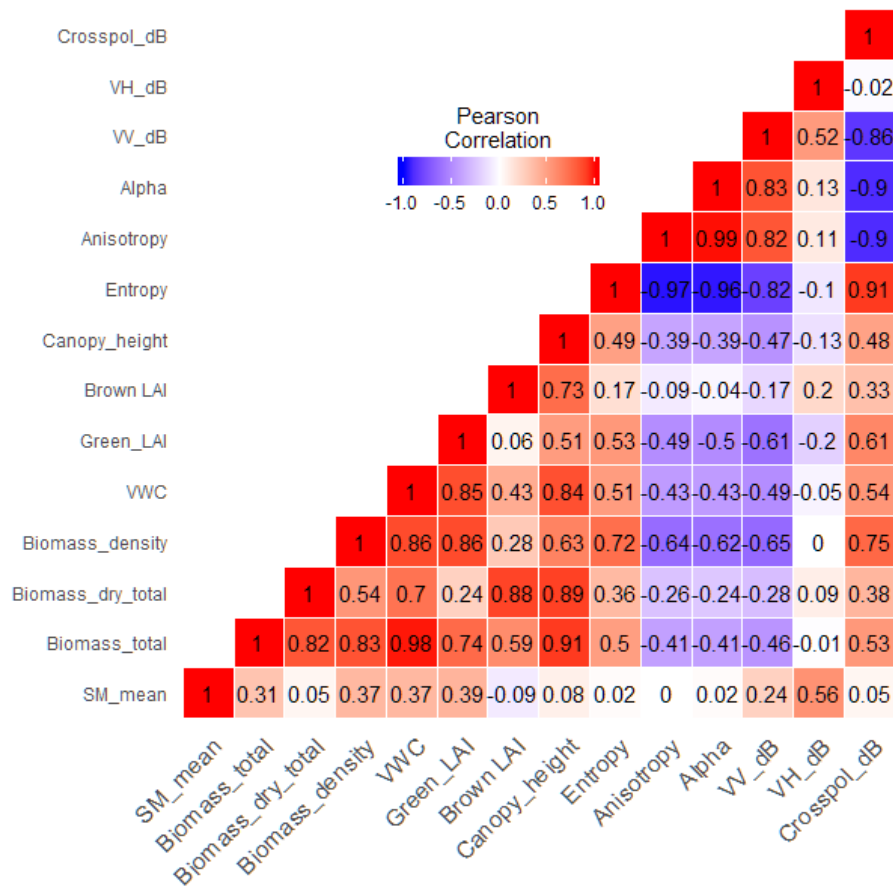


Figure 5.19. Correlation heat map for winter barley.

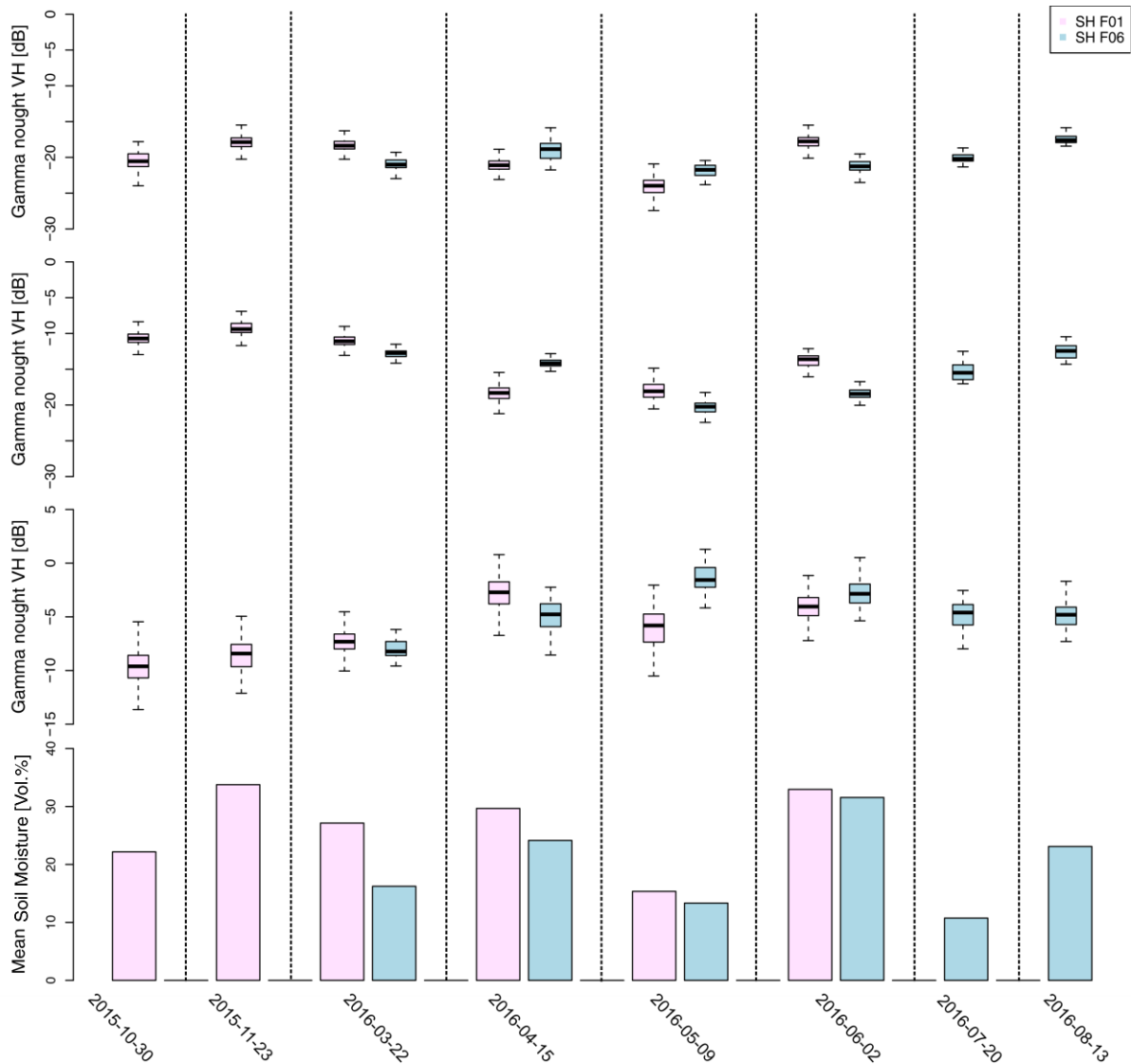


Figure 5.20. Histograms of backscatter per winter barley field in different polarizations and corresponding field mean soil moisture for different acquisition dates.

In the signal analysis for both cereals (Figure 5.20 & Figure 5.22), γ_{0vh} and γ_{0vv} seem to decrease with biomass accumulation as long as the plant is predominantly green (for winter wheat from 2015-04-21 to 2015-05-15 and from 2015-11-23 to 2016-05-09 and for winter barley from 2015-11-23 to 2015-05-09). For 2015-10-30 to 2015-11-23, there is a slight increase in backscatter for all polarizations. In the Crosspol Ratio, the backscatter on 2015-10-30 is around -10 dB, comparable to bare soil conditions. Indeed, the vegetation on that date is still minimal, with bare soil dominating the field. But as the Crosspol Ratio on the next date is only slightly higher, despite a considerable vegetation cover, an automated bare soil recognition based only on the value of the Crosspol Ratio would fail, as explained in 11.3.1.

As soon as the plant gets drier and brown LAI starts to increase (in May), γ_{0vh} and γ_{0vv} start

to increase as well. Veloso et al. (2017) also found an increase in both VV and VH polarization from cereal fields starting in May on test sites in southwest France. They accredited this to the heading that causes an increase in fresh biomass. Apart from a possible amplifying (winter wheat 2015-07-27) or attenuating effect (winter wheat 2015-07-02), soil moisture seems to have no effect on the course of the backscatter intensities. On 2015-04-21 and 2015-05-15 the winter wheat fields SH F01 and SH F05 generate lower backscatter compared to SH F03 in both VV and VH polarization. In Crosspol Ratio the effect is reversed. On SH F01 and SH F05, the biomass amount is higher compared to SH F03. Therefore, also the absolute amount of biomass seems to influence the backscatter intensity and not only the vegetation cycle. On 2015-07-26 SH F05 is already harvested, while winter wheat still covers the other fields.

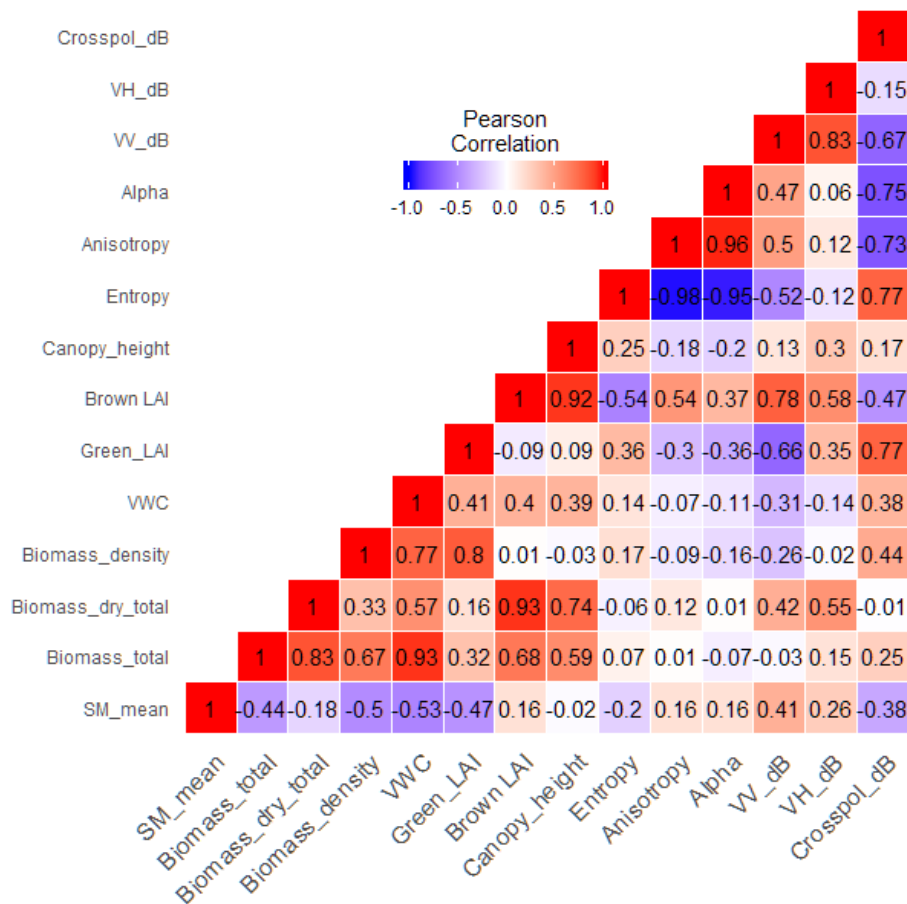


Figure 5.21. Correlation heat map for winter wheat.

The winter barley field SH F06 is delayed in its vegetation development compared to SH F01. This can also be seen in a delay in the backscatter courses as described above (e.g. SH F01 backscatter starts increasing on 2015-04-21, whereas SH F06 starts increasing from 2015-05-09 and is harvested later). It is sown later and harvested later than SH F01.

For the Crosspol Ratio, the study by Veloso et al. (2017) found a high sensitivity towards the growth cycle of winter wheat and barley. The Crosspol Ratio increases at the tillering stage around March and decreases during senescence at early June until harvest in their study. Apart from an increase in backscatter for both winter wheat and barley from March to April 2016, this course cannot be seen clearly from our data. This can be due to the lower temporal resolution of our data that do not show every detail of the growth cycle. The study also found a higher correlation of the Crosspol Ratio to fresh biomass than to photosynthetic activity, which is not present in our correlation analysis.

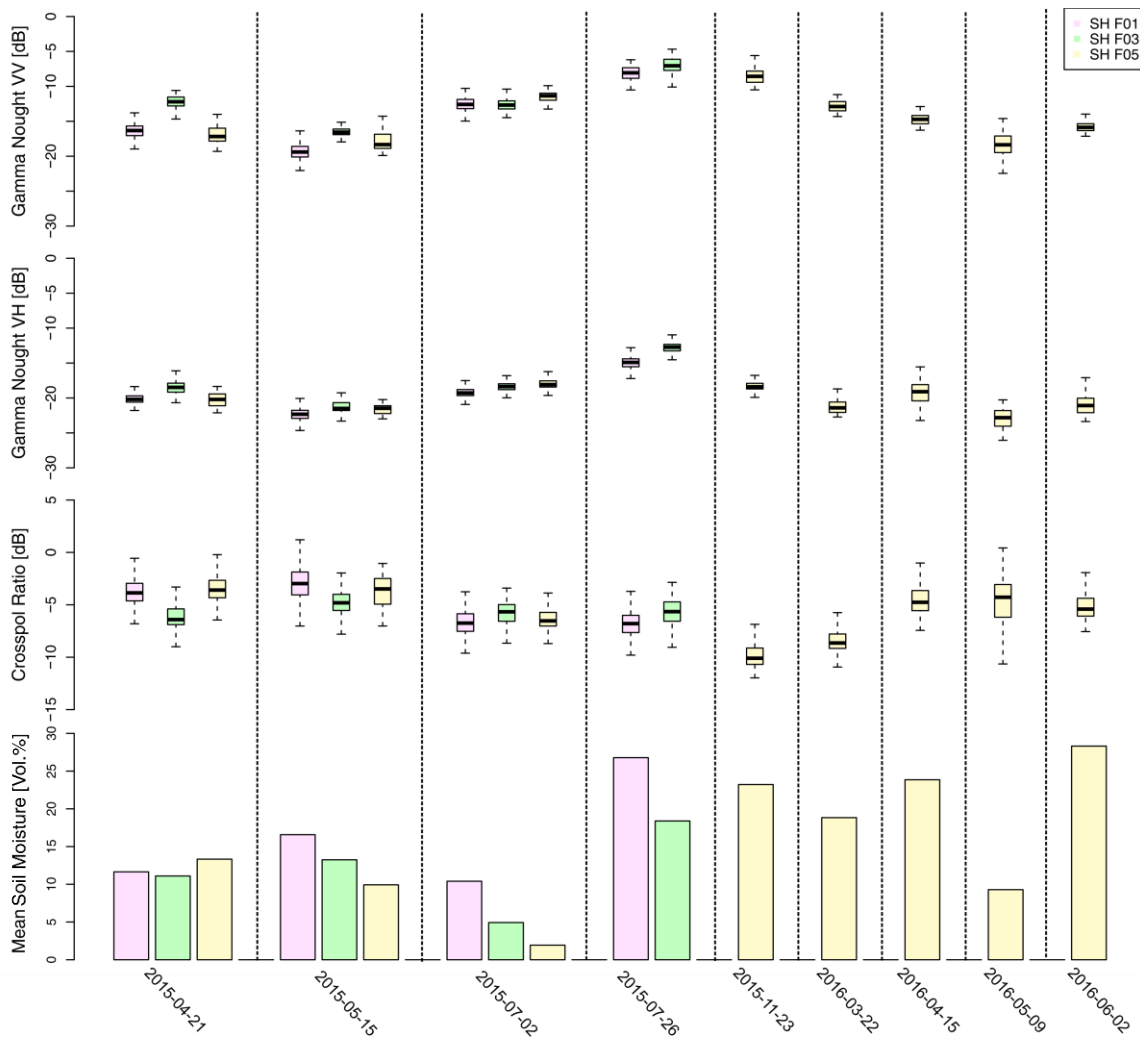


Figure 5.22. Histograms of backscatter per winter wheat field in different polarizations and corresponding field mean soil moisture for different acquisition dates. Whereas in 2015 three fields are covered with winter wheat, only one field is covered with winter wheat in 2016.

In general, the backscatter on cereal fields reacts differently, depending on whether the vegetation is still completely green or getting brown. Therefore, we expect to find an empirical relationship of backscatter intensity to green and brown LAI. As the biomass amount seems to have

amplifying effects, we expect a relationship with total biomass as well. No discrete influence of soil moisture could be found.

5.3.4 Maize Signal Analysis

Despite only covering a small percentage of area in the Rur catchment when compared to sugar beet and cereals, maize is an important crop to produce animal feeding and biomass. Several studies, aimed at understanding microwave interactions with vegetation, concentrate on maize (Vecchia et al., 2008, van Emmerik et al., 2015, Bériaux et al., 2015). Therefore, studying the sensitivity of S1A backscatter to maize fields is of great interest. In contrast to cereal stubbles that we assigned to the bare soil class, as they did not show a substantial effect on the cereal parameter retrieval, we kept maize stubbles in the class maize because they still have high biomass and we also expect a strong structural effect for example on the retrieval of canopy height when including maize stubbles in the maize analysis.

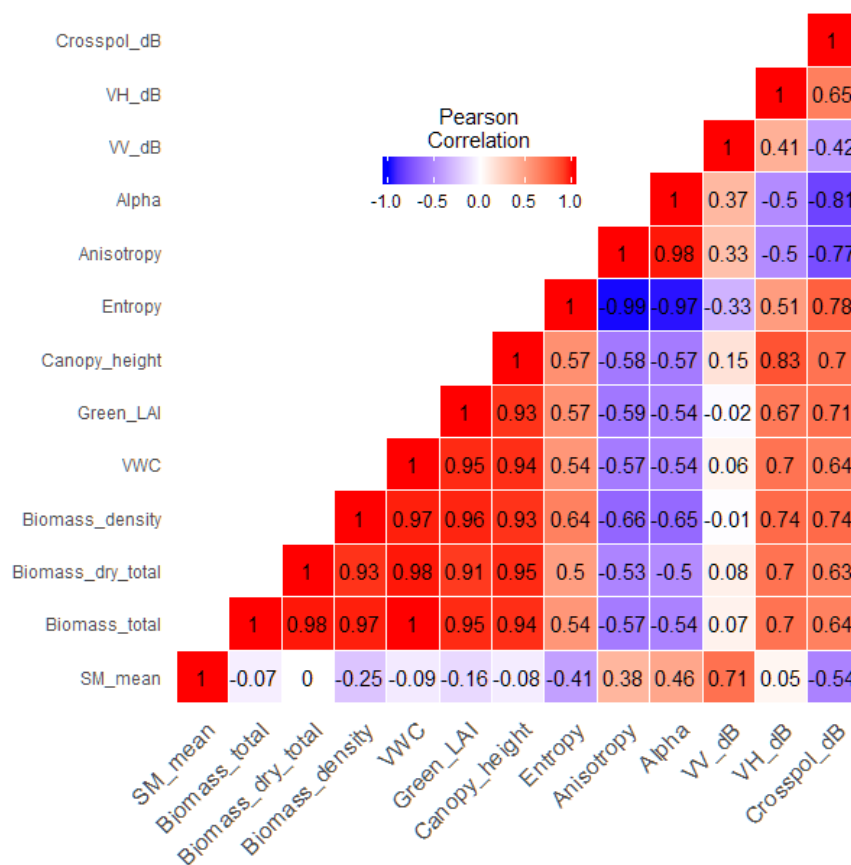


Figure 5.23. Correlation heat map for maize.

In contrast to the other vegetation types, Maize shows to have a strong linear correlation of γ_{0vh} and the Crosspol Ratio to all vegetation parameters (Figure 5.23). On the other hand γ_{0vv} , shows almost no sensitivity to vegetation at all, but is correlated strongly with soil moisture. This is surprising first, as maize fields are so densely vegetated when fully grown, that C-band micro-waves should not reach the ground. Compared to cereals and sugar beet however, the row distance of maize is much higher, so that more incoming microwaves can reach the soil. It is also remarkable that the vegetation parameters correlate nearly perfectly with each other. Such strong correlation cannot be found for any other vegetation type.

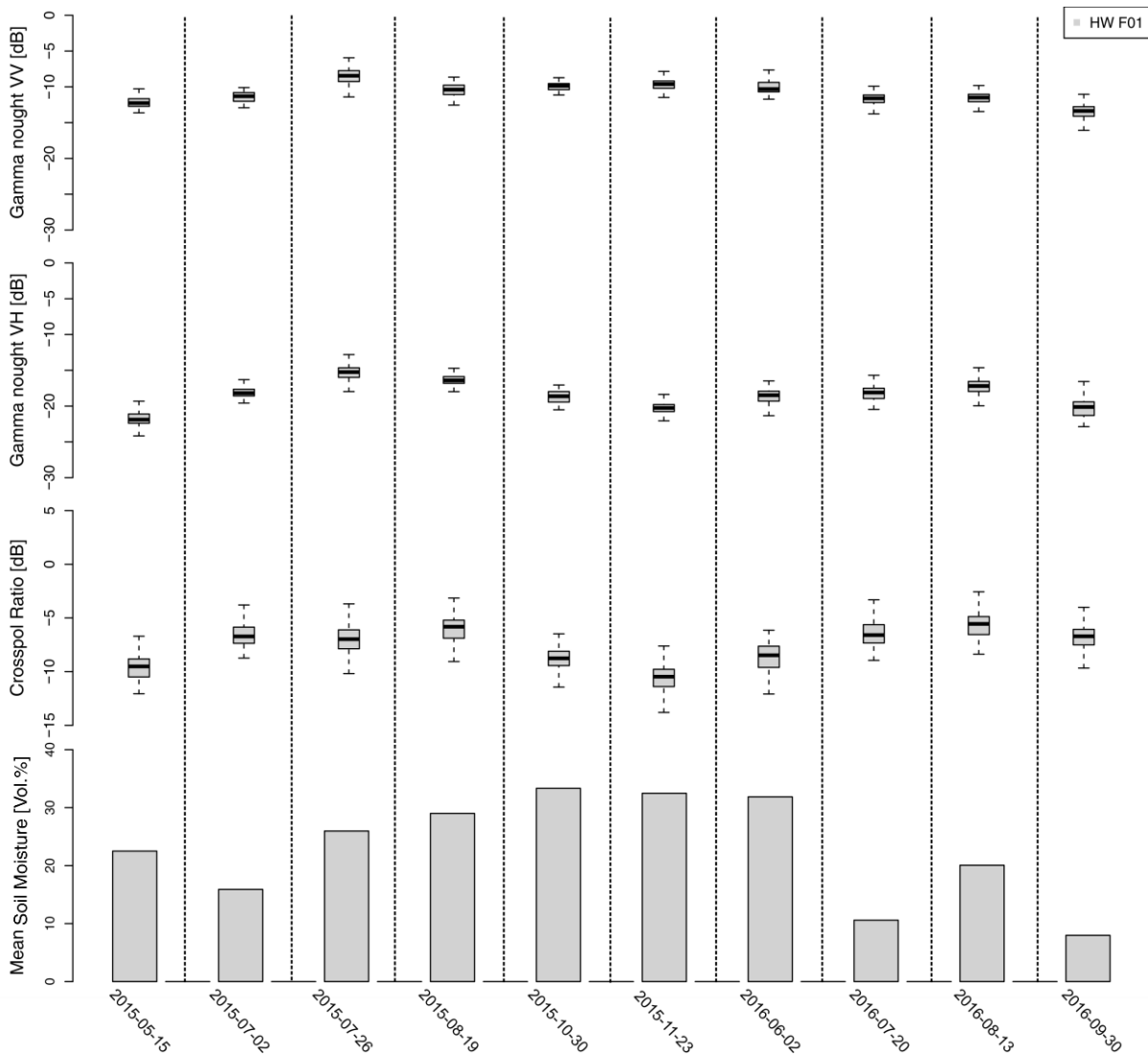


Figure 5.24. Histograms of backscatter per maize field in different polarizations and corresponding field mean soil moisture for different acquisition dates.

The signal analysis (Figure 5.24) of maize shows not much variability in γ_{0vv} that could be accredited to the vegetation cycle. The correlation heat map (Figure 5.23) already indicated this. Differences in backscatter intensity with comparable vegetation conditions (like very small plants on 2015-05-15 and 20160602 or stubbles 2015-11-23 and 2016-09-30) can be attributed to different soil moisture states.

Both γ_{0vh} and the Crosspol Ratio show clear responses to vegetation growth and biomass accumulation. Backscatter in both polarizations increases with vegetation development from the state of very small plants (2015-05-15 and 2016-06-02) until harvest (after 2015-08-19 and 2016-08-13). This behaviour has also been observed by Veloso et al. (2017). Therefore, a time series of γ_{0vh} or crosspol backscatter could be used to determine harvest dates of maize when no ground information is available.

A further decrease after harvest (from 2015-10-30 to 2015-11-23) has been found in the study by Veloso et al. (2017) as well and was accredited to standing green residues or weed. Indeed, on photos from the fields on these dates we find weed on the field on 2015-10-30 and no green vegetation at all on 2015-11-23. Therefore we agree with the assumption by Veloso et al. (2017).

5.3.5 Grassland and Triticale Signal Analysis

Grassland areas cover a large part of the total area of the Rur catchment, particularly in the Eifel region. Cultivating agricultural areas with grassland rather than converting them to arable land is supported by EU funds to increase biodiversity and reduce carbon dioxide emissions. Therefore, cultivating grassland is especially profitable for areas with low harvest yields, for example because of topography like in the Eifel region. Furthermore, grassland constitutes a challenge for soil moisture retrieval because of complex scattering interactions with the thatch layer that can contain large amounts of water (Saatchi et al., 1994).

Although triticale is a cereal like winter wheat or winter barley, it is used as a cash crop on our test sites and is therefore not sown in rows, resembling grassland, and covered the fields only for short periods. Consequently, we analyse triticale together with grassland.

The correlation heat maps for triticale and grassland (Figure 5.25 & Figure 5.27) are characterized by a very pale colour spectrum, indicating overall low linear correlations with the SAR observables. Low to medium linear correlations can only be seen for canopy height (with γ_{0vv} and the Crosspol Ratio for grassland and with γ_{0vh} and the Crosspol Ratio for triticale). Soil moisture has a low linear correlation with γ_{0vv} and γ_{0vh} for triticale.

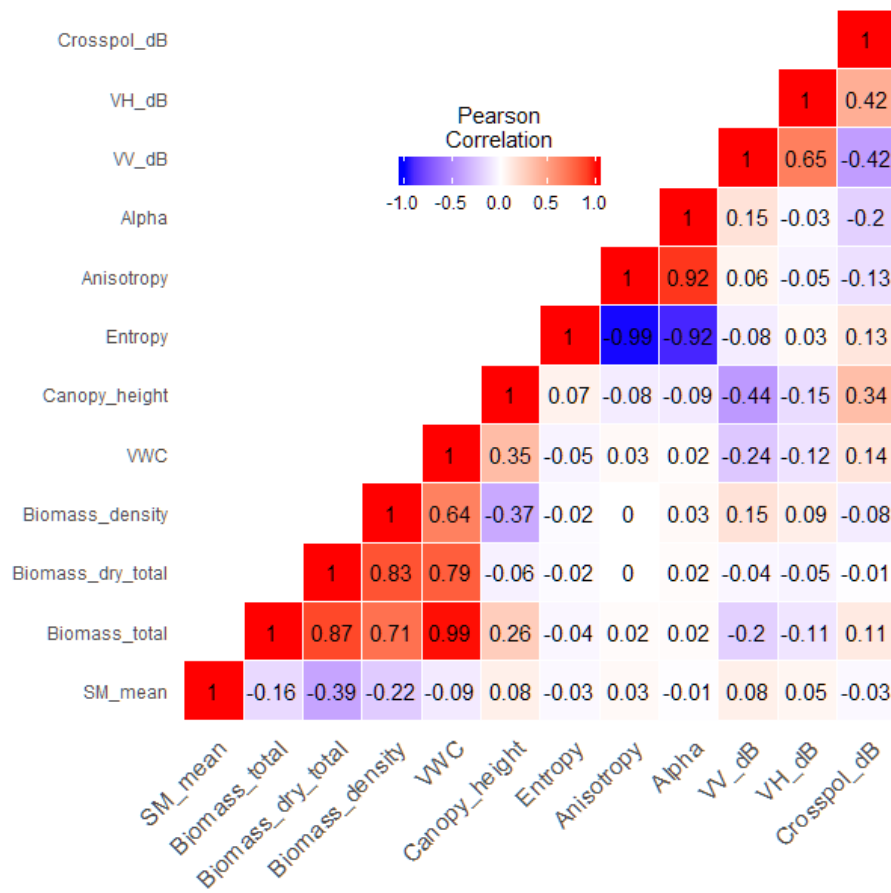


Figure 5.25. Correlation heat map for grassland.

The histograms for pasture and triticale (Figure 5.26 & Figure 5.28) show no recognizable system. They fluctuate barely around the value of -15 for γ_{0vv} and -20 for γ_{0vh} . Therefore, no influence of soil moisture or any vegetation parameter can be recognized. Also, relative differences between the two grassland fields cannot be attributed to differences in soil moisture or to a systematic difference due to e.g. soil type or topography. For triticale, we do not cover full vegetation periods but only periods of two (2015) or three dates (2016). Still, we do not see any effects of vegetation growth on the backscatter from one to the next date.

Biomass accumulation for grassland is governed by cutting dates. As we have no information about the cutting dates on our research fields, we cannot examine their influence. However, no strong variation is found for the backscatter signatures that would indicate a harvest event.

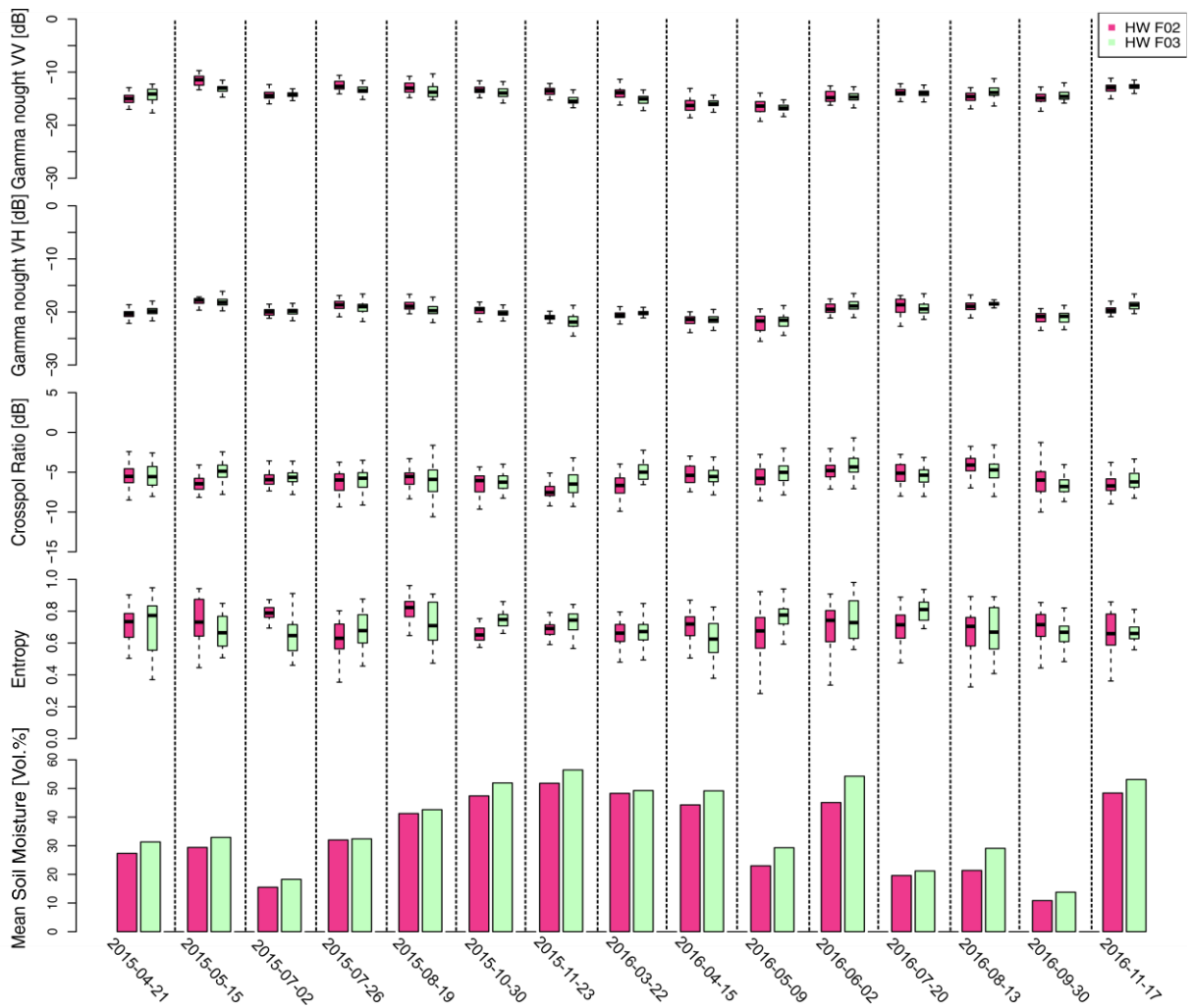


Figure 5.26. Histograms of backscatter per grassland field in different polarizations, entropy, and corresponding field mean soil moisture for different acquisition dates.

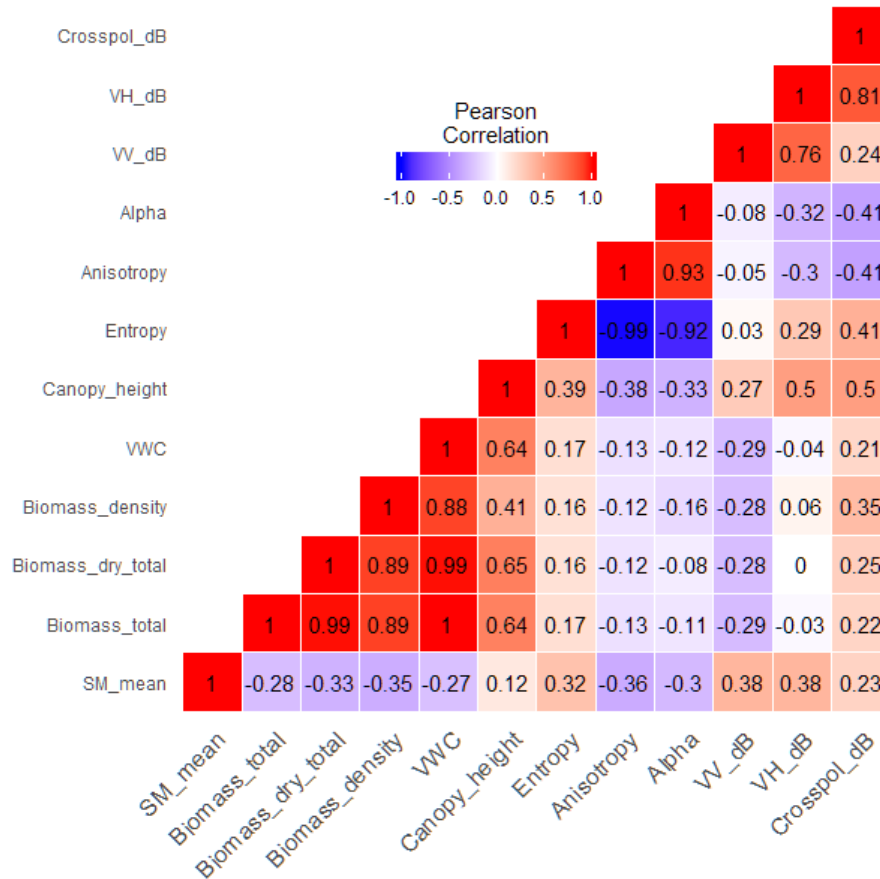


Figure 5.27. Correlation heat map for triticale.

In contrast to all other discussed land use types, H shows no identical course to the Crosspol Ratio for triticale and grassland. This can be seen for example on 2016-05-09 for triticale, where the Crosspol Ratio increased from 2016-04-15 but the entropy decreases. For pasture, this becomes clear especially when comparing the relative differences in the two fields. On 2015-05-15 for example the Crosspol Ratio is higher for HW F03 than for HW F02 but H is lower for HW F03 than for HW F02. Also on 2015-10-30 the Crosspol Ratio on HW F02 is higher than on 2015-11-23, whereas H increases between the two dates. This might be due to the fact that both the triticale and grassland fields are not sown in rows, which stand in contrast to the other vegetation types that are sown in rows. Consequently, the course of H relative to the Crosspol Ratio could be utilized to distinguish fields that are sown in rows from those without a structured sowing. Nevertheless, the temporal course of H (and of A and α) shows no systematic behaviour and the correlation to all ground measures is low.

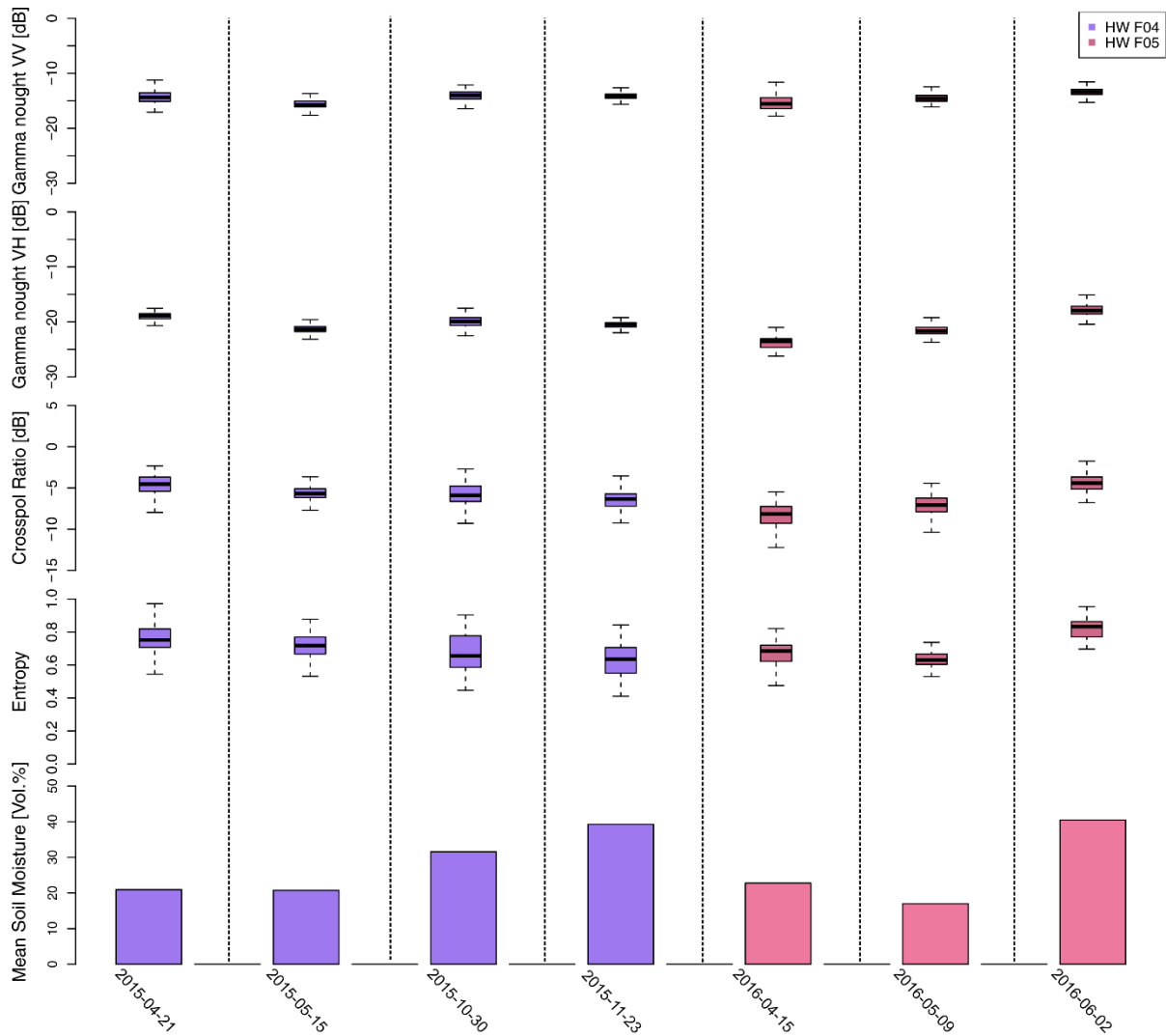


Figure 5.28. Histograms of backscatter per triticale field in different polarizations, entropy, and the corresponding field mean soil moisture for different acquisition dates. In 2015 and 2016 different fields were vegetated with triticale.

5.3.6 Signal Analysis Summary

The signal analysis in the last chapters has shown that different types of land use influence backscatter from C-band SAR in different ways. Bare soil is mainly influenced by soil moisture and roughness induced by large amounts of dry biomass in the form of huge piles of crop residue on the harvested field. This raises the question how to define the class bare soil and what to assign to this class. When the vegetation cycle is known, the course of the Crosspol Ratio could be used to identify whether a field is harvested, or rather bare soil.

Backscatter from sugar beet is mainly influenced by the canopy height and that from cereal fields depends on the development of green and brown LAI. Backscatter from both vegetation types shows no clear sensitivity towards soil moisture.

Maize seems to have an influence on γ_{ovh} and the Crosspol Ratio, evoked by all vegetation components. Basically, their backscatter intensity depends just on the vegetation growth and

accumulation of biomass. In contrast to that stands γ_{0vv} , that seems to be influenced mainly by soil moisture.

Grassland and triticale are a special case in our analysis, because they are the only plants not sown in rows. As they are also the only vegetation types that show a difference in the course of H and the Crosspol Ratio, this difference could be exploited to identify fields that are seeded in rows. Apart from that, no sensitivity to soil moisture or any vegetation parameter has been found for grassland and triticale.

How far these influences can be quantified and utilized to develop retrieval models, is examined in the following chapter.

5.4 Retrieval of Soil Moisture and Vegetation Parameters from Dual-Polarized S1A Data

After the qualitative analyses in chapter 5.1., this chapter is dedicated to the development of quantitative retrieval models. It will validate their performance, like explained in chapter 4.8.2.

5.4.1 The Bare Soil Model

Fields, that are classified as bare soil can have different appearances. Therefore, the class bare soil could be subdivided further into pure bare soil, bare soil with harvest residues or stubbles (after cereal or maize harvest) and freshly ploughed bare soil (that shows high surface roughness). Especially regarding stubbles and crop residues it is not trivial to decide whether to assign a field to the bare soil class or to the class of its original vegetation. In this study, we assigned stubbles and crop residues from cereals to the class bare soil, because even when the stubbles are still standing, many crop residues cover the surface, so that the overall appearance of the surface is very heterogeneous and not comparable to not yet harvested cereals. In contrast to that, maize stubbles still have a homogenous surface appearance, because the fields are not covered with residues. Therefore, and because of the sensitivity of SAR measures to the canopy height of maize, maize stubbles are assigned to the class Maize.

On bare soil fields, both the amount of soil moisture and the biomass on the field have an (opposing) effect on the backscatter intensity, with VV polarisation being more sensitive so soil moisture (c.f. chapter 5.3.1) than VH. Therefore, for the simplest form of a model to retrieve soil moisture from bare soil, we compared γ_0 backscatter to measured soil moisture. As expected, the relationship between soil moisture and γ_{0vv} is strongest. It can be explained by a linear model as derived from Figure 5.29:

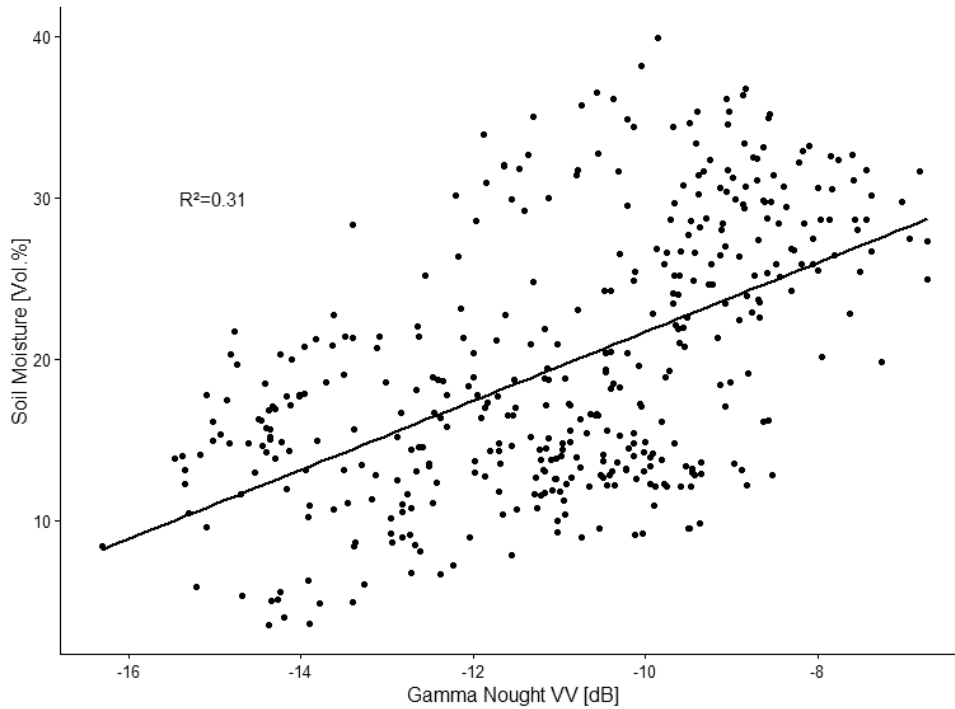


Figure 5.29. Relationship between surface soil moisture [Vol.%] and γ_{0VV} [dB] for bare soil with linear model and corresponding R^2 .

$$SM[Vol. \%] = 43.04 + 2.14 \gamma_{0VV} \quad (5.1)$$

The model is calculated from the whole data set and shows an adjusted R^2 of 0.31*** (***) indicates a highly significant relationship with a p-value < 0.001). Adding more parameters like biomass information or the Crosspol Ratio did not improve the relationship (adjusted R^2 of 0.27*** for both). Neither restricting the model to bare soil subclasses, like pure bare soil without crop residues and stubbles did have a strong impact (adjusted R^2 of 0.34***). This is a consequence of our findings in chapter 5.3.1, which have shown that besides soil moisture, also crop residues and stubbles have an influence on the backscatter intensity but this influence cannot be quantified. Consequently, we defined fields with non-vegetated soil, soil with harvest residues and soil with cereal stubbles as bare soil fields. Fields with maize stubbles were assigned to the class maize as explained earlier.

As soil moisture does not have a direct influence on SAR backscatter, but an indirect influence via the relative dielectric constant of wet soil, most soil moisture retrieval models use the relative dielectric constant (as calculated e.g. with Topp et al., 1980) instead of soil moisture to develop a retrieval model. This conversion did not improve our model. Also averaging the data and working on field mean scale, did not have a significant influence on the results. Therefore, we use (5.1) to estimate volumetric soil moisture from γ_{0VV} directly (Figure 5.30). The mean *RMSE* when using equation (5.1) is given in Table 5.2.

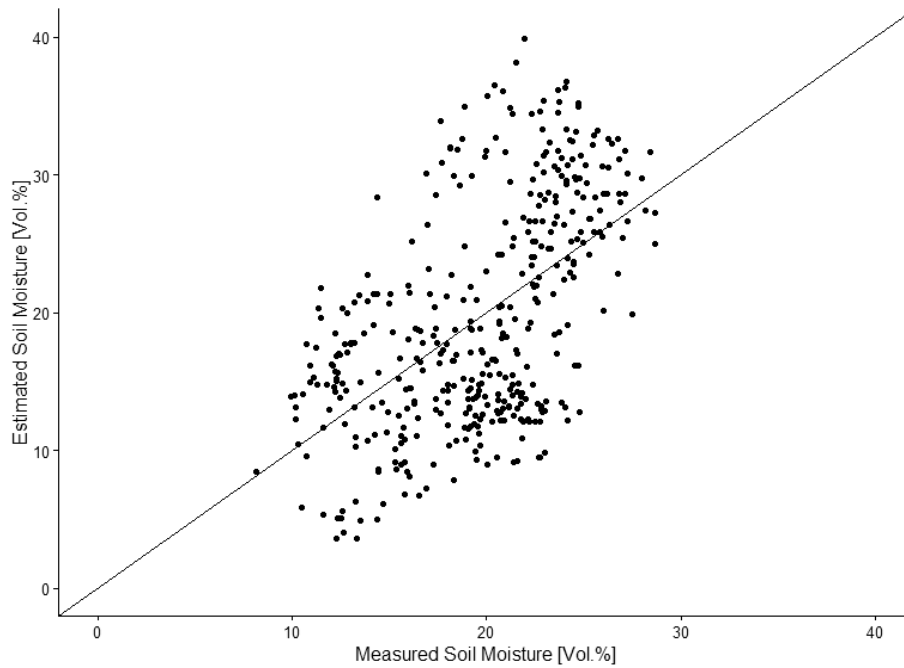


Figure 5.30. Comparison of measured and estimated soil moisture for bare soil [Vol.%]. The solid line is the zero-line.

Table 5.2. Mean *RMSE* for soil moisture retrieval on bare soil using LOOCV, 5- and 10-fold cross validation with 1000 repetitions.

| | LOOCV | 5-fold CV (1000 repetitions) | 10-fold CV (1000 repetitions) |
|--------------------------|-------|------------------------------|-------------------------------|
| Mean <i>RMSE</i> [Vol.%] | 6.7 | 6.7 | 6.7 |

Other studies for empirical C-band SAR soil moisture retrieval resulted in an *RMSE* of around 5% (Loew et al., 2006, Rombach and Mauser, 1997). Paloscia et al. (2013) found an *RMSE* of generally around 4 Vol. % in a precursor study for Sentinel-1 using Radarsat-2 and ENVISAT data over different areas and vegetation types. They used an Artificial Neural Network (ANN) approach and the NDVI to incorporate vegetation information. Whereas VV polarization alone resulted in an *RMSE* of 6 Vol. %, the combination of VV + VH as in the case of Sentinel-1 resulted in an *RMSE* < 2 Vol. %. Mattia et al. (2015) found an *RMSE* of 6 Vol. % using the SMOSAR algorithm with Sentinel-1 data on a wheat farm when averaging to field mean scale. Satalino et al. (2002) found an *RMSE* of 6 Vol. % over smooth bare soils in a critical assessment on soil moisture retrieval capacities from ERS. They concluded that no more than two classes of soil moisture are distinguishable.

Despite the high quality of Sentinel-1 data, the *RMSE* for soil moisture retrieval even under bare soil conditions is as low as with single-channel SAR data from e.g. ERS. This is probably due to the high incidence angle of the S1A acquisitions for our research area. This incidence

angle causes a high sensitivity to roughness and vegetation attenuation effects. Baghdadi et al. (2006) even found an *RMSE* of 9 Vol.% for soil moisture retrieval from bare soil using C-Band ENVISAT data with high incidence angles. Also, the VV polarization, which is the only copol channel that is available from S1A, is regarded inferior to HH polarization for soil moisture studies (Paloscia et al., 2013).

It is well known, that surface roughness has a major influence on the backscatter intensity of bare soil fields. Therefore, to possibly improve soil moisture retrieval we must investigate this effect. Consequently, we compared roughness measurements on bare soil fields to the SAR measures.

At first, rms height and acl were normalized to the centre wavelength of S1A, which is 5.55 cm, as radar effective roughness is wavelength-dependent. As mentioned earlier, roughness measurements have not been performed on the dates of S1A acquisitions but one day up to two weeks later. In general, we assume soil surface roughness to be not as temporarily variable as e.g. soil moisture, but to reduce the effect of this uncertainty, we averaged the radar and roughness measurements to field mean values. Analysis also showed that we must restrict our dataset to bare soil fields with no crop residues, as they have an undefinable influence on the relationship between surface roughness and backscatter. One possible reason for that is the heterogeneous distribution of crop residues on the field. Crop residues are also prone to temporal changes due to wind, animal movement etc., so that with the time-lag between the SAR measurement and the ground measurement with the laser distance device, the two signals decorrelate. As only few roughness measurements were performed, our sample finally reduced to six data points representing field means. They are all from the Selhausen test site and correspond to two different S1A acquisition dates: 2016-11-17 and 2016-09-30 (with roughness measurements performed on 2016-11-30 and 2016-10-11, respectively). For all fields, k_s is below one, apart from SH F06 on 2016-09-30. It shows a mean k_s way above one and showed high deviations when fitting linear regressions to the datasets. The reason is that the field has been freshly ploughed on the date of the roughness measurement and therefore is no longer comparable to the SAR acquisition 11 days earlier. As a S1A acquisition from the same orbit was available for one day after the roughness measurements, we could use this measurement for validation purposes, as we discarded SH F06 / 2016-09-30 from our model calibration dataset. For the other fields that have been measured on 2016-10-11, we kept using the S1A acquisition from 2016-09-30, as we have no soil moisture measurements for the acquisition from 2016-10-12.

While fitting empirical models to predict roughness measures from SAR observables, we found highest correlations of roughness measurements to the Crosspol Ratio and to A . This sensitivity

of Crosspol Ratio and A to surface roughness has also been found by Koyama (2012). For the dual-pol case we must keep in mind, that A has no clear physical meaning and correlates strongly with H and the Crosspol Ratio respectively, as explained in the chapter 5.3.

The five best resulting models for the description of surface roughness are compared in Table 10. Each model was developed on five data points that represent field mean values. Using the three measurement points per field separately, did not result in high correlations.

While all models have high R^2 values, model 1-3 have a p-value < 0.001 (***) whereas model 4 and 5 have a p-value < 0.01 (**). We applied a leave-one-out cross validation as described earlier to calculate an $RMSE$. Next, we used our models to predict k_s and acl respectively for the additional dataset from SH F06 on 2016-10-12. For these predictions, we calculated the $RMSE$. Overall, model 3 performs best for the prediction of k_s (Figure 5.31), as it has a high R^2 value, a low prediction error and shows the lowest $RMSE$ for predicting the additional data point. Furthermore, it is based only on the Crosspol Ratio and does not use A additionally like model 2. Therefore, model 3 is used in the following analysis.

Still, the $RMSE$ is around 23% for the prediction of SH F06 on 2016-10-12, so that predictions for high roughness values (as found on the validation data point) are insecure. Consequently, prediction of roughness on freshly ploughed fields will not perform well. To develop a more robust model, a larger amount of roughness measurements, closer to the date of SAR acquisition is necessary. These measurements should encompass also fields with higher roughness situations, as directly after ploughing.

Table 5.3. Overview of different models to retrieve roughness parameters from SAR observables with adjusted R^2 and the significance (** = p-value < 0.01 , *** = p-value < 0.001).

| Model | Regression | Degree of regression | R^2 | LOOCV RMSE | Prediction of SH F06 2016-10-12 RMSE |
|-------|--------------------------------------|----------------------|---------|------------|--------------------------------------|
| 1 | $acl \sim vh[db] / vv[db]$ | 1 | 0.99*** | 0.16 | 1.74 |
| 2 | $k_s \sim \log_{10}(vh/vv) * 10 * A$ | 1 | 0.77*** | 0.06 | 0.36 |
| 3 | $k_s \sim \log_{10}(vh/vv) * 10$ | 1 | 0.76*** | 0.07 | 0.23 |
| 4 | $k_s \sim A$ | 2 | 0.7** | 0.71 | 0.49 |
| 5 | $acl \sim vh[db] / vv[db]$ | 1 | 0.73** | 0.86 | 3.5 |

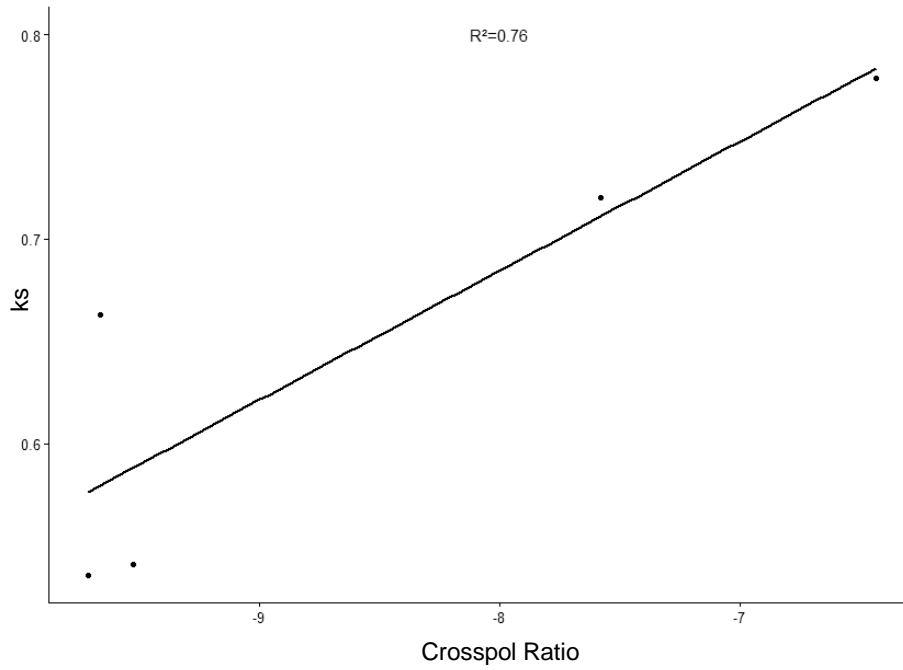


Figure 5.31. Relationship between k_s and the Crosspol Ratio based on field mean values. Each mean value consists of 3 single roughness measurements in the look direction of S1A.

$$k_s = 1.19 + 0.06 \cdot \log_{10} \frac{\gamma_0^{vh}}{\gamma_0^{vv}} \cdot 10 \quad (5.2)$$

As roughness in the form of k_s is linearly correlated with the Crosspol Ratio in dB, as explained by model 3, we can use the Crosspol Ratio directly as a proxy for surface roughness. Nevertheless, adding the Crosspol Ratio as a roughness term to soil moisture retrieval based on γ_{0vv} does not improve the model (adjusted $R^2 = 0.30^{***}$ for bare soil without crop residues and $R^2 = 0.31^{***}$ for all classes of bare soil). This shows, that adding roughness information by using (5.2) cannot improve soil moisture retrieval. To analyse the potential improvement by incorporating roughness data, a bigger data set of roughness measurements, encompassing different roughness conditions is needed.

Consequently, we will use the simple soil moisture retrieval model (5.1) for bare soil, only depending on γ_{0vv} .

5.4.2 The Sugar Beet Model

No significant relationship between soil moisture and backscatter can be derived, independent of which polarization is used or whether additional parameters like e.g. biomass are included in the regression analysis. Therefore, no model can be developed, that allows for soil moisture retrieval under sugar beet. Also restricting the dataset to dates with very small sugar beet plants like on 2015-05-15 and 2016-05-09 did not enable soil moisture retrieval. This is surprising, because the plants are so small on these dates that the soil surface is rather bare and soil moisture

retrieval should be feasible. A possible reason for that could be the sowing process of the field that compressed the soil in a way that its characteristics differ from bare soil fields. Instead, as already indicated by the correlation heat maps, a high linear correlation is found for retrieving canopy height, VWC and biomass from SAR observables. (Figure 5.32) shows the relationship between canopy height and γ_{0vv} . Consequently, the canopy height of sugar beet can be retrieved directly from γ_{0vv} as:

$$\text{canopy height [cm]} = 85.91 + 5.5 \cdot \gamma_{0vv}^{vv}[\text{dB}] \quad (5.3)$$

The regression is highly significant with an adjusted R^2 of 0.54***.

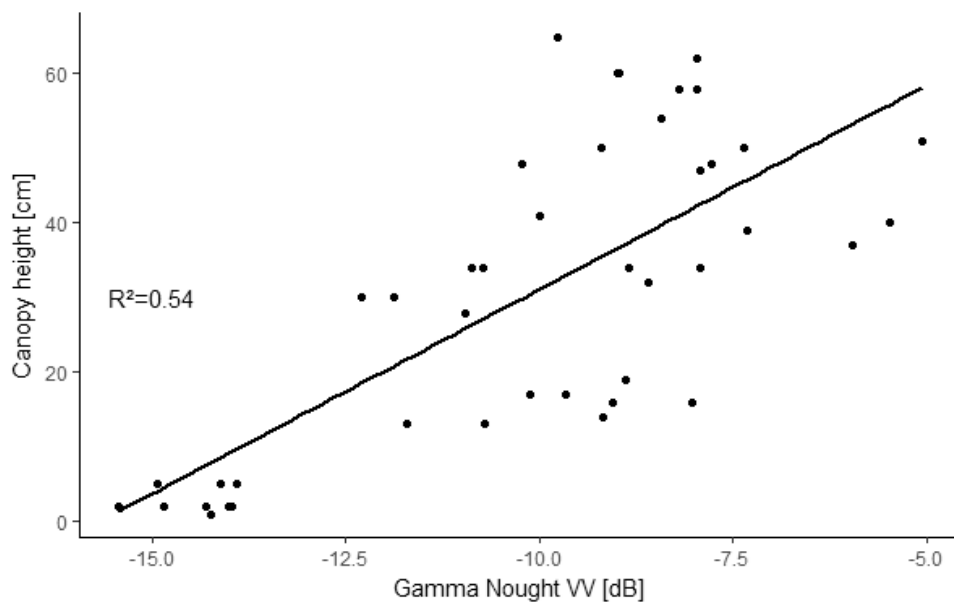


Figure 5.32. Relationship between canopy height [cm] and γ_{0vv} [dB] for sugar beet with linear fit and R^2 .

Using equation (5.3) results in an $RMSE$ of 14.2 cm (Table 5.4). The modelled canopy height is then compared to the measured canopy height in Figure 5.33. It shows that no systematic over- or underestimation occurs, but the deviations from the reference zero line are equally distributed. Still, the $RMSE$ is on a level of about $\frac{1}{4}$ of the range canopy height measurements.

Table 5.4. Mean $RMSE$ for the retrieval of canopy height for sugar beet.

| | LOOCV | 5-fold CV (1000 repetitions) | 10-fold CV (1000 repetitions) |
|------------------|-------|------------------------------|-------------------------------|
| Mean $RMSE$ [cm] | 14.2 | 14.2 | 14.2 |

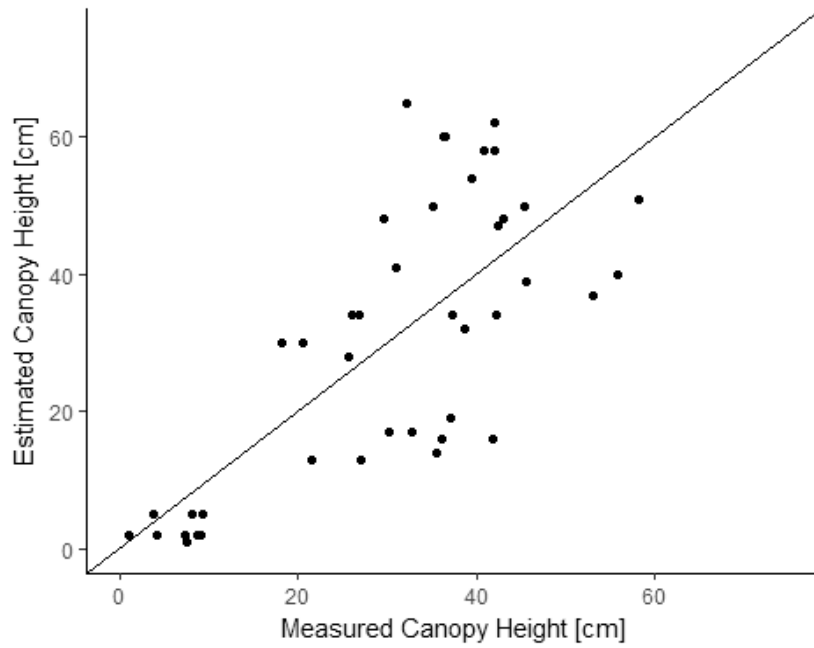


Figure 5.33. Comparison of measured and estimated canopy height for sugar beet with reference zero line.

VWC can be retrieved from our dataset from a combination of VV and VH backscatter as:

$$VWC [Vol. \%] = 103.1 + 1.97 \cdot \gamma_0^{vv} [dB] + 0.12 \cdot \gamma_0^{vh} [dB] \quad (5.4)$$

The relationship has an adjusted R^2 of 0.3***.

Table 5.5. Mean *RMSE* for the retrieval of VWC from sugar beet.

| | LOOCV | 5-fold CV (1000 repetitions) | 10-fold CV (1000 repetitions) |
|--------------------------|-------|------------------------------|-------------------------------|
| Mean <i>RMSE</i> [Vol.%] | 5.7 | 5.7 | 5.7 |

Calculating the VWC and comparing it to measured VWC (Figure 5.34) shows no systematic over- or underestimation but reaches an *RMSE* of 5.7 Vol.% (Table 5.4), which is again within $\frac{1}{4}$ of the value range.

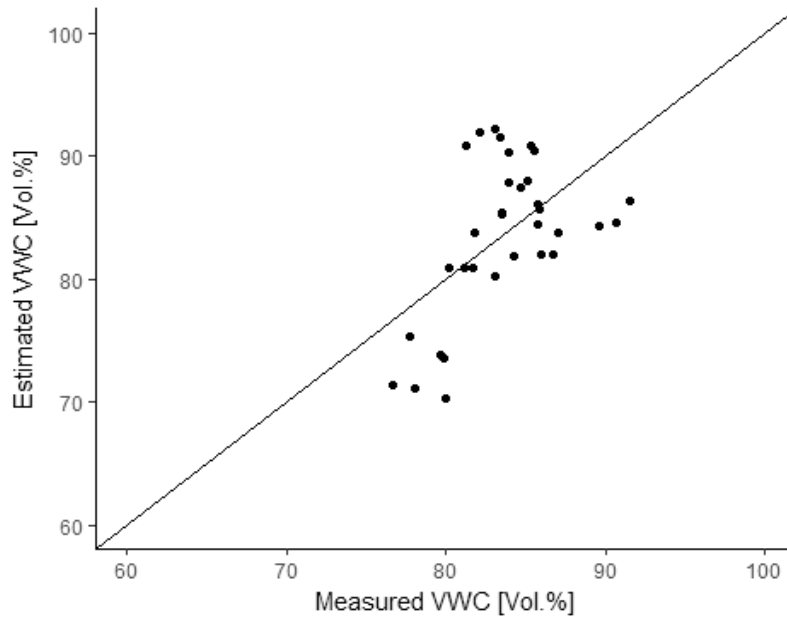


Figure 5.34. Comparison of estimated and measured VWC [Vol.%] for sugar beet.

The total wet biomass can be estimated from our dataset with an adjusted R^2 of 0.3***:

$$Biomass [g/m^2] = 19888 + 595 \cdot \gamma_0^{vv}[dB] + 450 \cdot \gamma_0^{vh}[dB] \quad (5.5)$$

and results in an $RMSE$ of about 5200 – 6500 g (Table 5.6), depending on the validation technique that is used. As the range of measured values is about 11.000 g, the $RMSE$ makes up about $\frac{1}{2}$ of the range. The high $RMSE$ and Figure 5.35 prove, that biomass cannot be predicted with a sufficient accuracy by (5.5). This could be due to the sample taking of sugar beet plants, which are hard to extract from the soil, when they are getting bigger. This can cause plants samples to break into small pieces. Additionally, many leaves fell off the plants and lay loosely on the ground. This can cause over- or underestimations on the real biomass per plant.

Table 5.6. Mean $RMSE$ for the retrieval of sugar beet biomass.

| | LOOCV | 5-fold CV (1000 repetitions) | 10-fold CV (1000 repetitions) |
|---------------------------------|-------|------------------------------|-------------------------------|
| Mean $RMSE$ [g/m ²] | 6574 | 5259 | 5248 |

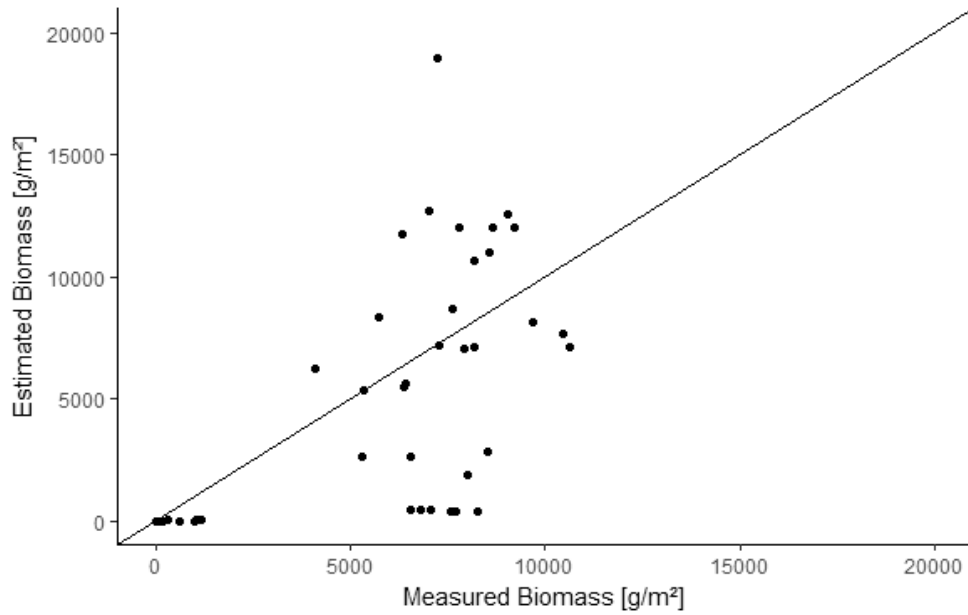


Figure 5.35. Comparison of estimated and measured biomass [g/m²] for sugar beet.

In total, our dataset enables no soil moisture retrieval for sugar beet. But we can retrieve canopy height and VWC instead, with an uncertainty of about 25%.

5.4.3 The Cereal Model

SAR backscatter from cereal fields shows no high sensitivity towards soil moisture, as already indicated in 5.3.3 Therefore no soil moisture retrieval model can be developed. Regarding the vegetation parameters, we found a high sensitivity towards green and brown LAI. This is supported by findings from Prévot et al. (1993) and Brown et al. (2003) who consider LAI as a major parameter influencing the scattering behaviour of incoming microwaves. Despite the biomass amount having an influence on backscatter intensity in all polarizations, this influence cannot be explained by an empirical model. Mattia et al. (2003) found the VV polarization in C-band to be highly sensitive to biomass but this sensitivity was considerably modulated by soil moisture. Therefore, like with our data, the retrieval of biomass or biomass density was not feasible neither using VV nor any other polarization.

The quantitative analysis results in two models describing the green LAI either by γ_{0vv} (Figure 5.36) or by the Crosspol Ratio (Figure 5.37) with an adjusted R^2 of 0.4*** for both models.

$$\text{Green LAI} = -3.8 - 0.4 \cdot \gamma_0^{vv} [dB] \quad (5.6)$$

$$\text{Green LAI} = 5.5 + 0.5 \cdot \frac{\gamma_0^{vh}}{\gamma_0^{vv}} [dB] \quad (5.7)$$

Splitting the data set into winter wheat and winter barley results in better adjusted R^2 values for winter wheat than for winter barley (0.6*** / 0.4***) when calibrating a linear model with the Crosspol Ratio. Why the Crosspol Ratio correlates stronger to green LAI for winter wheat than winter barley is not clear but could be attributed to the generally higher LAI and biomass values of winter barley (Table 4.5) that influence the Crosspol Ratio differently. The analysis of sensitivity in 5.3.3 has shown that winter barley, in contrast to winter wheat, has also a high correlation of biomass density to the Crosspol Ratio. This might influence the relationship between the Crosspol Ratio and green LAI. As the differentiation of winter cereals by remote sensing is not trivial, we prefer to use a comprehensive model for winter cereals.

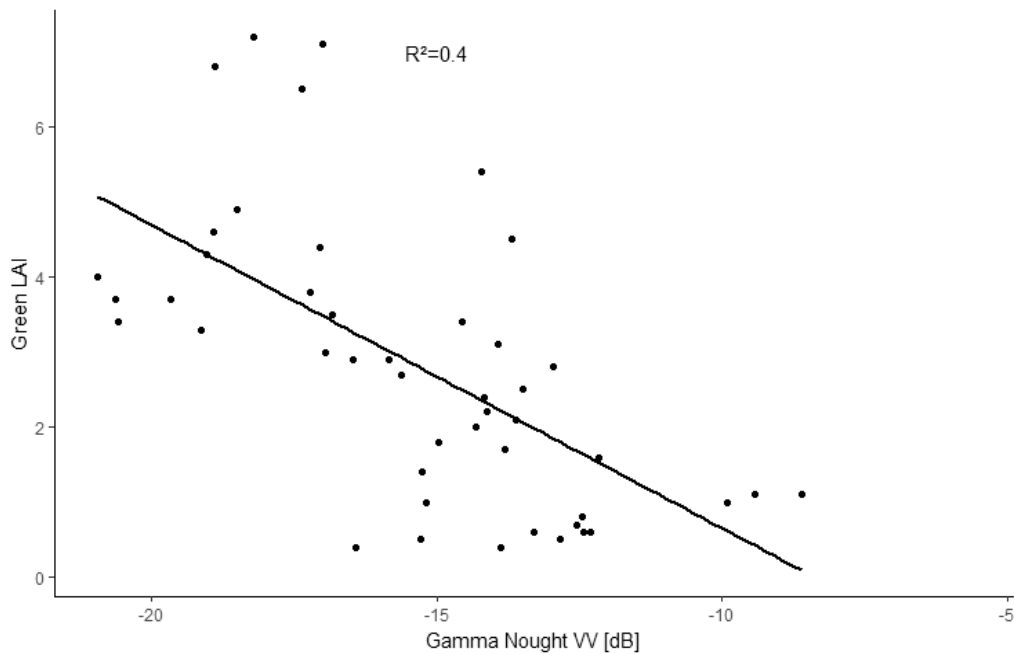


Figure 5.36. Relationship of green LAI and γ_{0vv} for cereals.

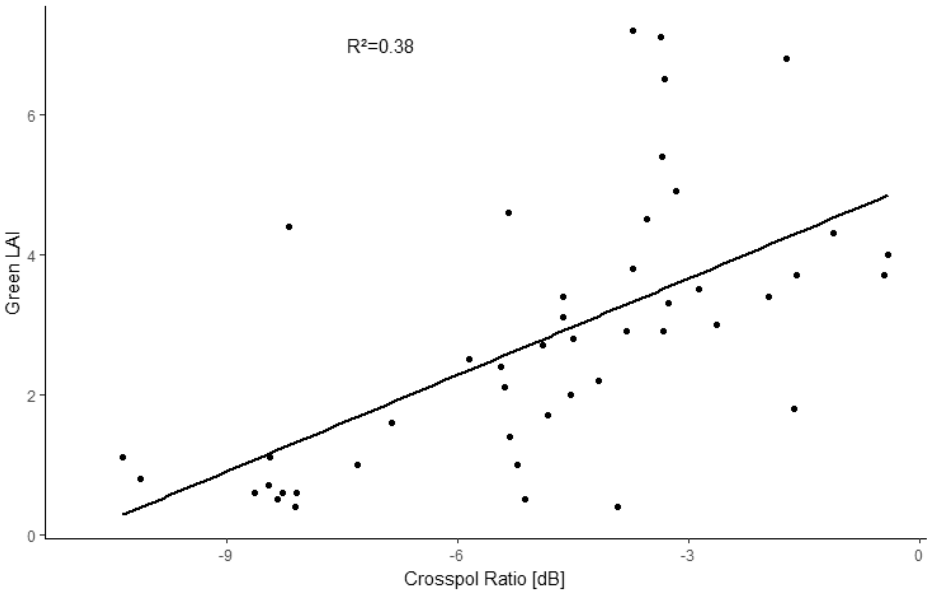


Figure 5.37. Relationship of green LAI and the Crosspol Ratio for cereals.

The quantitative analysis of brown LAI resulted in no significant model. Therefore, it cannot be retrieved from SAR observables. This indicates, that brown leaves have a lower influence on SAR backscatter than green leaves.

Figure 5.38 and Figure 5.39 show the comparison of estimated and measured LAI for the two models (5.6) and (5.7).

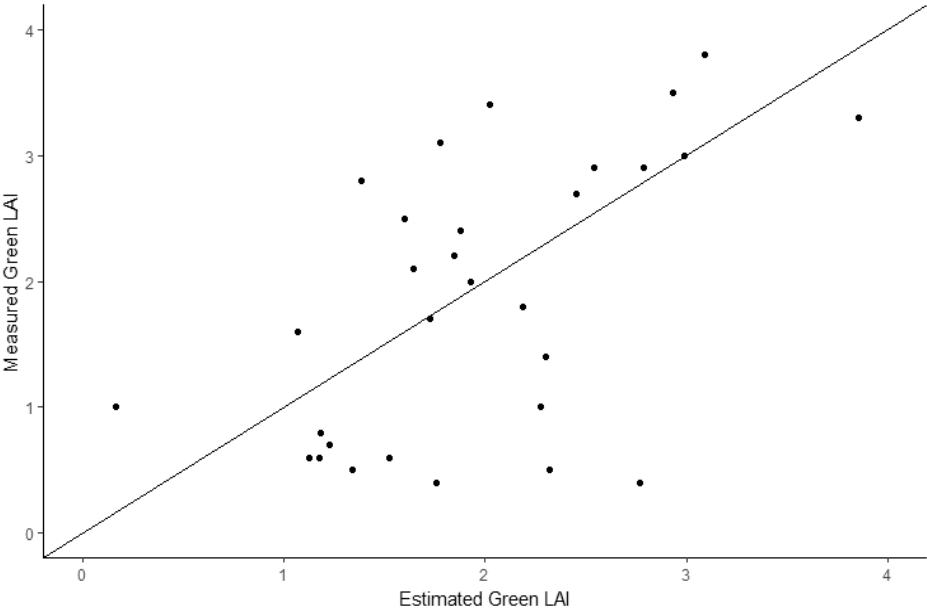


Figure 5.38. Comparison of measured and estimated green LAI for cereals using equation (5.6).

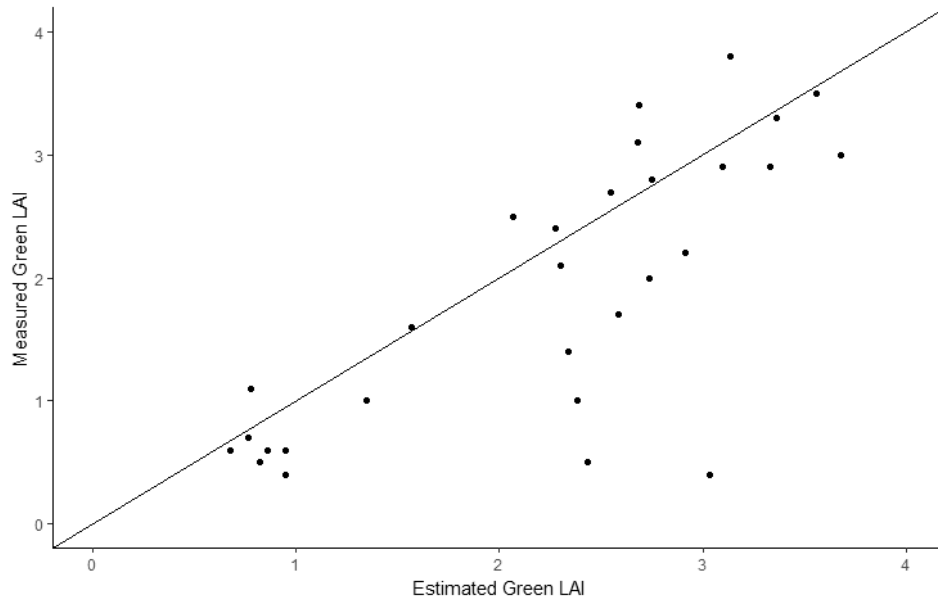


Figure 5.39. Comparison of measured and estimated green LAI for cereals using equation (5.7).

While the first model tends to have an equally distributed error, in the second model more data points are underestimated. Both models can estimate green LAI with an accuracy of about $\frac{1}{4}$ of the LAI range (Table 5.6). This accuracy is comparable to the accuracy found for parameters retrieved in the previous chapters. Retrieving the LAI only from winter wheat and using a linear model based on the Crosspol Ratio would accomplish an *RMSE* of 0.8 but because of the reasons mentioned earlier, we prefer using a combined model for winter cereal LAI retrieval.

Table 5.7. Mean *RMSE* for the retrieval of green LAI for cereals using models 5.6 and 5.7.

| | LOOCV | 5-fold CV (1000 repetitions) | 10-fold CV (1000 repetitions) |
|------------------------|-------|------------------------------|-------------------------------|
| Mean <i>RMSE</i> (5.6) | 1.5 | 1.5 | 1.5 |
| Mean <i>RMSE</i> (5.7) | 1.5 | 1.5 | 1.5 |

5.4.4 The Maize Model

Maize is the only land use type in our study besides bare soil, which shows a high sensitivity towards surface soil moisture. Therefore, it allows for the retrieval of soil moisture by using the following linear model:

$$\text{Soil Moisture}[\text{Vol. \%}] = 67.2 + 4.1 \cdot \gamma_{0VV}[\text{dB}] \quad (5.8)$$

The model is based on a linear regression as shown in Figure 5.40 and reaches *RMSE* values comparable to those of soil moisture retrieval from bare soil (Table 5.7). The model shows no bias, towards over- or underestimation of the measured soil moisture (Figure 5.41).

Table 5.8. Mean *RMSE* for soil moisture retrieval from maize.

| | LOOCV | 5-fold CV (1000 repetitions) | 10-fold CV (1000 repetitions) |
|--------------------------|-------|------------------------------|-------------------------------|
| Mean <i>RMSE</i> [Vol.%] | 6.8 | 6.8 | 6.8 |

Restricting the data set to situations with small vegetation and stubbles does not change the model fit notably and results in a slightly worse adjusted R^2 of 0.4***. Therefore, as already indicated in the analysis of sensitivity, high vegetation cover seems to have no strong influence on γ_{0vv} . The backscatter from the soil surface is rather enhanced by double bounce effects from the high maize stems. These stems are planted in row distances of around 80 cm, which is about six times higher than the row distance of e.g. winter wheat. Therefore, more of the incoming vertically polarized microwaves can reach the ground.

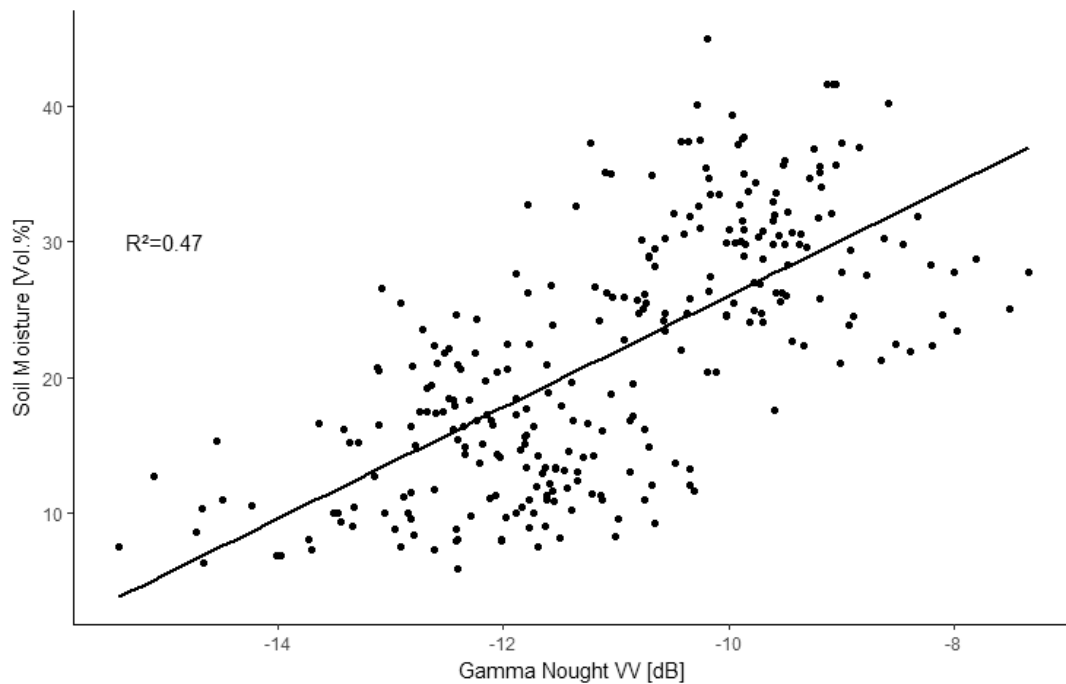


Figure 5.40. Relationship between soil moisture and γ_{0vv} under maize.

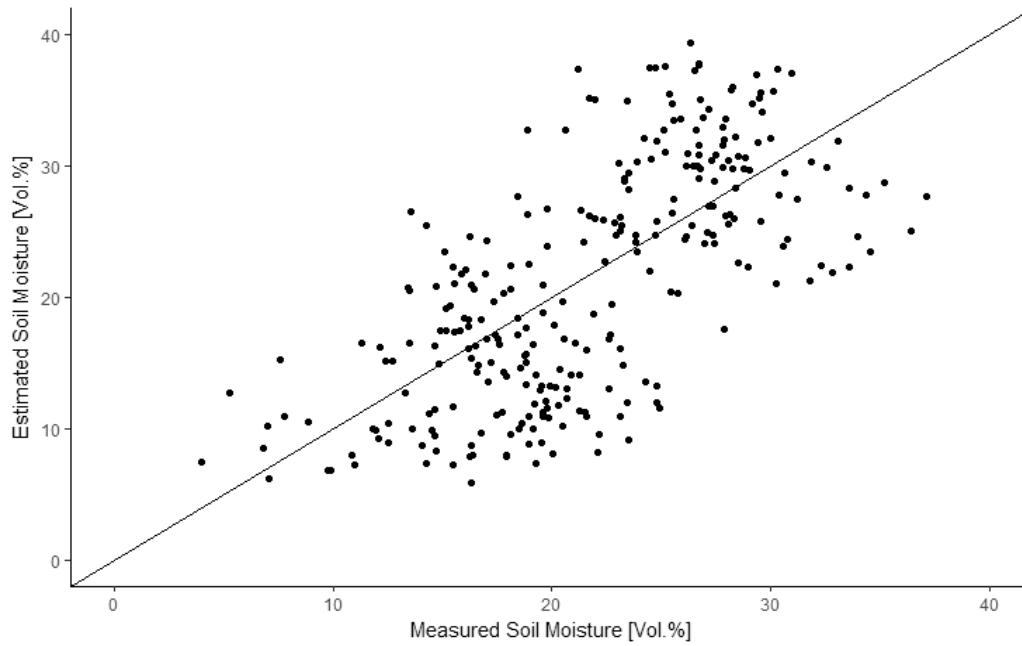


Figure 5.41. Comparison of measured and estimated soil moisture under maize.

In contrast to γ_{0vv} , that is mainly sensitive to soil moisture, γ_{0vh} and the Crosspol Ratio correlate strongly to vegetation parameters. Therefore, a highly significant model to retrieve green LAI from the Crosspol Ratio can be developed as shown in Figure 5.42:

$$Green\ LAI = 7.6 + 0.8 \cdot \frac{\gamma_0^{vh}}{\gamma_0^{vv}} [dB] \quad (5.9)$$

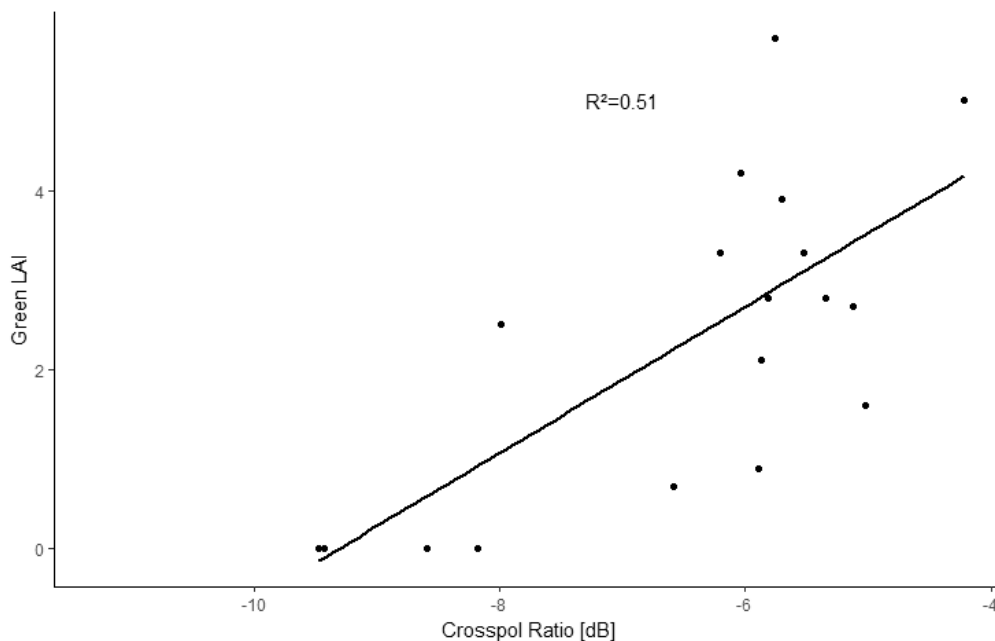


Figure 5.42. Relationship between green LAI and the Crosspol Ratio on maize.

Table 5.9. Mean *RMSE* for LAI retrieval from maize.

| | LOOCV | 5-fold CV (1000 repetitions) | 10-fold CV (1000 repetitions) |
|------------------|-------|------------------------------|-------------------------------|
| Mean <i>RMSE</i> | 1.3 | 1.3 | 1.3 |

The *RMSE* of the LAI estimation is in an order of 1/3 of the range of LAI measurements and therefore slightly worse than for the estimation of the other vegetation parameters (Table 5.8). The comparison of measured and estimated LAI indicates no strong preference towards over- or underestimation (Figure 5.43).

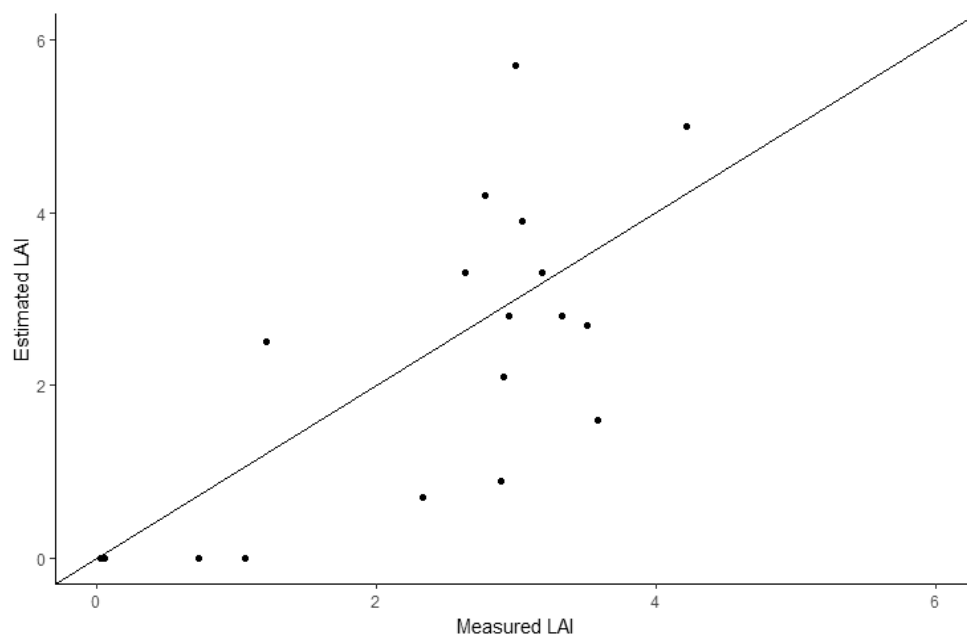


Figure 5.43. Comparison of measured and estimated green LAI for maize.

For the estimation of canopy height, a linear model based on γ_{0vh} can be developed:

$$\text{Canopy Height [cm]} = 776.3 + 37.5 \cdot \gamma_{0vh} \text{ [dB]} \quad (5.10)$$

It is based on the comparison of canopy height and γ_{0vh} as shown in Figure 5.44 and has an adjusted R^2 of 0.7***. The *RMSE* of the relationship is about 53 cm (Table 5.9) and therefore again around 1/4 of the range of the occurring canopy height values.

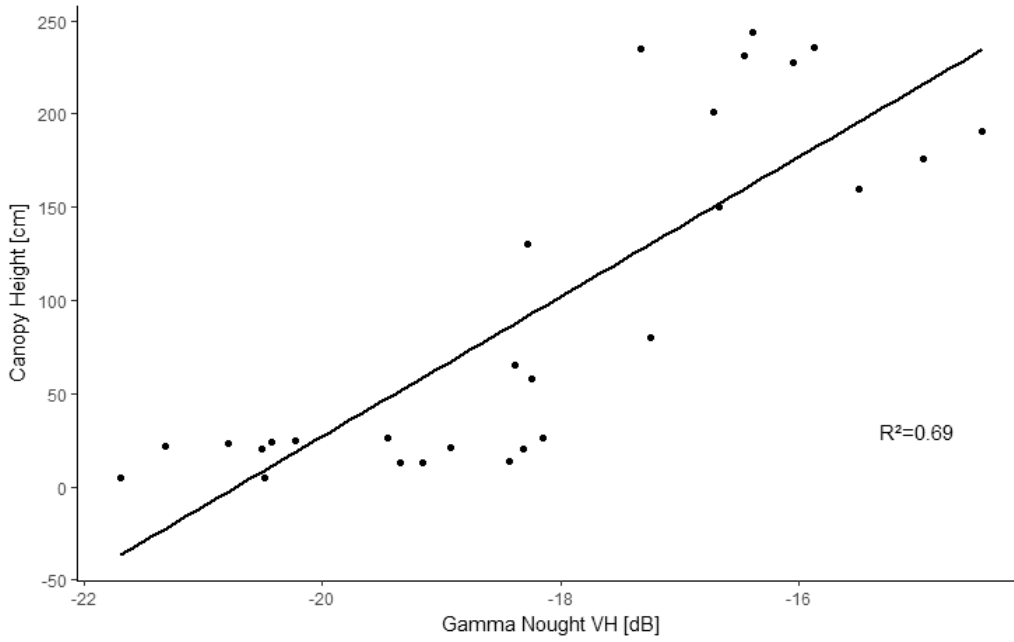


Figure 5.44. Relationship between canopy height and γ_{0vh} for maize.

Table 5.10. Mean *RMSE* for canopy height retrieval from maize.

| | LOOCV | 5-fold CV (1000 repetitions) | 10-fold CV (1000 repetitions) |
|-----------------------|-------|------------------------------|-------------------------------|
| Mean <i>RMSE</i> [cm] | 52.7 | 52.8 | 52.8 |

The comparison of estimated and measured canopy height shows no strong bias towards over- or underestimation (Figure 5.45).

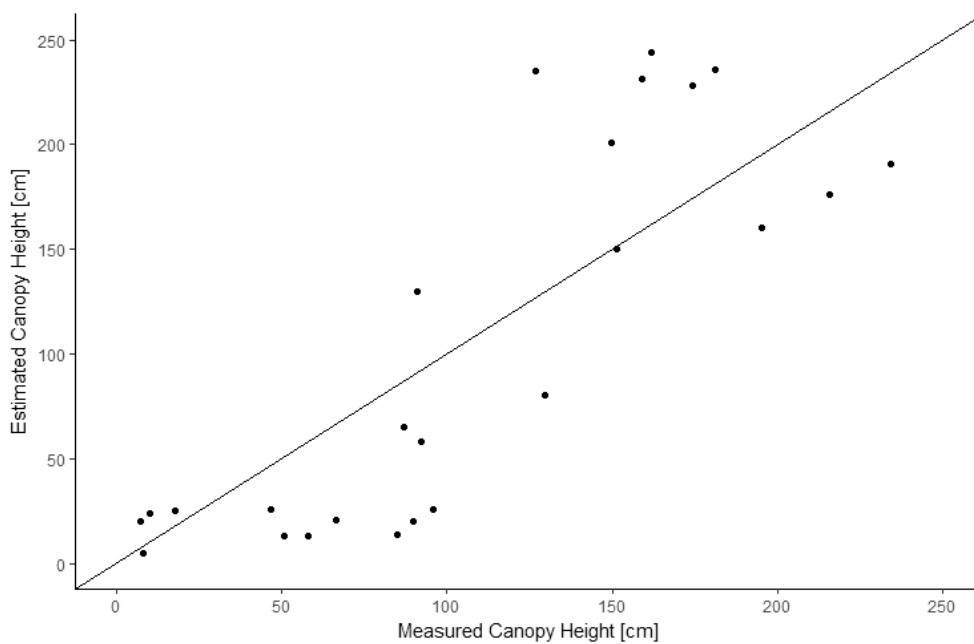


Figure 5.45. Comparison of estimated and measured canopy height for maize.

5.4.5 The Grassland and Triticale Model

As already emerging from the analysis of sensitivity, no simple model can be derived neither from grassland nor from triticale, to describe the relationship between soil moisture or vegetation parameters with SAR observables. We accredit this to the surface structure of grassland vegetation that is not sown in regular rows and to the influence of the thatch layer. For soil moisture retrieval the absence of a row structure means that no bare soil shows through, when the vegetation is dense. The analysis of maize indicated, that even with dense vegetation, soil moisture can be retrieved because of stem-ground interactions and because of the high row distance. Also, the taking of vegetation samples from grassland is more prone to measurement errors, because grassland samples have to be collected using an electric hand mower or scissors. In contrast to crops it is difficult to cut the blade of grass from the soil surface without including soil material in the sample.

While parameter retrieval for triticale might be possible for other locations, it is not possible for our research fields, because here, triticale resembles grassland vegetation and is not sown in rows. Furthermore, the triticale fields in our study were characterized by high amounts of weeds that could have a strong unknown influence on the microwave backscatter.

In general, the problem of soil moisture retrieval on grassland has been discussed by several authors (Martin et al., 1989, Saatchi et al., 1994, Koyama et al., 2010a) who described the high water content of the thatch layer and its complex interactions with the microwaves as the main obstacle. Additionally, Baghdadi et al. (2016) found HH polarization that is not available from our data, superior for soil moisture retrieval under grassland to VV or VH polarization.

5.4.6 Summary Models for Land Surface Parameter Retrieval

The last chapter has shown, that apart from bare soil and maize, soil moisture retrieval on agricultural areas is not possible with C-band SAR from S1A, when the incidence angle is high. This is supported by a study from Alexakis et al. (2017), that found a strong attenuating effect of even sparse vegetation for S1A data with a comparably high incidence angle. The fact that in contrast to the other vegetated land use types, soil moisture retrieval under maize is possible, is surprising as maize accumulates very high amounts of biomass. Nevertheless, Brown et al. (2003) found a high double-bounce component in VV backscatter from maize, resulting in stem-ground interactions that could explain the higher sensitivity of VV to soil moisture under maize and also Joseph et al. (2010) found a high sensitivity of C-band backscatter on soil moisture under maize even at peak biomass and large incidence angles, which they attributed to scattering along the soil-vegetation pathway. For both maize and bare soil, the *RMSE* of soil

moisture retrieval is around 7 Vol.%. This is comparable to former studies of C-Band SAR soil moisture retrieval that resulted in *RMSE* values between 4-9 Vol.% (cf. chapter 5.4.1) depending on the sensor and incidence angle.

The inclusion of roughness information from few measurements did not improve the soil moisture retrieval performance for bare soil. To have a possible improving effect more roughness measurements from different acquisition dates and different roughness states (e.g. freshly ploughed) would be needed. As for most vegetated areas (apart from maize) no sensitivity to soil moisture could be detected and because the amount of available roughness measurements is even lower than for bare soil, the roughness measurements under vegetation were not considered further.

Altogether, maize and sugar beet are the only vegetation types that allow for the retrieval of more than one vegetation parameter. In contrast to that, for cereals, only the retrieval of green LAI is possible. We explain this with the fact that maize is sensitive to soil moisture only in VV polarization but not in VH polarization and for sugar beet we find no strong sensitivity to soil moisture. Consequently, vegetation parameters can be derived without soil moisture interfering in the backscattering process. For cereals, soil moisture effects the backscatter intensity, but this effect cannot be quantified. Therefore, soil moisture disturbs vegetation parameter retrieval for cereals. Predominantly, the *RMSE* for vegetation parameter retrieval is around 25 % of the total value range. Additionally, not all vegetation parameters could be retrieved from all vegetation types. Consequently, dual-pol C-band SAR data with high incidence angle seems to be not perfectly suited for vegetation parameter retrieval.

Grassland and triticale posed an interesting case, as they are the only vegetation type that is not sown in rows and showed as the only vegetation type a course of H that is not identical to the Crosspol Ratio. Nevertheless, neither the retrieval of soil moisture nor that of any vegetation parameter was possible from both grassland and triticale. The reason for that could be the dense vegetation structure of triticale and the vegetation structure and the strongly absorbing thatch layer for grassland.

6 Conclusions and Perspective

The overall aim of this thesis was to improve the extraction of soil moisture and vegetation information from C-band SAR on agricultural fields

- a) to monitor spatial and temporal patterns of soil moisture,
- b) to enable qualitative soil moisture retrieval without ground measurements and
- c) to enable the retrieval of high resolution quantitative soil moisture and vegetation parameters from the newly launched dual-polarimetric Sentinel-1 satellites.

Therefore, the **first scope** of the thesis was to develop a method to derive qualitative soil moisture information in the absence of ground measurements that enables the analysis of historic soil moisture patterns. Here, the following research questions came up:

- i)** Can the qualitative near-surface soil moisture status in the Rur catchment be assessed without in-situ measurements?
- ii)** How can a soil moisture retrieval scheme be validated in the absence of corresponding in-situ measurements of soil moisture?
- iii)** Can near-surface soil moisture patterns in the Rur catchment be found from qualitative data and can their occurrence be explained?

Indeed, the soil moisture index approach is an easily applicable tool for assessing qualitative near surface soil moisture. The only necessary input data is a land use map and a time series of SAR data. Both is available through historic data sets from the ERS satellites. Ground truth data that is needed to train the land use classifications could be substituted by information from aerial images or could be collected by referring to agricultural statistics. This makes a soil moisture index method interesting for historic analysis and the application in data scarce regions.

Due to the lack of ground measurements of soil moisture, the SMI cannot be validated but is rather evaluated by analysing wetting and drying tendencies and comparing the SMI to antecedent precipitation.

Both types of evaluation have shown that the properties of the SMI data are in line with those of in-situ soil moisture:

- The comparison of tandem scenes has shown that moisture changes due to precipitation are well represented in most soil moisture index maps. This makes the soil moisture index a valuable tool to assess moisture tendencies, e.g. for drought monitoring.

- The relationship of the SMI and 7-day antecedent precipitation is comparable to the relationship of in-situ measured soil moisture and corresponding 7-day antecedent precipitation. When averaged, the SMI shows a strong linear correlation with antecedent precipitation. Therefore, it can substitute antecedent precipitation as input to hydrological studies and can be used to derive qualitative information such as soil moisture patterns.

Consequently, the SMI can be used to monitor temporal developments of near surface soil moisture (e.g. for drought monitoring) with a high spatial resolution, give a qualitative idea about surface soil moisture distributions and could outperform antecedent precipitation as a substitute for soil moisture data in hydrological models because it needs no precipitation measurements. The quality of the SMI itself depends of course highly on the accuracy of the underlying land use classification and the extent of the time series of SAR-data.

The analysis of spatial variability of the SMI showed behaviour as described in theory for soil moisture. This indicates that the SMI can be used for the analysis of spatial soil moisture variability without the need of in-situ soil moisture measurements.

Contrary to expectations, the only influence on the soil moisture structure in the Rur catchment is the difference in management and hereby in evapotranspiration between different fields, expressed by the size of homogenous areas. Therefore, qualitative index-based soil moisture information may not be sufficient to identify more complex factors that influence soil moisture patterns, due to its high uncertainty. For such analysis, quantitative soil moisture information from ground measurements or (semi-) empirical remote sensing based soil moisture retrieval methods might be indispensable. Alternatively, an index-based method applied to SAR data with higher spatial, temporal, and radiometric resolution like Sentinel-1 or Radarsat-2 could provide suitable data for pattern analysis. Also, a better land use map, based on a higher number of optical satellite scenes has the potential to improve the quality of an SMI.

The **second scope** of this thesis was to enable retrieval of soil moisture and vegetation parameters from dual-pol C-Band Sentinel-1 data.

Consequently, a method has been presented to process images of VV and VH intensity, the Crosspol Ratio, and the $H2\alpha$ parameters H , A and α from S1A Level-1 SLC data. Regarding the utilization of S1A data for soil moisture and vegetation studies, the following two research questions must be answered:

- iv) Is C-Band SAR data from S1A with high incidence angles suitable for the quantitative estimation of near surface soil moisture under vegetation?

- v) Can semi-empirical algorithms be developed that make the huge open source data archive of Sentinel-1A/B usable for soil moisture and vegetation studies?

As C-band SAR has a short wavelength and therefore a low penetration capacity, the sensitivity of our data to soil moisture and vegetation parameters needed to be assessed first. This was done by using two different methods:

- The utilization of correlation heat maps showed, that only VV-polarized backscatter from bare soil and maize is sensitive to soil moisture. Backscatter from the different vegetation types is sensitive to different vegetation parameters, with maize showing the highest sensitivity to all vegetation parameters in VH polarization. Grassland and triticale, showed no sensitivity to any land surface parameter. The $H2\alpha$ parameters correlate nearly perfectly with each other.
- The analysis of the course of the backscatter signals mainly supports the findings of the correlation analysis. It revealed additionally, that the course of the Crosspol Ratio could identify harvest dates when the general vegetation cycle is known. We also found out, that A and α add no information to the analysis and are therefore redundant. Apart from grassland and triticale, the only vegetation type not sown in rows, the temporal course of H is identical to that of the Crosspol Ratio. Consequently, the course of H relative to the Crosspol Ratio could be used to identify vegetation that is not sown in rows.

The findings from the analysis of sensitivity were used to develop semi-empirical retrieval schemes for soil moisture and vegetation parameters:

- Under bare soil, soil moisture can be retrieved with an error of about 20 % of the value range ($RMSE \sim 7$ Vol. %). Roughness measurements showed a high correlation with SAR observables on a field mean scale. Including roughness information into the soil moisture retrieval scheme did not improve the model, though.
- Sugar beet allows for the retrieval of canopy height and vegetation water content with an error of about 25 % of the range. Fresh biomass can only be derived with an error of about 50 %.
- From cereals we can only derive the green LAI with an error of 25 % of the range.
- Maize allows for the retrieval of soil moisture with an error of about 20 % of the range ($RMSE \sim 7$ Vol. %), of green LAI with an error of around 33 % and of canopy height with an error of 25 %.
- Grassland and triticale do not enable the retrieval of any land surface parameter.

The model development shows, that soil moisture retrieval from Sentinel- 1 data with high incidence angles is only possible on bare soil and maize, because on bare soil no attenuating vegetation cover is present and maize plants have a strong vertical component that enhances the VV polarized backscatter by double bounce effects. Consequently, dual-polarimetric C-band SAR with high incidence angles is not optimal to study soil moisture under vegetation.

Because the SMI method was successful in deriving soil moisture using C-band as well (although deriving only qualitative information), we assume the high incidence angle to be the limiting factor in the S1A study and not necessarily the wavelength. In contrast to the S1A data, the ERS data for the SMI study had a much lower incidence angle. Hence, for soil moisture studies, data with high incidence angles should be favoured to reduce the vegetation influence.

For the quantitative retrieval of vegetation parameters, C-band SAR is not the optimal wavelength, because the sensitivity study and the model development showed that soil moisture very well modulates the different SAR observables, although we were not able to quantify this effect. A high incidence angle should generally be preferred for vegetation studies, as the microwaves pass through a higher fraction of vegetation before reaching the ground.

Consequently, SAR-data with shorter wavelengths like e.g. X-band and high incidence angles, should be favoured for vegetation studies, to minimize the effect of soil moisture. X-band is more affected by clouds and precipitation than longer wavelengths, though.

For the study of soil moisture, L-band SAR in general will be better suited as it is less influenced by vegetation and roughness and has a higher penetration capacity. However, low-frequency bands like L- or P-band are more prone to degradation of the signal by radio frequency interference (RFI) and the Faraday rotation in the ionosphere, which modifies polarization and phase. In that sense, C-band is a good compromise because it is less affected by external influences. Additionally continuity is important for scientific long-time applications and ESA as well as the Canadian Space Agency have a long history of C-band SAR. This makes C-band a reasonable choice for land surface studies.

In contrast to single-channel SAR, the dual-pol data from S1A enabled the differentiation of scattering contributions, especially for maize, where the VV polarization was only sensitive to soil moisture and the VH polarization to vegetation parameters. Therefore multi-polarimetric SAR systems are superior for land surface studies. Except for the effect from grassland and triticale on H , the $H2\alpha$ parameters can easily be substituted by the Crosspol Ratio. This can reduce the processing requirements, as no $H2\alpha$ decomposition must be performed. How far the

parameters of the full-pol H/α decomposition for C-band SAR can improve the empirical retrieval of soil moisture and vegetation parameters, must be assessed more in detail, e.g. employing Radarsat-2 data. Also the influence of surface roughness should be researched in more detail, with a higher number of measurement points on several dates and including different roughness conditions like freshly ploughed soil.

In summary, this thesis contributed to assessing the potential of C-Band SAR for soil moisture and vegetation studies. It showed that a simple time-series based approach can assess soil moisture tendencies and its spatial variability with high resolution in the absence of ground measurements. It stressed the incidence angle as an important limiting factor in soil moisture studies, and showed that C-band SAR is not optimal to quantitatively retrieve vegetation parameters. It also revealed the importance of dual-polarimetric data to distinguish the backscattering contributions e.g. for maize. The $H2\alpha$ decomposition seems to be redundant when the Crosspol Ratio is calculated.

Future work to assess the C-band potential should concentrate on C-band data with higher incidence angles, e.g. from other sensors or from other orbits / research areas and put more emphasis on field measurements of surface roughness. It is also interesting to assess how full-polarimetric C-band data e.g. from Radarsat-2 can enhance the retrieval of land surface parameters, how S1A data can possibly be used to downscale existing passive soil moisture products with coarse resolution and how pattern analysis using the SMI performs, when applied to data with higher spatial resolution.

7 References

- ALEXAKIS, D., MEXIS, F.-D., VOZINAKI, A.-E., DALIAKOPOULOS, I. & TSANIS, I. 2017. Soil Moisture Content Estimation Based on Sentinel-1 and Auxiliary Earth Observation Products. A Hydrological Approach. *Sensors*, 17, 1455.
- ALI, S., GHOSH, N. C. & SINGH, R. 2010. Rainfall–runoff simulation using a normalized antecedent precipitation index. *Hydrological Sciences Journal*, 55, 266-274.
- ÁLVAREZ-MOZOS, J., CASALÍ, J., GONZÁLEZ-AUDÍCANA, M. & VERHOEST, N. E. C. 2005. Correlation between Ground Measured Soil Moisture and RADARSAT-1 derived Backscattering Coefficient over an Agricultural Catchment of Navarre (North of Spain). *Biosystems Engineering*, 92, 119-133.
- ARGENTI, F., LAPINI, A., BIANCHI, T. & ALPARONE, L. 2013. A Tutorial on Speckle Reduction in Synthetic Aperture Radar Images. *IEEE Geoscience and Remote Sensing Magazine*, 1, 6-35.
- ATTEMA, E. P. W. & ULABY, F. T. 1978. Vegetation modeled as a water cloud. *Radio Science*, 13, 357-364.
- ATWOOD, D. K., SMALL, D., GENS, R. 2012. Improving PolSAR Land Cover Classification With Radiometric Correction of the Coherency Matrix. *IEEE Journal of Selected Topics in Applied Earth Observations and Remote Sensing*, 5.
- BAGHDADI, N., GHERBOUDJ, I., ZRIBI, M., SAHEBI, M., KING, C. & BONN, F. 2004. Semi-empirical calibration of the IEM backscattering model using radar images and moisture and roughness field measurements. *International Journal of Remote Sensing*, 25, 3593-3623.
- BAGHDADI, N., HOLAH, N. & ZRIBI, M. 2006. Soil moisture estimation using multi-incidence and multi-polarization ASAR data. *International Journal of Remote Sensing*, 27, 1907-1920.
- BAGHDADI, N. N., HAJJ, M. E., ZRIBI, M. & FAYAD, I. 2016. Coupling SAR C-Band and Optical Data for Soil Moisture and Leaf Area Index Retrieval Over Irrigated Grasslands. *IEEE Journal of Selected Topics in Applied Earth Observations and Remote Sensing*, 9, 1229-1243.
- BALENZANO, A., SATALINO, G., LOVERGINE, F., RINALDI, M., IACOBELLIS, V., MASTRONARDI, N. & MATTIA, F. 2013. On the use of temporal series of L-and X-band SAR data for soil moisture retrieval. Capitanata plain case study. *European Journal of Remote Sensing*, 46, 721-737.
- BECKMANN, P. & SPIZZICHINO, A. 1987. *The Scattering of Electromagnetic Waves from Rough Surfaces*, Artech House.
- BELL, K. R., BLANCHARD, B. J., SCHMUGGE, T. J. & WITCZAK, M. W. 1980. Analysis of Surface Moisture Variations Within Large-Field Sites. *Water Resources Research*, 16, 796-810.
- BENNACEUR, L., BOUSSEMA, M. R. & BELHADJ, Z. Retrieval of multi-scale roughness parameters and soil moisture by numerical inversion. IGARSS 2003. 2003 IEEE International Geoscience and Remote Sensing Symposium. Proceedings (IEEE Cat. No.03CH37477), 21-25 July 2003 2003. 3836-3838 vol.6.
- BÉRIAUX, E., WALDNER, F., COLLIENNE, F., BOGAERT, P. & DEFOURNY, P. 2015. Maize Leaf Area Index Retrieval from Synthetic Quad Pol SAR Time Series Using the Water Cloud Model. *Remote Sensing*, 7, 15818.
- BINDLISH, R. 2001. Parameterization of vegetation backscatter in radar-based, soil moisture estimation. *Remote sensing of environment*, v. 76, pp. 130-137-2001 v.76 no.1.
- BLAES, X., DEFOURNY, P., WEGMULLER, U., VECCHIA, A. D., GUERRIERO, L. & FERRAZZOLI, P. 2006. C-band polarimetric indexes for maize monitoring based on a validated radiative transfer model. *IEEE Transactions on Geoscience and Remote Sensing*, 44, 791-800.
- BLUME, H. P., BRÜMMER, G. W., SCHEFFER, F., HORN, R., KANDELER, E., SCHACHTSCHABEL, P., KÖGEL-KNABNER, I., WELP, G., KRETZSCHMAR, R. & THIELE-BRUHN, S. 2009a. *Scheffer/Schachtschabel: Lehrbuch der Bodenkunde*, Spektrum Akademischer Verlag.
- BLUME, T., ZEHE, E. & BRONSTERT, A. 2009b. Use of soil moisture dynamics and patterns at different spatio-temporal scales for the investigation of subsurface flow processes. *Hydrology and Earth System Sciences*, 13, 1215-1233.
- BOGENA, H., HERBST, M., HAKE, J.-F., KUNKEL, R., MONTZKA, R., PÜTZ, T., VERECKEN, H. & WENDLAND, F. 2005. MOSYRUR - Water balance analysis in the Rur basin. Jülich.

- BOISVERT, J. B., GWYN, Q. H. J., BRISCO, B., MAJOR, D. J. & BROWN, R. J. 1995. Evaluation of Soil Moisture Estimation Techniques and Microwave Penetration Depth for Radar Applications. *Canadian Journal of Remote Sensing*, 21, 110-123.
- BROWN, S. C. M., QUEGAN, S., MORRISON, K., BENNETT, J. C. & COOKMARTIN, G. 2003. High-resolution measurements of scattering in wheat canopies-implications for crop parameter retrieval. *IEEE Transactions on Geoscience and Remote Sensing*, 41, 1602-1610.
- BRUCKLER, L., WITONO, H. & STENGEL, P. 1988. Near surface soil moisture estimation from microwave measurements. *Remote Sensing of Environment*, 26, 101-121.
- BRUNOTTE, E., IMMENDORF, R. & SCHLIMM, R. 1994. *Die Naturlandschaft und ihre Umgestaltung durch den Menschen: Erläuterungen zur Hochschulkursionskarte Köln und Umgebung*, Selbstverlag Geographisches Institut der Universität zu Köln.
- BRYANT, R., MORAN, M. S., THOMA, D. P., COLLINS, C. D. H., SKIRVIN, S., RAHMAN, M., SLOCUM, K., STARKS, P., BOSCH, D. & DUGO, M. P. G. 2007. Measuring Surface Roughness Height to Parameterize Radar Backscatter Models for Retrieval of Surface Soil Moisture. *IEEE Geoscience and Remote Sensing Letters*, 4, 137-141.
- CAMPBELL, J. B. 2002. *Introduction to Remote Sensing*, Taylor & Francis.
- CHEN, X. & HU, Q. 2004. Groundwater influences on soil moisture and surface evaporation. *Journal of Hydrology*, 297, 285-300.
- CHOUDHURY, B. J. & GOLUS, R. E. 1987. Estimating soil wetness using satellite data. *International Journal of Remote Sensing*, 9, 1251-1257.
- CHOUDHURY, B. J., OWE, M., GOWARD, S. N., GOLUS, R. E., ORMSBY, J. P., CHANG, A. T. C. & WANG, J. R. 1986. Quantifying spatial and temporal variabilities of microwave brightness temperature over the U.S. Southern Great Plains. *International Journal of Remote Sensing*, 8, 177-191.
- CLOUDE, S. R. 1985. Target decomposition theorems in radar scattering. *Electronics Letters*, 21, 22-24.
- CLOUDE, S. R. Eigenvalue parameters for surface roughness studies. 1999. 2-13.
- CLOUDE, S. R. 2007. The Dual Polarisation Entropy/Alpha Decomposition: A PALSAR Case Study. 3rd International Workshop on Science and Applications of SAR Polarimetry and Polarimetric Interferometry, 2007 Noordwijk, Netherlands. European Space Agency.
- CLOUDE, S. R., POTTIER, E. 1996. A Review of Target Decomposition Theorems in Radar Polarimetry. *IEEE Transactions on Geoscience and Remote Sensing*, 34, 20.
- CLOUDE, S. R., POTTIER, E. 1997. An entropy based classification scheme for land applications of polarimetric SAR. *IEEE Transactions Geosc. Remote Sens.*, 35, 10.
- COGNARD, A. L., LOUMAGNE, C., NORMAND, M., OLIVIER, P., OTTLE, C., VIDALMADJAR, D., LOUAHALA, S. & VIDAL, A. 1995. Evaluation of the Ers-1 Synthetic Aperture Radar Capacity to Estimate Surface Soil-Moisture - 2-Year Results Over the Naizin Watershed. *Water Resources Research*, 31, 975-982.
- COSGRIFF, R. L., PEAKE, W. H. & TAYLOR, R. C. 1960. *Terrain scattering properties for sensor system design : terrain handbook 2*, Columbus, Ohio State University.
- CROW, W. T. & ZHAN, X. W. 2007. Continental-scale evaluation of remotely sensed soil moisture products. *IEEE Geoscience and Remote Sensing Letters*, 4, 451-455.
- DAVIDSON, M. W. J., MATTIA, F., SATALINO, G., VERHOEST, N. E. C., TOAN, T. L., BORGEAUD, M., LOUIS, J. M. B. & ATTEMA, E. 2003. Joint statistical properties of RMS height and correlation length derived from multisite 1-m roughness measurements. *IEEE Transactions on Geoscience and Remote Sensing*, 41, 1651-1658.
- DAVIDSON, M. W. J., THUY LE, T., MATTIA, F., SATALINO, G., MANNINEN, T. & BORGEAUD, M. 2000. On the characterization of agricultural soil roughness for radar remote sensing studies. *IEEE Transactions on Geoscience and Remote Sensing*, 38, 630-640.
- DUBOIS, P. C., ZYL, J. V. & ENGMAN, T. 1995. Measuring soil moisture with imaging radars. *IEEE Transactions on Geoscience and Remote Sensing*, 33, 915-926.
- DWD CLIMATE DATA CENTER (CDC) Historical daily precipitation observations for Germany, version v005, 2017. v005 ed.
- EL HAJJ, M., BAGHDADI, N., ZRIBI, M. & ANGELLIAUME, S. 2016. Analysis of Sentinel-1 Radiometric Stability and Quality for Land Surface Applications. *Remote Sensing*, 8, 406.

- ENGMAN, E. T. 1991. Applications of Microwave Remote-Sensing of Soil-Moisture for Water-Resources and Agriculture. *Remote Sensing of Environment*, 35, 213-226.
- ENTEKHABI, D., RODRIGUEZ-ITURBE, I. & CASTELLI, F. 1996. Mutual interaction of soil moisture state and atmospheric processes. *Journal of Hydrology*, 184, 3-17.
- ESA 2017. SNAP - ESA Sentinel Application Platform, <http://step.esa.int>. v5.05 ed.
- ESA, E. S. A. 2015. Sentinel-1A TOPS Radiometric Calibration Refinement.
- FAMIGLIETTI, J., DEVEREAUX, J. S., LAYMON, C. A., TSEGAYE, T., HOUSER, P. R., JACKSON, T. J., GRAHAM, S. T., RODELL, M. & VAN OEVELEN, P. J. 1999. Ground-based investigations of soil-moisture variability within remote sensing footprints during the Southern Great Plains 1997 (SGP97) Hydrology Experiment. *Water Resources Research*, 35, 1938-1951.
- FAMIGLIETTI, J., RUDNICKI, J. & RODELL, M. 1998. Variability in surface moisture content along a hill slope transect: Rattlesnake Hill, Texas. *Journal of Hydrology*, 210, 259-281.
- FANG, B., LAKSHMI, V., BINDLISH, R., JACKSON, T. J., COSH, M. & BASARA, J. 2013. Passive Microwave Soil Moisture Downscaling Using Vegetation Index and Skin Surface Temperature. *Vadose Zone Journal*, 12.
- FREEMAN, A. & DURDEN, S. L. 1998. A three-component scattering model for polarimetric SAR data. *IEEE Transactions on Geoscience and Remote Sensing*, 36, 963-973.
- FROST, V. S., STILES, J. A., SHANMUGAN, K. S. & HOLTZMAN, J. C. 1982. A Model for Radar Images and Its Application to Adaptive Digital Filtering of Multiplicative Noise. *IEEE Transactions on Pattern Analysis and Machine Intelligence*, PAMI-4, 157-166.
- FUNG, A. K. 1994. *Microwave Scattering and Emission Models and Their Applications*, Artech House.
- FUNG, A. K., LI, Z. Q. & CHEN, K. S. 1992. Backscattering from A Randomly Rough Dielectric Surface. *IEEE Transactions on Geoscience and Remote Sensing*, 30, 356-369.
- GARRIGUES, S., ALLARD, D., BARET, F. & WEISS, M. 2006. Quantifying spatial heterogeneity at the landscape scale using variogram models. *Remote Sensing of Environment*, 103, 81-96.
- GEOLOGISCHER DIENST NRW 2016. *Geologie und Boden in Nordrhein Westfalen*, Krefeld, Geologischer Dienst NRW.
- HÄCKEL, H. 2016. *Meteorologie*, UTB GmbH.
- HAJNSEK, I., JAGDHUBER, T., SCHCON, H. & PAPATHANASSIOU, K. P. 2009. Potential of Estimating Soil Moisture Under Vegetation Cover by Means of PolSAR. *IEEE Transactions on Geoscience and Remote Sensing*, 47, 442-454.
- HAJNSEK, I., POTTIER, E. & CLOUDE, S. R. 2003. Inversion of surface parameters from polarimetric SAR. *IEEE Transactions on Geoscience and Remote Sensing*, 41, 727-744.
- HALLIDAY, D., RESNICK, R., WALKER, J. & KOCH, S. W. 2008. *Halliday Physik*, Wiley.
- HECHT, E. 2014. *Optics*, Pearson.
- HEINE, I., JAGDHUBER, T. & ITZEROTT, S. 2016. Classification and Monitoring of Reed Belts Using Dual-Polarimetric TerraSAR-X Time Series. *Remote Sensing*, 8, 552.
- HOLM, W. A., BARNES, R.M. . On radar polarization mixed state decomposition theorems. USA National Radar Conference, 1988 Michigan.
- HUBER, P. J. 2011. Robust Statistics. In: LOVRIC, M. (ed.) *International Encyclopedia of Statistical Science*. Berlin, Heidelberg: Springer Berlin Heidelberg.
- JACKSON, T. J., SCHMUGGE, J. & ENGMAN, E. T. 1996. Remote sensing applications to hydrology: Soil moisture. *Hydrological Sciences Journal-Journal des Sciences Hydrologiques*, 41, 517-530.
- JAGDHUBER, T., HAJNSEK, I., CAPUTO, M. & PAPATHANASSIOU, K. P. Dual-Polarimetry for Soil Moisture Inversion at X-Band. EUSAR 2014; 10th European Conference on Synthetic Aperture Radar, 3-5 June 2014 2014a. 1-4.
- JAGDHUBER, T., HAJNSEK, I. & PAPATHANASSIOU, K. P. Polarimetric soil moisture retrieval using an iterative generalized hybrid decomposition technique. 2014 IEEE Geoscience and Remote Sensing Symposium, 13-18 July 2014 2014b. 53-56.
- JAGDHUBER, T., HAJNSEK, I. & PAPATHANASSIOU, K. P. 2015. An Iterative Generalized Hybrid Decomposition for Soil Moisture Retrieval Under Vegetation Cover Using Fully Polarimetric SAR. *IEEE Journal of Selected Topics in Applied Earth Observations and Remote Sensing*, 8, 3911-3922.

- JAGDHUBER, T., HAINSEK, I., PAPATHANASSIOU, K. P. & BRONSTERT, A. Soil moisture retrieval under agricultural vegetation using fully polarimetric SAR. 2012 IEEE International Geoscience and Remote Sensing Symposium, 22-27 July 2012 2012. 1481-1484.
- JENSEN, J. R. 2007. *Remote Sensing of the Environment: An Earth Resource Perspective*, Pearson Prentice Hall.
- Jl, K. & WU, Y. 2015. Scattering Mechanism Extraction by a Modified Cloude-Pottier Decomposition for Dual Polarization SAR. *Remote Sensing*, 7, 7447.
- JOSEPH, A. T., VAN DER VELDE, R., O'NEILL, P. E., LANG, R. & GISH, T. 2010. Effects of corn on C- and L-band radar backscatter: A correction method for soil moisture retrieval. *Remote Sensing of Environment*, 114, 2417-2430.
- KORRES, W., KOYAMA, C. N., FIENER, P. & SCHNEIDER, K. 2010. Analysis of surface soil moisture patterns in agricultural landscapes using Empirical Orthogonal Functions. *Hydrology and Earth System Sciences*, 14, 751-764.
- KORRES, W., REICHENAU, T. G., FIENER, P., KOYAMA, C. N., BOGENA, H. R., CORNELISSEN, T., BAATZ, R., HERBST, M., DIEKKRÜGER, B., VEREECKEN, H. & SCHNEIDER, K. 2015. Spatio-temporal soil moisture patterns – A meta-analysis using plot to catchment scale data. *Journal of Hydrology*, 520, 326-341.
- KOTTEK, M., GRIESER, J., BECK, C., RUDOLF, B. & RUBEL, F. 2006. *World Map of the Köppen-Geiger Climate Classification Updated*.
- KOYAMA, C. N. 2012. *Quantitative Estimation of Surface Soil Moisture in Agricultural Landscapes using Spaceborne Synthetic Aperture Radar Imaging at Different Frequencies and Polarizations*. Dr.rer.nat, Universität zu Köln.
- KOYAMA, C. N., KORRES, W., FIENER, P. & SCHNEIDER, K. 2010a. Variability of Surface Soil Moisture Observed from Multitemporal C-Band Synthetic Aperture Radar and Field Data. *Vadose Zone Journal*, 9, 1014-1024.
- KOYAMA, C. N., KORRES, W., FIENER, P. & SCHNEIDER, K. 2010b. Variability of Surface Soil Moisture Observed from Multitemporal C-Band Synthetic Aperture Radar and Field Data. *Vadose Zone Journal*, 9, 1014-1024.
- KOYAMA, C. N. & SCHNEIDER, K. 2010. A novel approach to estimate soil moisture under vegetation using partial polarimetric ALOS PALSAR data. ISPRS Commission VIII Symposium 2010, 2010 Kyoto, Japan. 422-426.
- KROGAGER, E. 1990. New decomposition of the radar target scattering matrix. *Electronics Letters*, 26, 1525-1527.
- KUAN, D. T., SAWCHUK, A. A., STRAND, T. C. & CHAVEL, P. 1985. Adaptive Noise Smoothing Filter for Images with Signal-Dependent Noise. *IEEE Transactions on Pattern Analysis and Machine Intelligence*, PAMI-7, 165-177.
- KUTÍLEK, M. & NIELSEN, D. R. 1994. *Soil hydrology*, Catena Verlag.
- LAKSHMI, V. 2013. Remote Sensing of Soil Moisture. *ISRN Soil Science*, 2013, 33.
- LE HEGARAT-MASCLE, S., ZRIBI, M., ALEM, F., WEISSE, A. & LOUMAGNE, C. 2002. Soil moisture estimation from ERS/SAR data: Toward an operational methodology. *IEEE Transactions on Geoscience and Remote Sensing*, 40, 2647-2658.
- LEE, J.-S. 1981. Speckle analysis and smoothing of synthetic aperture radar images. *Computer Graphics and Image Processing*, 17, 24-32.
- LEE, J.-S. 1983. Digital image smoothing and the sigma filter. *Computer Vision, Graphics, and Image Processing*, 24, 255-269.
- LEE, J. S., AINSWORTH, T. L., WANG, Y. & CHEN, K. S. 2015. Polarimetric SAR Speckle Filtering and the Extended Sigma Filter. *IEEE Transactions on Geoscience and Remote Sensing*, 53, 1150-1160.
- LEE, J. S. & POTTIER, E. 2009. *Polarimetric Radar Imaging - From Basics to Applications*, Boca Raton, CRC Press Taylor & Francis Group.
- LEE, J. S., WEN, J. H., AINSWORTH, T. L., CHEN, K. S. & CHEN, A. J. 2009. Improved Sigma Filter for Speckle Filtering of SAR Imagery. *IEEE Transactions on Geoscience and Remote Sensing*, 47, 202-213.

- LEYS, C., LEY, C., KLEIN, O., BERNARD, P. & LICATA, L. 2013. Detecting outliers: Do not use standard deviation around the mean, use absolute deviation around the median. *Journal of Experimental Social Psychology*, 49, 764-766.
- LIEDTKE, H. & MARCINEK, J. 2002. *Physische Geographie Deutschlands*, Klett-Perthes.
- LOEW, A., LUDWIG, R. & MAUSER, W. 2006. Derivation of surface soil moisture from ENVISAT ASAR wide swath and image mode data in agricultural areas. *IEEE Transactions on Geoscience and Remote Sensing*, 44, 889-899.
- MAITRE, H. 2008. *Processing of Synthetic Aperture Radar (SAR) Images*, Wiley.
- MARINELLO, F., PEZZUOLO, A., GASPARINI, F., ARVIDSSON, J. & SARTORI, L. 2015. Application of the Kinect sensor for dynamic soil surface characterization. *Precision Agriculture*, 16, 601-612.
- MARSHALL, T. J. & HOLMES, J. W. 1979. *Soil Physics*, Cambridge, Cambridge University Press.
- MARTIN, R. D., ASRAR, G. & KANEMASU, E. T. 1989. C-band scatterometer measurements of a tallgrass prairie. *Remote Sensing of Environment*, 29, 281-292.
- MARZAHN, P. & LUDWIG, R. 2009. On the derivation of soil surface roughness from multi parametric PolSAR data and its potential for hydrological modeling. *Hydrol. Earth Syst. Sci.*, 13, 381-394.
- MASSONNET, D. & SOUYRIS, J. C. 2008. *Imaging with Synthetic Aperture Radar*, EFPL Press.
- MATTIA, F., SATALINO, G., BALENZANO, A., RINALDI, M., STEDUTO, P. & MORENO, J. Sentinel-1 for wheat mapping and soil moisture retrieval. Geoscience and Remote Sensing Symposium (IGARSS), 2015 Milan, Italy.
- MATTIA, F., SATALINO, G., PAUWELS, V. R. N. & LOEW, A. 2009. Soil moisture retrieval through a merging of multi-temporal L-band SAR data and hydrologic modelling. *Hydrology and Earth System Sciences*, 13, 343-356.
- MATTIA, F., TOAN, T. L., PICARD, G., POSA, F. I., ALESSIO, A. D., NOTARNICOLA, C., GATTI, A. M., RINALDI, M., SATALINO, G. & PASQUARIELLO, G. 2003. Multitemporal C-band radar measurements on wheat fields. *IEEE Transactions on Geoscience and Remote Sensing*, 41, 1551-1560.
- MESCHDE, M. 2015. *Geologie Deutschlands: Ein prozessorientierter Ansatz*, Springer Berlin Heidelberg.
- MOHANTY, B. P., COSH, M. H., LAKSHMI, V. & MONTZKA, C. 2017. Soil Moisture Remote Sensing: State-of-the-Science. *Vadose Zone Journal*, 16.
- MOHANTY, B. P., SKAGGS, T. H. & FAMILIETTI, J. S. 2000. Analysis and mapping of field-scale soil moisture variability using high-resolution, ground-based data during the Southern Great Plains 1997 (SGP97) Hydrology Experiment. *Water Resources Research*, 36, 1023-1031.
- MONTZKA, C., BOGENA, H., WEIHERMÜLLER, L., JONARD, F., BOUZINAC, C., KAINULAINEN, J., BALLING, J. E., LOEW, A., DALL'AMICO, J. T., ROUHE, E., VANDERBORGHT, J. & VEREECKEN, H. 2013. Brightness Temperature and Soil Moisture Validation at Different Scales During the SMOS Validation Campaign in the Rur and Erft Cathcments, Germany. *IEEE Transactions Geosc. Remote Sens.*, 51.
- MOREIRA, A., PRATS-IRAOLA, P., YOUNIS, M., KRIEGER, G., HAJNSEK, I. & PAPATHANASSIOU, K. P. 2013. A tutorial on synthetic aperture radar. *IEEE Geoscience and Remote Sensing Magazine*, 1, 6-43.
- MOTT, H. 2007. *Remote Sensing with Polarimetric Radar*, Hoboken, New Jersey, John Wiley & Sons, Inc. .
- OGILVY, J. A. 1992. *Theory of wave scattering from random rough surfaces.*, Bristol, Inst. of Physics Publ.
- OH, Y. 2004. Quantitative retrieval of soil moisture content and surface roughness from multipolarized radar observations of bare soil surfaces. *IEEE Transactions on Geoscience and Remote Sensing*, 42, 596-601.
- OH, Y., SARABANDI, K. & ULABY, F. T. 1992. An Empirical-Model and An Inversion Technique for Radar Scattering from Bare Soil Surfaces. *IEEE Transactions on Geoscience and Remote Sensing*, 30, 370-381.
- OLIVER, C. & QUEGAN, S. 2004. *Understanding Synthetic Aperture Radar Images*, SciTech Publ.

- PALOSCIA, S., MACELLONI, G., PAMPALONI, P. & SIGISMONDI, S. 1999. The potential of C- and L-band SAR in estimating vegetation biomass: the ERS-1 and JERS-1 experiments. *IEEE Transactions on Geoscience and Remote Sensing*, 37, 2107-2110.
- PALOSCIA, S., PAMPALONI, P., PETTINATO, S. & SANTI, E. 2010. Generation of soil moisture maps from ENVISAT/ASAR images in mountainous areas: a case study. *International Journal of Remote Sensing*, 31, 2265-2276.
- PALOSCIA, S., PETTINATO, S., SANTI, E., NOTARNICOLA, C., PASOLLI, L. & REPPUCCI, A. 2013. Soil moisture mapping using Sentinel-1 images: Algorithm and preliminary validation. *Remote Sensing of Environment*, 134, 234-248.
- PAN, F., PETERS-LIDARD, C. D. & SALE, M. J. 2003. An analytical method for predicting surface soil moisture from rainfall observations. *Water Resources Research*, 39, n/a-n/a.
- PASOLLI, L., NOTARNICOLA, C., BRUZZONE, L., BERTOLDI, G., DELLA CHIESA, S., HELL, V., NIEDRIST, G., TAPPEINER, U., ZEBISCH, M., DEL FRATE, F. & VAGLIO LAURIN, G. 2011. Estimation of Soil Moisture in an Alpine Catchment with RADARSAT2 Images. *Applied and Environmental Soil Science*, 2011.
- PATHE, C., WAGNER, W., SABEL, D., DOUBKOVA, M. & BASARA, J. B. 2009. Using ENVISAT ASAR Global Mode Data for Surface Soil Moisture Retrieval Over Oklahoma. *IEEE Transactions on Geoscience and Remote Sensing*, 47.
- PEBESMA, E. J. 2004. Multivariable geostatistics in S: the gstat package. *Computers & Geosciences*, 30, 683-691.
- PRÉVOT, L., CHAMPION, I. & GUYOT, G. 1993. Estimating surface soil moisture and leaf area index of a wheat canopy using a dual-frequency (C and X bands) scatterometer. *Remote Sensing of Environment*, 46, 331-339.
- QUESNEY, A., LE HEGARAT-MASCLE, S., TACONET, O., VIDAL-MADJAR, D., WIGNERON, J. P., LOUMAGNE, C. & NORMAND, M. 2000. Estimation of watershed soil moisture index from ERS/SAR data. *Remote Sensing of Environment*, 72, 290-303.
- RAHMAN, M. M., MORAN, M. S., THOMA, D. P., BRYANT, R., SANO, E. E., HOLIFIELD COLLINS, C. D., SKIRVIN, S., KERSHNER, C. & ORR, B. J. 2007. A derivation of roughness correlation length for parameterizing radar backscatter models. *International Journal of Remote Sensing*, 28, 3995-4012.
- RANEY, R. K., FREEMAN, T., HAWKINS, R. W. & BAMLER, R. A plea for radar brightness. *Geoscience and Remote Sensing Symposium*, 1994. IGARSS '94. Surface and Atmospheric Remote Sensing: Technologies, Data Analysis and Interpretation., International, 8-12 Aug. 1994 1994. 1090-1092 vol.2.
- REICHENAU, T. G., KORRES, W., MONTZKA, C., FIENER, P., WILKEN, F., STADLER, A., WALDHOFF, G. & SCHNEIDER, K. 2016. Spatial Heterogeneity of Leaf Area Index (LAI) and Its Temporal Course on Arable Land: Combining Field Measurements, Remote Sensing and Simulation in a Comprehensive Data Analysis Approach (CDAA). *PLOS ONE*, 11, e0158451.
- REYNOLDS, S. G. 1970. The gravimetric method of soil moisture determination Part III An examination of factors influencing soil moisture variability. *Journal of Hydrology*, 11, 288-300.
- RICHARDS, J. A. 2009. *Remote Sensing with Imaging Radar*, Springer Berlin Heidelberg.
- RIGNOT, E., WAY, J. B., MCDONALD, K., VIREECK, L., WILLIAMS, C., ADAMS, P., PAYNE, C., WOOD, W. & SHI, J. 1994. Monitoring of environmental conditions in Taiga forests using ERS-1 SAR. *Remote Sensing of Environment*, 49, 145-154.
- ROBOCK, A. 2003. Hydrology - Soil Moisture. In: HOLTON, J., PYLE, J., CURRY, J. (ed.) *Encyclopedia of Atmospheric Sciences*. Elsevier.
- ROMBACH, M. & MAUSER, W. 1997. Multi-Annual Analysis of ERS Surface Soil Moisture Measurements of Different Land Uses. 3rd ERS SYMPOSIUM Florence 97, 1997.
- ROTH, C. H., MALICKI, M. A. & PLAGGE, R. 1992. Empirical-Evaluation of the Relationship Between Soil Dielectric-Constant and Volumetric Water-Content As the Basis for Calibrating Soil-Moisture Measurements by Tdr. *Journal of Soil Science*, 43, 1-13.
- SAATCHI, S. S., VINE, D. M. L. & LANG, R. H. 1994. Microwave backscattering and emission model for grass canopies. *IEEE Transactions on Geoscience and Remote Sensing*, 32, 177-186.

- SABINS, F. F. 2007. *Remote Sensing: Principles and Interpretation*, Waveland Press.
- SANO, E. E., HUETE, A. R., TROUFLEAU, D., MORAN, M. S. & VIDAL, A. 1998. Relation between ERS-1 synthetic aperture radar data and measurements of surface roughness and moisture content of rocky soils in a semiarid rangeland. *Water Resources Research*, 34, 1491-1498.
- SATALINO, G., MATTIA, F., DAVIDSON, M. W. J., THUY LE, T., PASQUARIELLO, G. & BORGEAUD, M. 2002. On current limits of soil moisture retrieval from ERS-SAR data. *IEEE Transactions on Geoscience and Remote Sensing*, 40, 2438-2447.
- SCHMUGGE, T. J. & JACKSON, T. J. 1996. Soil moisture variability. In: STEWART, J. B., ENGMAN, E. T., FEDDES, R. A. & KERR, Y. (eds.) *Scaling up in hydrology using remote sensing*. Chichester: John Wiley & Sons.
- SCHMUGGE, T. J., JACKSON, T. J. & MCKIM, H. L. 1980. Survey of Methods for Soil-Moisture Determination. *Water Resources Research*, 16, 961-979.
- SCILANDS GMBH 2010. Digital Elevation Model 10 without anthropogenic landforms. Göttingen, Germany.
- SENTINEL-1 TEAM 2013. Sentinel-1 User Handbook. European Space Agency.
- SHIKLOMANOV, I. A. 1993. World fresh water resources. In: GLEICK, P. H. (ed.) *Water in crisis: A guide to the world's fresh water resources*. New York: Oxford University Press.
- SIMMER, C., THIELE-EICH, I., MASBOU, M., AMELUNG, W., BOGENA, H., CREWELL, S., DIEKKRÜGER, B., EWERT, F., FRANSEN, H.-J. H., HUISMAN, J. A., KEMNA, A., KLITZSCH, N., KOLLET, S., LANGENSIEPEN, M., LÖHNERT, U., RAHMAN, A. S. M. M., RASCHER, U., SCHNEIDER, K., SCHWEEN, J., SHAO, Y., SHRESTHA, P., STIEBLER, M., SULIS, M., VANDERBORGHT, J., VERECKEN, H., KRUK, J. V. D., WALDHOFF, G. & ZERENNER, T. 2015. Monitoring and Modeling the Terrestrial System from Pores to Catchments: The Transregional Collaborative Research Center on Patterns in the Soil–Vegetation–Atmosphere System. *Bulletin of the American Meteorological Society*, 96, 1765-1787.
- SMALL, D., MIRANDA, N. & MEIER, E. A revised radiometric normalisation standard for SAR. 2009 IEEE International Geoscience and Remote Sensing Symposium, 12-17 July 2009 2009. IV-566-IV-569.
- SMITH, N. V., SAATCHI, S. S. & RANDERSON, J. T. 2004. Trends in high northern latitude soil freeze and thaw cycles from 1988 to 2002. *Journal of Geophysical Research: Atmospheres*, 109, n/a-n/a.
- TENG, W. L., WANG, J. R. & DORAISWAMY, P. C. 1993. Relationship between satellite microwave radiometric data, antecedent precipitation index, and regional soil moisture. *International Journal of Remote Sensing*, 14, 2483-2500.
- THOMA, D. P., MORAN, M. S., BRYANT, R., RAHMAN, M., HOLIFIELD-COLLINS, C. D., SKIRVIN, S., SANO, E. E. & SLOCUM, K. 2006a. Comparison of four models to determine surface soil moisture from C-band radar imagery in a sparsely vegetated semiarid landscape. *Water Resources Research*, 42, n/a-n/a.
- THOMA, D. P., MORAN, M. S., BRYANT, R., RAHMAN, M., HOLIFIELD-COLLINS, C. D., SKIRVIN, S., SANO, E. E. & SLOCUM, K. 2006b. Comparison of four models to determine surface soil moisture from C-band radar imagery in a sparsely vegetated semiarid landscape. *Water Resources Research*, 42.
- THOMSEN, L. M., BAARTMAN, J. E. M., BARNEVELD, R. J., STARKLOFF, T. & STOLTE, J. 2015. Soil surface roughness: comparing old and new measuring methods and application in a soil erosion model. *SOIL*, 1, 399-410.
- TODD, D. K. & MAYS, L. W. 2004. *Groundwater Hydrology*, Wiley.
- TOMER, S. K., AL BITAR, A., SEKHAR, M., ZRIBI, M., BANDYOPADHYAY, S., SREELASH, K., SHARMA, A. K., CORGNE, S. & KERR, Y. 2015. Retrieval and Multi-scale Validation of Soil Moisture from Multi-temporal SAR Data in a Semi-Arid Tropical Region. *Remote Sensing*, 7, 8128-8153.
- TOPP, G. C., DAVIS, J. L. & ANNAN, A. P. 1980. Electromagnetic Determination of Soil-Water Content - Measurements in Coaxial Transmission-Lines. *Water Resources Research*, 16, 574-582.
- ULABY, F. T. & BATLIVALA, P. P. 1976. Optimum Radar Parameters for Mapping Soil Moisture. *IEEE Transactions on Geoscience Electronics*, 14, 81-93.

- ULABY, F. T., DUBOIS, P. C. & VANZYL, J. 1996. Radar mapping of surface soil moisture. *Journal of Hydrology*, 184, 57-84.
- ULABY, F. T., MOORE, R. K. & FUNG, A. K. 1982. *Microwave Remote Sensing. Active and Passive. Volume II. Radar Remote Sensing and Surface Scattering and Emission Theory*, Reading, Artech House Publishers.
- ULABY, F. T., MOORE, R. K. & FUNG, A. K. 1986. *Microwave Remote Sensing, Active and Passive, Vol.III: From Theory to Applications*, Boston, Artech House.
- ULABY, F. T., MOORE, R.K., FUNG, A.K. 1981. *Microwave remote sensing: active and passive. Volume I: microwave remote sensing fundamentals and radiometry*, Addison-Wesley.
- VAN EMMERIK, T., STEELE-DUNNE, S. C., JUDGE, J. & VAN DE GIESEN, N. 2015. Impact of Diurnal Variation in Vegetation Water Content on Radar Backscatter From Maize During Water Stress. *IEEE Transactions on Geoscience and Remote Sensing*, 53, 3855-3869.
- VECCHIA, A. D., FERRAZZOLI, P., GUERRIERO, L., NINIVAGGI, L., STROZZI, T. & WEGMULLER, U. 2008. Observing and Modeling Multifrequency Scattering of Maize During the Whole Growth Cycle. *IEEE Transactions on Geoscience and Remote Sensing*, 46, 3709-3718.
- VELOSO, A., MERMOZ, S., BOUVET, A., LE TOAN, T., PLANELLS, M., DEJOUX, J.-F. & CESCHIA, E. 2017. Understanding the temporal behavior of crops using Sentinel-1 and Sentinel-2-like data for agricultural applications. *Remote Sensing of Environment*, 199, 415-426.
- VERECKEN, H., KAMAI, T., HARTE, T., KASTEEL, R., HOPMANS, J. & VANDERBORGHT, J. 2007. Explaining soil moisture variability as a function of mean soil moisture: A stochastic unsaturated flow perspective. *Geophysical Research Letters*, 34.
- VERHOEST, N. E. C., LIEVENS, H., WAGNER, W., ALVAREZ-MOZOS, J., MORAN, M. S. & MATTIA, F. 2008. On the soil roughness parameterization problem in soil moisture retrieval of bare surfaces from synthetic aperture radar. *Sensors*, 8, 4213-4248.
- VISSMAN, W. & LEWIS, G. L. 2003. *Introduction to Hydrology*, Prentice Hall.
- VILLANO, M. 2014. SNR and Noise Variance Estimation in Polarimetric SAR Data. *IEEE Geoscience and Remote Sensing Letters*, 11, 278-282.
- WAGNER, W., LEMOINE, G., BORGEAUD, M. & ROTT, H. 1999a. A study of vegetation cover effects on ERS scatterometer data. *IEEE Transactions on Geoscience and Remote Sensing*, 37, 938-948.
- WAGNER, W., LEMOINE, G. & ROTT, H. 1999b. A method for estimating soil moisture from ERS scatterometer and soil data. *Remote Sensing of Environment*, 70, 191-207.
- WARRICK, A. W. 2003. *Soil Water Dynamics*, Oxford University Press.
- WEGMÜLLER, U. 1990. The effect of freezing and thawing on the microwave signatures of bare soil. *Remote Sensing of Environment*, 33, 123-135.
- WEI, M. Y. 1995. *Soil Moisture: Report of a Workshop Held in Tiburon, California, 25-27 January 1994*, NASA Headquarters.
- WESTERN, A. W., BLÖSCHL, G. & GRAYSON, R. B. 1998. Geostatistical characterisation of soil moisture patterns in the Tarrawarra catchment. *Journal of Hydrology*, 205, 20-37.
- WISEMAN, G., MCNAIRN, H., HOMAYOUNI, S. & SHANG, J. 2014. RADARSAT-2 Polarimetric SAR Response to Crop Biomass for Agricultural Production Monitoring. *IEEE Journal of Selected Topics in Applied Earth Observations and Remote Sensing*, 7, 4461-4471.
- WMO, W. M. O. 2014. *Guide to Meteorological Instruments and Methods of Observation. CIMO Guide*. [Online]. WMO. Available: URL: https://library.wmo.int/opac/doc_num.php?explnum_id=3121 [Accessed 04.10.2017 2017].
- YAMAGUCHI, Y., MORIYAMA, T., ISHIDO, M. & YAMADA, H. 2005. Four-component scattering model for polarimetric SAR image decomposition. *IEEE Transactions on Geoscience and Remote Sensing*, 43, 1699-1706.
- ZRIBI, M., BAGHDADI, N., HOLAH, N. & FAFIN, O. 2005. New methodology for soil surface moisture estimation and its application to ENVISAT-ASAR multi-incidence data inversion. *Remote Sensing of Environment*, 96, 485-496.
- ZRIBI, M., CIARLETTI, V., TACONET, O., BOISSARD, P., CHAPRON, M. & RABIN, B. 2000. Backscattering on soil structure described by plane facets. *International Journal of Remote Sensing*, 21, 137-153.

Appendix

Land Use Classification method for the ERS Soil Moisture Index

The land use classifications for 1995-1997 and 1999-2003 are based on the following LANDSAT acquisitions:

- LANDSAT 5 TM: 1995-08-05, 1995-10-24, 1996-07-22, 1997-08-10, 2003-07-10, and 2003-08-11.
- LANDSAT 7 ETM+: 1999-09-09, 2000-05-06, 2000-08-26, 2001-03-06, 2001-05-25, 2001-06-26, 2001-08-29, 2002-08-16, 2003-02-24 and 2003-03-28.

All LANDSAT acquisitions have been atmospherically corrected using the software FLAASH (Spectral Sciences Inc., Burlington) in ENVI. Clouds and cloud shadows have been masked out by using a ratio of LANDSAT bands 6 and 1 and bands 2 and 5, respectively. Based on the ATKIS (Amtlich Topographisch-Kartographisches Informationssystem) digital land cover model, masks for grassland and arable land were produced. Within these masks a maximum-likelihood classification for each year has been performed (based on all available LANDSAT acquisitions per year). The classification results are then summarized in a land use base map based on the following decision tree:

1. If a pixel is classified at least in two years as grassland (or arable land) and the ATKIS digital land cover model classified the pixel as grassland (or arable land), the pixel will be classified as grassland (or arable land).
2. If a pixel is classified each year as grassland (or arable land) and the ATKIS digital land cover model has classified the pixel as arable land (or grassland), the pixel will be classified as grassland (or arable land).
3. In all other cases the pixel will be masked out.

The resulting product is a land use base map that differentiates grassland and arable land. All other land use classes like forest, built-up area, water bodies etc. were masked out.

In the final land cover maps per year, all pixels that are classified as grassland in the land use base map are classified as grassland as well. The pixels that are classified as arable land in the land use base map are classified into finer crop types in the yearly land cover maps by using a maximum-likelihood classifier that was trained on ground truth data. This ground truth dataset was supplied by cooperating farmers that gave us their management records and consist of 125 agricultural fields in total and encompasses different crop types (see Table A.1.). The test area is situated outside of the Rur catchment but directly at its eastern border. Tables A.1, A.2 and

A.3 show different error indices to assess the classification performance of the maximum-likelihood classification in comparison to the ground-truth information.

Since in some year (1995, 1999 and 2002), no LANDSAT acquisition from within the vegetation period of cereals was available, cereals could not be classified by the maximum-likelihood classifier. Therefore, in these years, the NDVI was calculated for the pixels that were classified as arable land in the land use base map, to identify pixels with an NDVI < 0.2. These pixels are assumed to be bare soil. Since hardly any arable land will be left fallow for a whole vegetation period, we assume that these fields are recently harvested cereal fields. Consequently, the respective pixels were classified as cereal pixels.

Table A.1. User's Accuracy of the yearly land use maps.

| Crop Type | 1995 | 1996 | 1997 | 1999 | 2000 | 2001 | 2002 | 2003 |
|------------------|-------------|-------------|-------------|-------------|-------------|-------------|-------------|-------------|
| Bare Soil | 100 | | | 98.5 | | | 99.8 | |
| Spelt | | | | | 92.7 | 97.9 | | 86.0 |
| Strawberries | | | | | 95.3 | 100 | | |
| Oat | | | | | | 100 | | 94.5 |
| Potatoes | | | | | | | | 93.5 |
| Rapeseed | | | | 49.5 | 94.4 | 91.5 | 88.1 | 93.2 |
| Rye | | | | | 44.2 | 100 | | |
| Mustard | | | | | | | | 100 |
| Summer Barley | | 100 | | | | 94.1 | | |
| Winter Barley | | | | | 92.0 | 97.9 | | 96.3 |
| Winter Wheat | | 92.6 | 95.9 | | 97.2 | 98.1 | | 94.2 |
| Sugar Beet | 100 | 90.6 | 87.0 | 100 | 92.4 | 90.4 | 97.6 | 94.9 |

Table A.2. Overall Accuracy of the yearly land use maps.

| Year | Overall Accuracy [%] |
|-------------|-----------------------------|
| 1995 | 99.1 |
| 1996 | 86.8 |
| 1997 | 85.6 |
| 1999 | 82.4 |
| 2000 | 90.2 |
| 2001 | 96.1 |
| 2002 | 86.4 |
| 2003 | 93.2 |

Table A.3. Kappa-Values of the yearly land use maps.

| Year | Kappa |
|-------------|--------------|
| 1995 | 0.98 |
| 1996 | 0.79 |
| 1997 | 0.72 |
| 1999 | 0.59 |
| 2000 | 0.86 |
| 2001 | 0.95 |
| 2002 | 0.76 |
| 2003 | 0.91 |

Erklärung

Ich versichere, dass ich die von mir vorgelegte Dissertation selbständig angefertigt, die benutzten Quellen und Hilfsmittel vollständig angegeben und die Stellen der Arbeit – einschließlich Tabellen, Karten und Abbildungen –, die anderen Werken im Wortlaut oder dem Sinn nach entnommen sind, in jedem Einzelfall als Entlehnung kenntlich gemacht habe; dass diese Dissertation noch keiner anderen Fakultät oder Universität zur Prüfung vorgelegen hat; dass sie – abgesehen von unten angegebenen Teilpublikationen – noch nicht veröffentlicht worden ist, sowie, dass ich eine solche Veröffentlichung vor Abschluss des Promotionsverfahrens nicht vornehmen werde. Die Bestimmungen der Promotionsordnung sind mir bekannt. Die von mir vorgelegte Dissertation ist von Prof. Dr. Karl Schneider betreut worden.

Nachfolgend genannte Teilpublikationen liegen vor:

Esch, S., Korres, W., Reichenau, T.G., Schneider, K. (2016): Observing Soil Moisture Patterns on Agricultural Fields in the Rur Catchment using ERS SAR Datasets. *Proceedings of the ESA Living Planet Symposium*, Prague, Czech Republic, 09-13 May, 2016.

Esch, S., Korres, W., Reichenau, T.G., Schneider, K. (2017): Soil moisture index from ERS-SAR and its application to the analysis of spatial patterns in agricultural areas. *Journal of Applied Remote Sensing (JARS)*. [in review]

Köln, den 31.01.2018

(Sabrina Esch)